CRANFIELD UNIVERSITY

DEVINDER PAL SINGH BHAMBRA

COMPUTATIONAL ANALYSIS OF A-PILLAR VORTEX FORMATION IN AUTOMOTIVE APPLICATIONS

SCHOOL OF ENGINEERING
COMPUTATIONAL FLUID DYNAMICS

MASTERS BY RESEARCH
Academic Year: 2011 - 2013

Supervisor: DR. BEN THORNBER
JANUARY 2013

CRANFIELD UNIVERSITY

SCHOOL OF ENGINEERING
COMPUTATIONAL FLUID DYNAMIC

MASTERS BY RESEARCH

Academic Year 2011 - 2013

DEVINDER PAL SINGH BHAMBRA

COMPUTATIONAL ANALYSIS OF A-PILLAR VORTEX FORMATION IN AUTOMOTIVE APPLICATIONS

Supervisor: DR. BEN THORNBER
JANUARY 2013

This thesis is submitted in partial fulfilment of the requirements for the degree of Masters by Research

ABSTRACT

The research focusses on computational analysis of vortex generation behind A-Pillar of simplified model derived from Jaguar XF that excludes air from the underside of vehicle. This vortex formation contributes in generating wall pressure fluctuations especially at speeds higher than 100km/hr. It is a collaborative work between Cranfield University and Jaguar Land Rover. Three dimensional pressure based incompressible flow using Large Eddy Simulation turbulence model is selected for computational analysis in FLUENT v14. This used high parallel computing systems available in Cranfield University. In the initial phase, three grid resolutions (coarse, medium and fine) were prepared in ICEM CFD with fine case consisting of 10 million cells.

Qualitative analysis includes extraction of slices, 3-D and surface streamlines and pressure and velocity contours for capturing the unsteadiness due to the vortex formation over the front side glass surface. The iso-surface of Q captures the unsteadiness at the A-Pillar wake and side mirror wake over front side glass surface. It also reveals that the range of length scales captured were limited even at the finest grid resolution. Quantitative analysis compares the mean pressure (C_p) data with JLR results. Probes were located at 51 locations over the front side glass window that showed a good comparison; specifically for the fine grid; with maximum variation incurred at probes located in separation areas. For predicting the wall pressure fluctuations, a total of ten probes were located over the front side glass window surface. The surface pressure (static) data was recorded for 1 sec of flow-time and later imported in MATLAB for post-processing. The results obtained in 1/3rd octave band showed that the large scales were too energetic and small scales are not captured. However, comparing sound pressure levels with the **A**ero-acoustic **W**ind **T**unnel (AWT); provided by JLR; it is concluded that either the grid is too coarse to resolve higher frequencies or the numerical modelling used is too dissipative to benefits the use of LES.

Keywords: Large Eddy Simulations, Sound Pressure Levels, iso-surface of Q, wall pressure fluctuations

ACKNOWLEDGEMENT

I would like to thank Dr. Ben Thornber, Dr. Evgeniy Shapiro for supervising and their valuable help and support throughout this research. In addition to this I would like to thank Adrian Gaylard at Jaguar Land Rover for their feedback and valuable suggestions.

A considerable thanks to the people with whom I shared my time in Cranfield University with; Atma Prakash, Nabil Haneef, Karthik Yadiyal, Ashish Kamthe, Mike Probyn and Charles for their valuable moral support throughout this research.

I would like to thank Andy Gittings at High Performance Computing centre at Cranfield University for their continuous support whenever required.

On personal grounds, I would like to thank my sister and parent who have always encouraged me and provided moral support throughout my work and life.

TABLE OF CONTENT

LIST OF FIGURES

LIST OF TABLES

LIST OF ABBREVIATIONS

JLR	Jaguar Land Rover
AWT	Aero-Acoustic Wind Tunnel
SPL	Sound Pressure Level
LDV	Laser Doppler Velocimeter
URANS	Unsteady Reynolds Navier-Stokes Equation
RANS	Reynolds Navier-Stokes Equation
LES	Large Eddy Simulation
DES	Detached Eddy Simulation
CFL	Courant-Friedrichs-Levy
TFLOPS	Tera Floating point Operations Per Second
dB	Decibel
Hz	Hertz

1. INTRODUCTION

This chapter outlines the motivation of this research followed by the objectives. The second section comprises of previous studies related to the flow characteristics and the aerodynamically induced noise generations experienced behind the A-Pillar region. Different studies based on empirical and numerical studies are presented including the effects of changing A-Pillar geometry with various windshield angles and at different yaw angles.

1.1 MOTIVATION AND OBJECTIVES

The concept of aerodynamics in road vehicles dates back to 1921 when one of the Australian aircraft engineer; Rumpler Tropfenwagen; developed a road vehicle (known as teardrop car) of aerofoil shape which was later launched in Berlin car show. Though the car claimed a drag of 0.28 which is still a challenge to achieve for road vehicles but it was a commercial failure. The majority of car manufacturers concentrate on designing an external body of their vehicles that can attract the consumers. However, a sudden and sharp increase in the oil prices in 1970s challenged all car manufacturers to design not only an attractive external structure but a fuel efficient vehicle. Ever since then, the concept of aerodynamics, which largely affects the fuel consumption of a vehicle, grounded the basic aspect of every vehicle design life cycle.

According to the survey in UK (Observatory, 2001 Census), there has been sudden increase in the car ownership during the past decade as shown in Figure 1.1. Moreover, there has been substantial difference in the percentage usage of car as the main mode of transport in comparison with other modes of transport such as public transport, and home working. These economic changes not only led to adverse environmental issues but caused health related issues to the driver and the passenger. The air and structure-borne noises typically affecting the human body can cause annoyance especially sleep disturbance, and less apparent effects such as cardiovascular and mental health problems reducing performance at work.

To an extent, the car manufacturers have been successful in reducing the noise levels typically affecting the driver and the passenger. However, according to Parliamentary Office of Science & Technology postnote [38] the noise levels for new road vehicles have been tightened to 11 dB since 1970s. It is anticipated that these noise levels will be further reduced in the future. So, researchers aim to achieve restricted noise levels originating from the vehicle such as tyre noise, engine noise, transmission noise or air and structure borne noises.

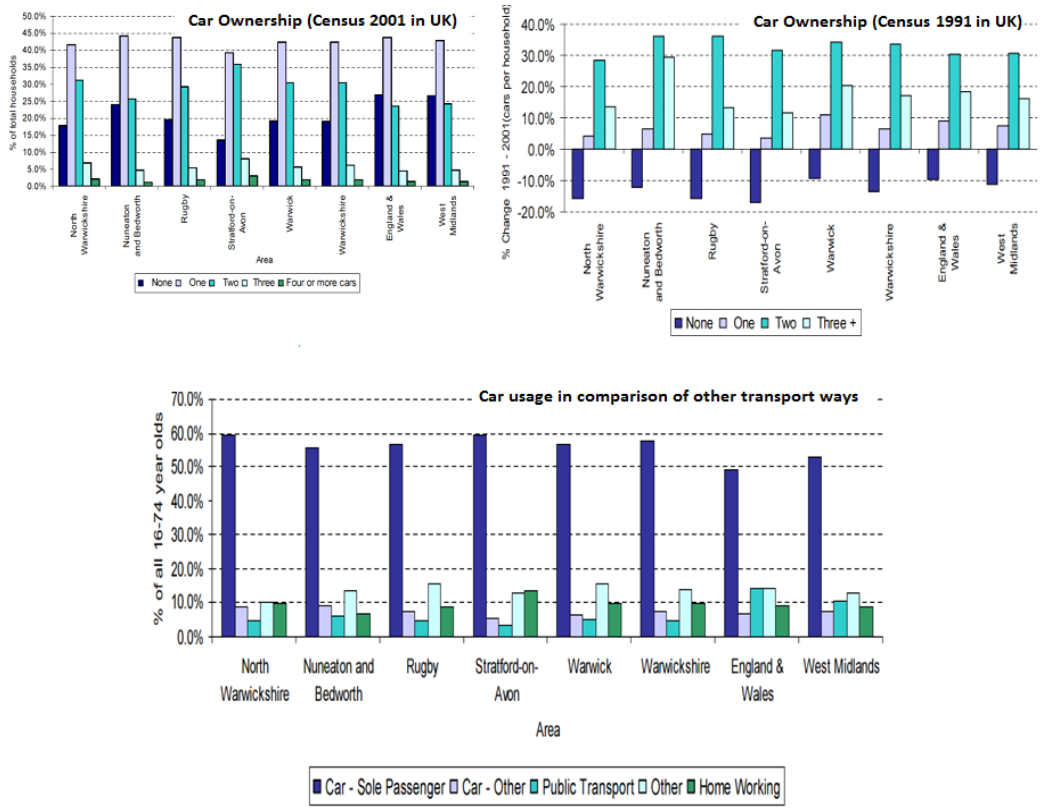

Figure 1.1 Car Ownership Statistics (Observatory, 2001 Census)

This research will focus on vortex generated behind the A-Pillar leading to external wall pressure fluctuations over the front side glass surface. The characteristic behaviour of the vortex leads to unsteady pressure fluctuations that significantly influence driver's concentration and health during long hour driving.

The objectives of this research are achieved by:

- Constructing three grid resolutions namely coarse, medium, and fine for understanding unsteady flow field
- Analysing vortex generation behind A-Pillar
- Quantitative analysis of surface pressure obtained from different probes located across the front side glass surface
- Comparison of above surface pressure results with data provided by JLR
- Statistical analysis of Sound Pressure Level (SPL) with preferred one-third octave frequency band
- Comparison of above obtained SPL results with data available from JLR.
- Assessment of highly under-resolved LES for practical applications

1.2 Literature Review

This section describes previous research on vortex generation and external wall pressure fluctuations generating behind the A-Pillar. This includes a thorough review of literature based on empirical and numerical studies of vortex generation published in relevant journal articles and conference papers. Experimental studies including modifications in the design of A-Pillar are discussed in Section 1.2.1 while the numerical studies in section 1.2.2.

1.2.1 Empirical studies

Stapleford [43] conducted first experimental work on three different objects (simple cuboid structure, cuboid with filleted front edges, and a passenger car) to aerodynamically analyse induced noise at different yaw angles. The authors found that vortex generated behind the A-Pillar manifested due to aerodynamic noises. SPL of 120 dB was generated from the vortex generation with 20 dB increase because of the background tunnel ambient noise. Moreover, high SPL in the low frequency region is predicted as a consequence of large scale turbulent structures in flow separation area.

Fricke [12] conducted preliminary experiments to analyse pressure fluctuations in region of flow separation. This study concluded that pressure fluctuations are significant near the shear layer above the recirculating flow to the reattachment point. . However, [32] described that average pressure fluctuations are significant near the reattachment flow region.

Watanabe et al. [46] examined conical vortex formation behind the A-Pillar. The author highlighted the wind noise generation in reference to rain gutter height and side window recess depth and the way of suppressing the wind noise by providing wind deflector around the A-Pillar

Buchheim et al. [46] verified results obtained by Stapleford, stating that the noise generated behind the A-Pillar was 20 dB greater than the background noise. However, Buchheim indicated that varying the geometry of A-Pillar region, noise generated can be made comparable to background noise. The

authors also investigated that the noise generation due to A-Pillar produced highest interior noise level at 60 dB within the frequency range of 250-500 Hz.

Sadakata et al. [42] proposed an impulsive change in the SPL when the slant angle of the A-Pillar is between 40 ^{o}-50 ^{o}. The authors depicted that noise level is reduced by coalescing appropriate slant angle of A-Pillar with the curled windshield

Haruna et al. [20] suggested that change in yaw angle shows corresponding change in the Sound Pressure Level. The authors proved above statement by conducting an experiment on a production vehicle in a wind tunnel. The free stream velocity was configured at 50 km/h with different yaw angles ranging between 0 ^{o} and 10 ^{o}. The experiment showed that the vortex is stronger when the vehicle is at 10 ^{o} yaw angle as compared to of 0 ^{o} yaw angle. However, this work did not provide information about the the size of vortices. Haruna et al. [19] further developed a numerical model and later on validated with an experimental study. The authors found varying sound pressure levels ranging between 110 dB to 130 dB are produced at different free stream velocities of 50, 100 and 140 km/h respectively.

Popat [40] performed an experimental work on A-Pillar vortex generation by varying the A-Pillar slant angle. His work concluded that windshield angle between 50 ^{o}-60 ^{o} produce a fully developed conical vortex generation.

Neinaltowska [35] conducted an experiment on the A-Pillar aimed at predicting the flow behind them by varying the velocity. Neinaltowska measured numerous pressure fluctuations with varying velocities at a point perpendicular to the side window. His work concluded that turbulence does not depend on the velocity, but depends on the wall distance (decreases with the wall distance) Moreover, highest region of turbulence is generated in the direction perpendicular to the flow.

Hamel [17] performed experiment work on aerodynamic noise generated behind A-Pillar by varying free stream velocities and the side mirror height. It was noticed that the sound pressure fluctuations increased by 20 dB at lower

frequency close to the location of side mirror. However, on increasing the height of side mirror relative to vertical axis, an increase in sound pressure level of the order of 4 dB at lower frequency is noticed beneath the side mirror and near to A-Pillar.

Alam et al. [4] conducted an experimental work on a Ford Felcon ER aimed at visualizing and studying the conical vortices behind the A-Pillar and various effects of Reynolds Number. Tufts were used on side mirrors to clearly visualize the flow around A-pillar as shown in Figure 1.2.

Figure 1.2 Full Scale Wind Tunnel predicting flow over A-Pillar Vortex using tufts

[4]

Different free stream velocities such as 40, 80, 120 and 140 km/h were used in this experiment. The authors predicted that change in free-stream velocity is noticeable with different yaw angles and at different locations on the side window. Moreover, Reynolds number shows considerable change below free stream velocities of 60 km/h as compared to velocities ranging between 60 - 120 km/h.

Alam [3] continued above experimental studies by varying the windshield radii and analysing the flow based on this modification. The result showed that there exists a relative impact of pressure fluctuations with change in windshield radii. He noticed that the maximum pressure fluctuations are measured between the separation and reattachment area of A-Pillar. Furthermore, the author amended the geometry of A-Pillar radius and examined RMS surface pressure C_p at different yaw angles. This depicted that with an increase in windshield radii there is decrease in the RMS C_p at different yaw angles.

Alam et al. [5] tested five 40% scale idealised model vehicle with varying velocities and yaw angles, windshield and A-Pillar radii (no edge, no A-Pillar edge and tightest A-Pillar edge) as shown in Figure 1.3. The authors concluded that for positive yaw angle does not shows no considerable change in mean and fluctuating pressures on Reynolds Number. However, slight dependency was noticed for zero and negative yaw angles. Moreover, positive yaw angle resulted in reduction of the area and magnitude of the flow separation and vice-versa.

Figure 1.3 Varying Radius of A-Pillar and Windshield Angle [5]

Alam et al. [6] developed full scale model of General Motors – Holden VT Calais with modified A-Pillar for predicting flow behaviour by varying the its local geometry and Reynolds Number. This work showed that change in A-Pillar geometry plays an important role in reducing the aerodynamic noise as shown in Figure 1.4 and Figure 1.5 Moreover, the study revealed that Reynolds Number does not show any significance on mean and fluctuating pressure coefficients.

Side View of Flow Visualisation with Standard A-pillar, Yaw = 0°, Speed = 100 km/h

Side View of Flow Visualisation with Modified A-pillar, Yaw = 0°, Speed = 100 km/h

Figure 1.4 Full Model vehicle with standard and Modified A-Pillar [6]

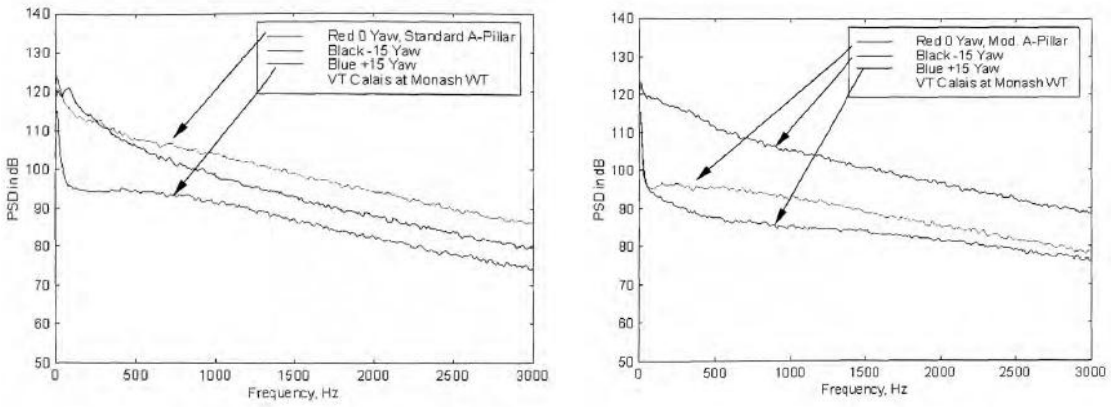

Figure 1.5 Comparison of Power Spectra on two models at various Yaw Angles with standard A-Pillar model (left) and modified A-Pillar right) [6]

Alam et al.[5] conducted an experiment on four models (three 40% scale models and one 30% scale model) to understand and visualize the surface mean and fluctuating pressures over the side mirror and A-Pillars, and further predict the change in pressure magnitude on varying A-Pillar radii. The models used for this work are shown in Figure 1.6. The results showed that for both models (Ford and 100R), the surface mean (Cp) and fluctuating (Cp_{rms}) pressure coefficients show autonomous behaviour with Reynolds Number. Moreover, the leeward side yaw angle obtained greater (Cp_{rms}) than windward.

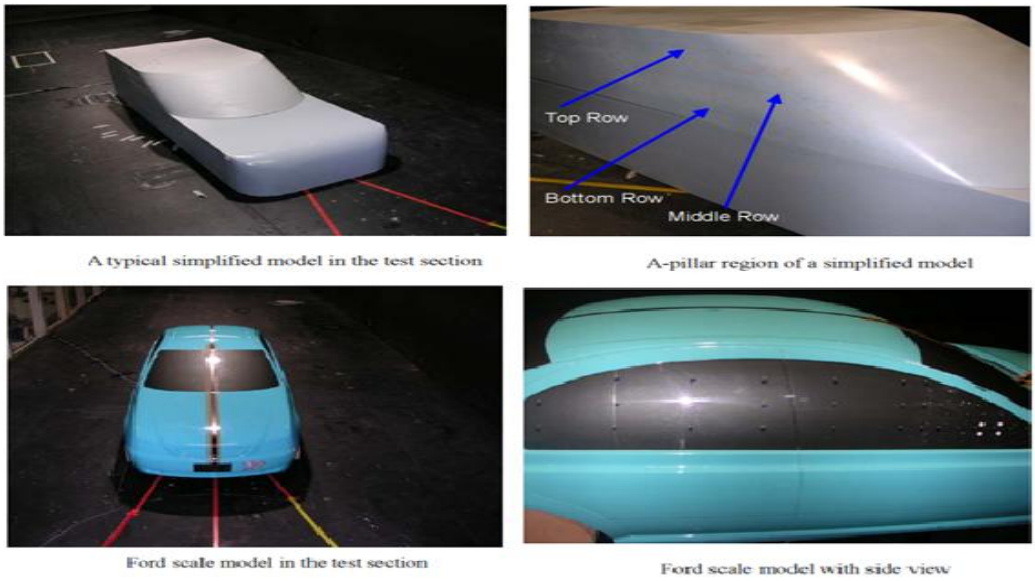

Figure 1.6: Different views of vehicle at different angles of A-Pillar (Alam, et al., 2005)

Hoarau [22] studied A-Pillar conical vortex generation resulting in unsteady wall pressure fields, through Laser Doppler Velocimeter (LDV) measurements and multi-point pressure measurements using off-set microphones. The free stream velocity (30 m/s) and Reynolds Number (1.8×10^5) were used based on the height of the model. Sixteen pressure sensors were used to analyse the air flow on the side mirror. The mean measurement of the mean and fluctuating velocity fields was measured from a distance of 100 mm from the nose of the body as shown in Figure 1.7. The results demonstrated the formation of conical vortices on the side walls of the car. Indeed, the flow separating sharp edges and the vortex core are the regions showing unsteady behaviour. Moreover, the vertical direction's fluctuating velocities are much larger than in the horizontal fluctuating velocities. A spectral analysis of the fluctuating pressure under the vortex core was accomplished to analyse the connection between the temporal and spatial scales of the unsteady aerodynamics and the wall pressure fields.

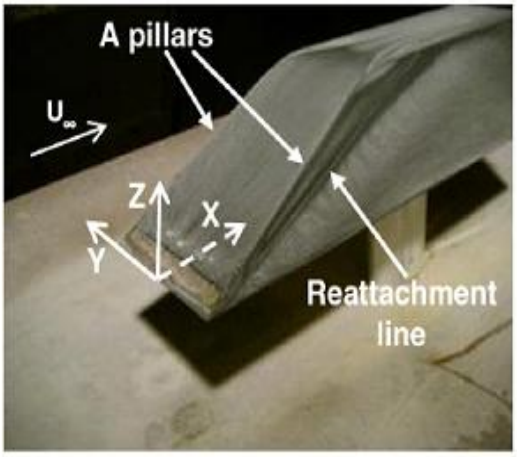

Body of a car

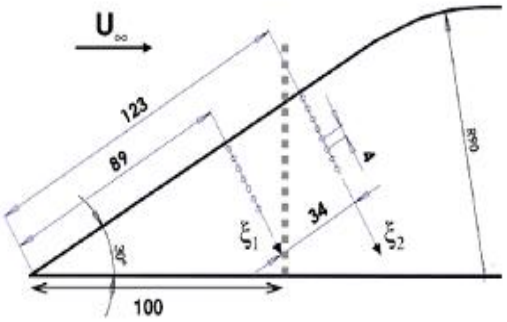

Pressure Holes in lateral Surface of the body (in mm). Vertical line shows the location of LDV.

Figure 1.7 Vehicle front body (left) and location of LDV points on front (right) [22]

1.2.2 Numerical Studies

Table 2.2 summarizes the numerical work published by authors on A-pillar along with their research area and comments on the outcomes.

In 1984, Onorato studied the effect of air drag performing numerical simulation and concluded that the vortex generation due to A-Pillar have significant effect on the external aerodynamic noise. Onorato defined total drag as

$$D_{Tot} = \int_A (P_{io} - P_i)d\sigma + \frac{\rho V_0^2}{2}\int_A \left(\frac{U_Y^2}{V_0^2} + \frac{U_Z^2}{V_0^2}\right)d\sigma - \frac{\rho V_0^2}{2}\int_A \left(1 - \frac{U_x}{V_0}\right)^2 d\sigma \quad \textbf{(1-1)}$$

The right hand side of this equation comprises of three parts. The first integral depicts the wake produced as a result of drag whereas second part represents the dissipation of energy because of A-Pillar vortex generation. The third part describes the longitudinal velocity deficit generated in the wake region. This work predicted that reducing the A-Pillar vortices will result in lowering the effect of drag and hence saving the fuel.

Hanaoka in 1993 [18] presented a numerical based simulation for predicting the aerodynamic noise at various slant angles of windshield (30°, 45°, 52.5°, 60° and 75° from horizontal axis) at the speed of 100 km/h. Quasi-DNS method and Lighthill-Curle's method for (noise prediction) was used. Their study showed that with an increase in the windshield slant angle there was a corresponding increase in wind noise, (critical at 50^o). Moreover, the aerodynamic was of dipole sound source instigated from the area where the separation of vortex and reattachment collectively occurred. Also, there was a turbulent shear interaction noticed due to the side window roof area. However, this work was unable to provide any data that could have shown the comparison with experimental data.

Zhu in 1993 [48] conducted CFD on different windshield slant angles but the distinguishing factor between the previous and this study was that latter conducted at different velocities (75, 100 and 150 km/h) whereas former used the same velocity of 100 km/h for all windshield slant angles. Zhu used CFD software called SCRYU and 150,000 grid points were generated for their car

model. The result obtained showed that the vortex generation and the breakdown process behind the A- Pillar is the region of aerodynamic noise generation. Furthermore, higher pressure variations were noticed at the junction of roof side and the front side window. The fluctuations in pressure obtained from the roof side were far greater than those generated behind the A-Pillar and increased with an increase in windshield slant angle.

A comparison of numerical and experimental simulation was conducted by Bergamini on A-Pillar of the bluff body moving with a velocity of 100 km/h [9]. The work focussed on analysing the liability of the numerical simulation for depicting the aerodynamic noise by resolving the Ffowks-Williams Hawkings equation. Unsteady RANS (Reynolds Averaged Navier-Stokes) simulation was used for numerical simulation. The results obtained showed peak sound pressure level was over predicted by 20 dB as compared to experimental results. These were not satisfactory specifically at points on the edge of the roof i.e. separation point.

In 2001, Andreas Kleber published a paper in a Journal article of FLUENT software users working towards simulation of air flow around an Opel-Astra. The computational analysis was conducted in ANSA and FLUENT v5. During the meshing, the author faced an obstacle in applying prism layers near areas such as front side window area and A-Pillar. In order to overcome this problem, these areas were meshed with tetrahedron or hexahedral blocks in Gambit. A 3D steady state incompressible Navier –Stokes equation was used in this work and the turbulence model used was k-ε Model. The result obtained on A-Pillar region is shown in Figure 1.8

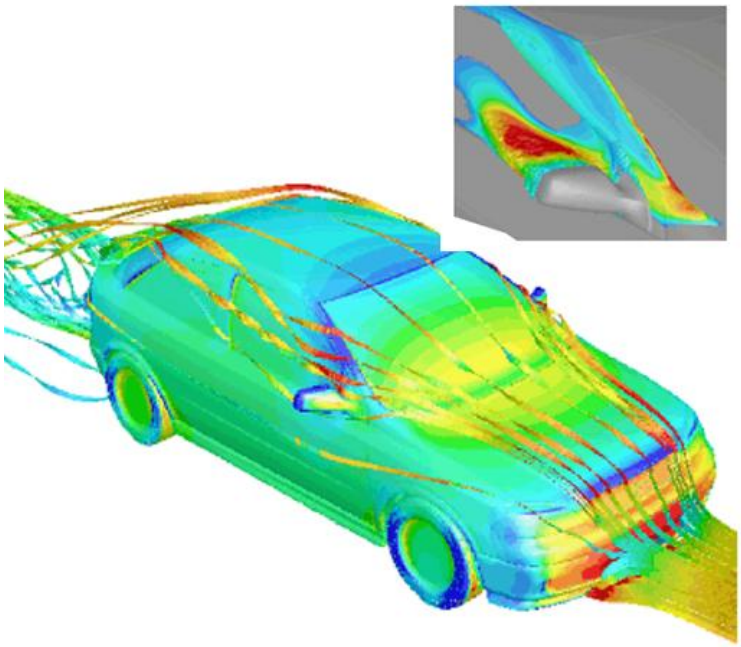

Figure 1.8: Flow Visualization using Pressure Distribution and iso-surface of Q at zero total pressure (Kleber, 2001)

Li in 2003 [29] performed computational analysis using CFD software named PAM-FLOW with the help of time dependant Navier-Stokes equation. Two modelling methods, finite difference (structured hexahedron mesh) and finite element (unstructured tetrahedral mesh) were used. But they did not provided any results for the finite difference and there was no comparison shown for both of these modelling methods. They concluded that for the experimental and finite element method, there was a progress in the aerodynamic noise generated in the A-Pillar region after modifying the rain gutter.

In 2004, Murad simulated two simple vehicles with different geometries of A-Pillar with different velocities and yaw angles. The results obtained were based on pressure coefficients and were compared with the experimental result [34][36]. The results obtained showed that the rectangular shaped model exhibited larger vortices than the slanted A-Pillar type of model. Moreover, the results obtained were greatly influenced by the change in yaw angles for both the models which show exactly opposite results i.e. rectangular shaped model predicted higher intensity of vortices on the windward side and lesser on leeward side where the converse is true for the slanted A-Pillar type model as shown in Figure 1.9.

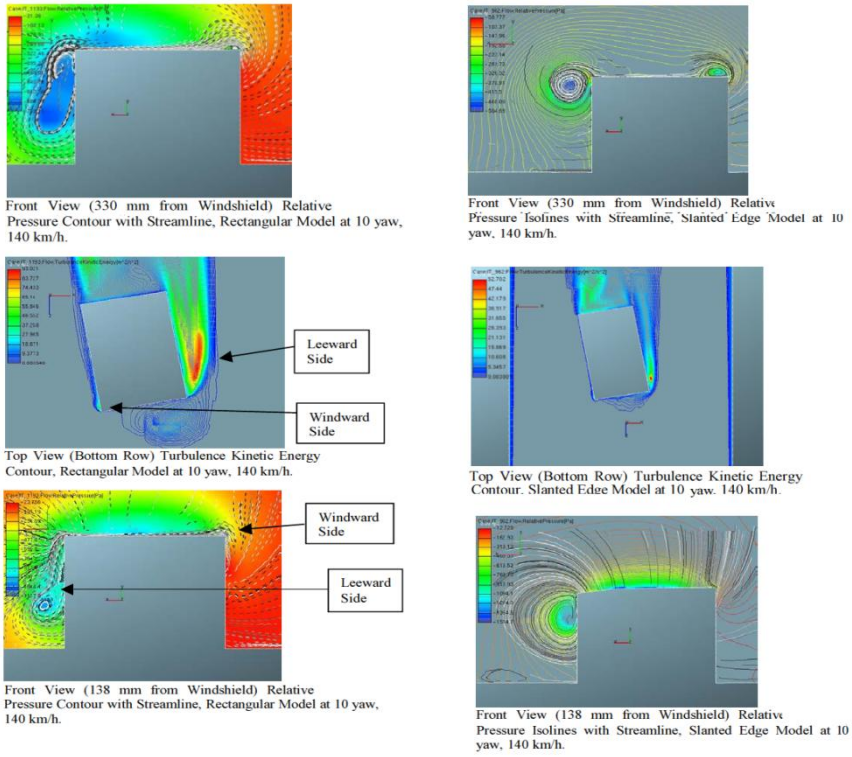

Figure 1.9: Pressure Contours with streamlines at various yaw angles [36]

In 2004, Gaylard worked on a CFD Simulation of A-Pillar/Side Glass Flows for Bluff SUV Geometries and conducted a comparison of analytical results; produced by ExaPowerFLOW; and experimental results; MIRA Full Scale Wind Tunnel (FSWT) [13][2][2][2]. The CFD software used for the flow analysis was ExaPowerFLOW (Lattice Boltzmann Solver). The results were based on pressure distribution and aero-acoustic simulation around the A-Pillar/Side Window area. The points were positioned on side mirror and the flow was

predicted on each point thereafter. Results on comparison showed good agreement with an over prediction of A-Pillar vortex strength and size whereas RANS method under-predicted the strength and size flow. Table 1.1 and Table 1.2 illustrate the analytical data used for capturing simulation results.

Table 1.1 Analytical Data

ID	Simulation type	Turbulence model	Boundary layer length scale	Inlet velocity m/s
A	Low Resolution	Dissipative	Standard	35
B	Aerodynamic	Dissipative	Standard	27.8
C	Aerodynamic	Unsteady	Standard	27.8
D	Aerodynamic	Unsteady	Standard	36.1
E	Aerodynamic	Unsteady	Local	27.8
F	Aerodynamic	Unsteady	Local	36.1

Table 1.2 Mesh Size and Resolution of Grids

Content	Mesh Size	Resolution
Low Resolution	10mm mesh(whole vehicle) 5mm mesh(A-pillar)	18 million – 27 million volume elements; 1.4 million to 1.8 million surface elements
Aerodynamics	11 mm (whole vehicle and stagnation Zone) 5.5 mm (whole vehicle including wheels) 2.75 mm (A-Pillar)	
Aero-Acoustic	12 mm (whole vehicle and stagnation Zone) .5 mm (A-Pillar)	

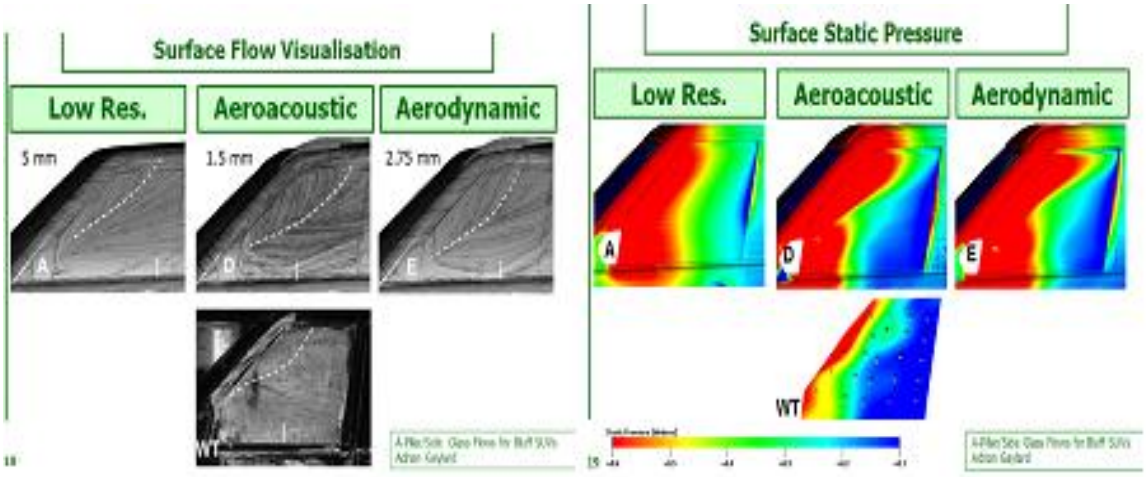

Figure 1.10: Experimental Results extracted on surface of front side glass window [1]

Gaylard [13] continued the work on Bluff SUV's but this time the chief aspect was detailed analysis of side glass surface noise spectra. As in earlier work they also used ExaPowerFLOW software for CFD simulations and computed the surface noise spectra. The strength and size of the vortex generated in the A-Pillar region were over-predicted. An estimate for frequency range was also given which showed that the simulation is constrained by the accuracy of different turbulent models that were used in this work instead of spatial resolution.

[3] studied the strong pressure fluctuations on the side window as a consequence of flow reattachment and separation occurring at A-Pillar, resulting in noise generation. Two different models were used for this work. The point of similarity for both models was the flat angle of inclination of 60^{o} whereas dissimilarity was at the curvature of windshield/A-Pillar; slanted sharp edge model and small semi-ellipsoidal model as shown in Figure 1.11. With the help of CFD, different Navier-Stokes Equations were implemented for predicting the vortical flow over these two models at different speeds (60, 100 and 140 km/h with 0^{o} and 15^{o} yaw angle). The analytical results were compared with experimental results and results were compared and analysis was done on the basis of mean pressure coefficient. In order to predict the local noise, boundary layer noise source model was implemented. The model used for turbulence modelling was the Realizable K-ε as this model shows good results for flows

concerning rotational, boundary layer under strong gradients of pressure, separation and reattachment.

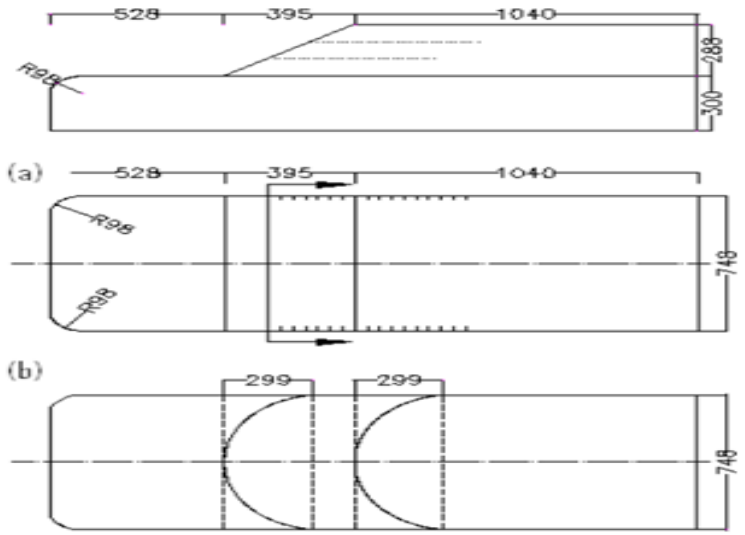

Figure 1.11: Vehicle with Slanted sharp (upper) and semi-ellipsoidal (bottom) model [3]

The results obtained in the slanted sharp edge model were that the vortex separation and reattachment occurring at A-Pillar with 0^o yaw angle was at 45^o with respect to A-Pillar. However, on comparing it with the case of 15^o yaw angle they concluded that on the leeward side, there was a larger A-Pillar vortex and wake generated in the former case than the latter as shown in Figure 1.12. In the case of the small semi-ellipsoidal model for 0^o yaw angle it was found that due to the type of geometry, the flow separates at A-Pillar and reattaches on the side window. A secondary stagnation point occurred at the upstream line. Moreover, flow separation in this case was very small when compared to slanted edge model. Because of this complex flow separation resulted in formation of two peaks in mean pressure coefficient distribution on side window. Also, the magnitude in the leeward side was much smaller than the windward side. This work conveyed that the value of maximum surface power spectra for the slanted edge mode is highest. This difference decreases on the leeward side as the result of the complex structure of flow on semi ellipsoidal model at negative yaw angle as shown in Figure 1.12.

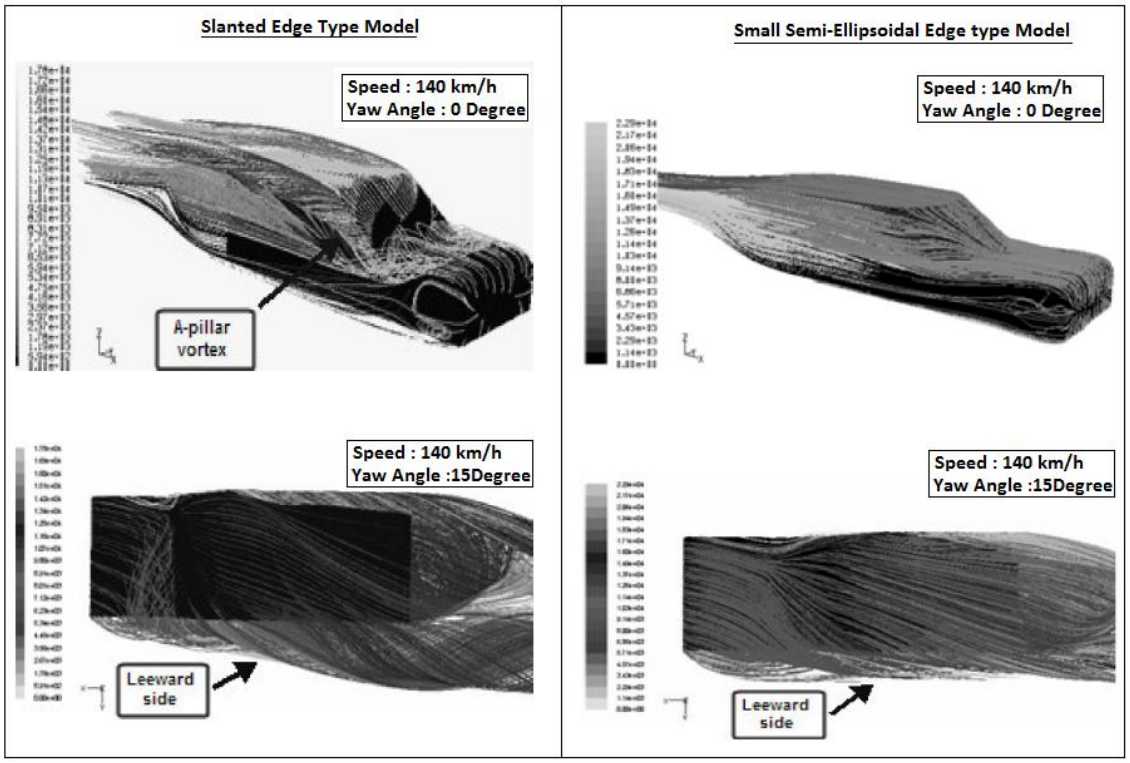

Figure 1.12: Flow around both the Models at specified speed and Yaw angle [33]

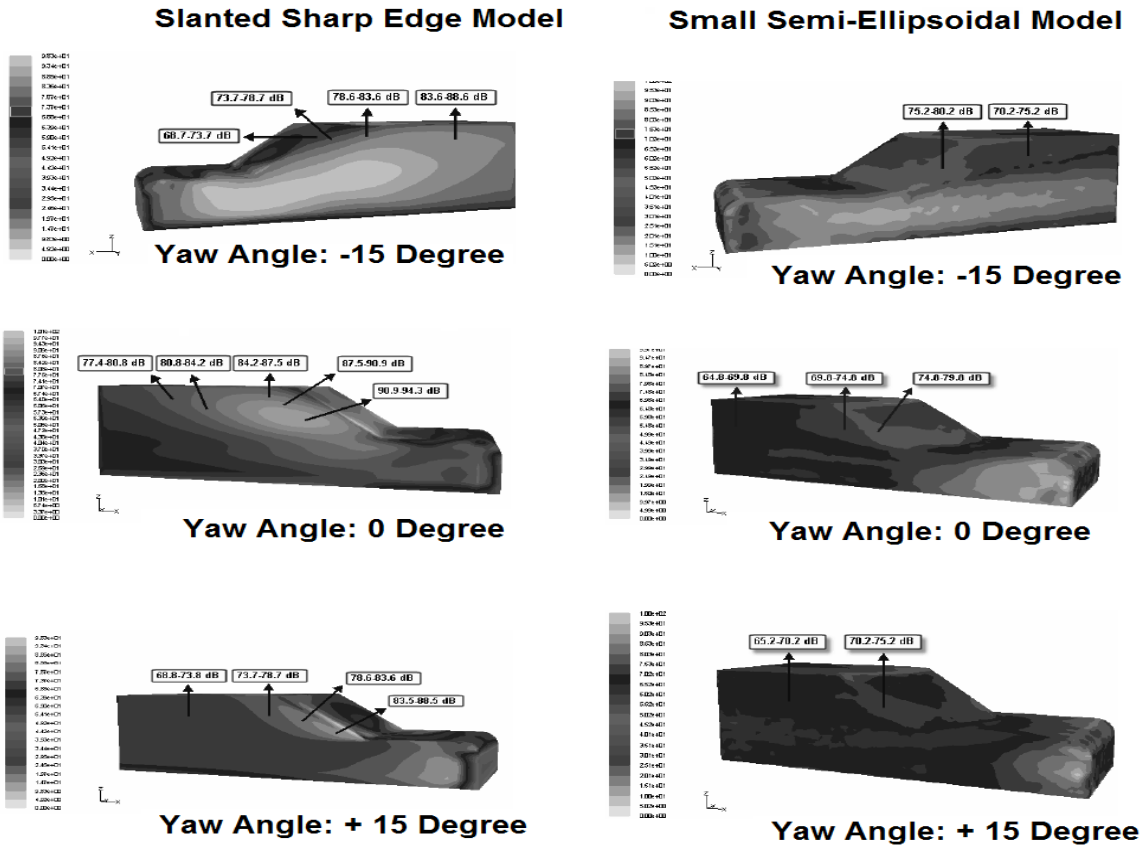

Figure 1.13: Contours of Surface Acoustic Power Level [33]

In 2011, Hagemeier [16] emphasized on vehicle soiling which also highlighted the problems arising due to the geometry of A-Pillar. The work agreed with the fact that the windshield and side window linked with A-Pillar and side mirror are the most affected regions when investigating by soiling method and the results obtained are shown in Figure 1.14 and Figure 1.15.

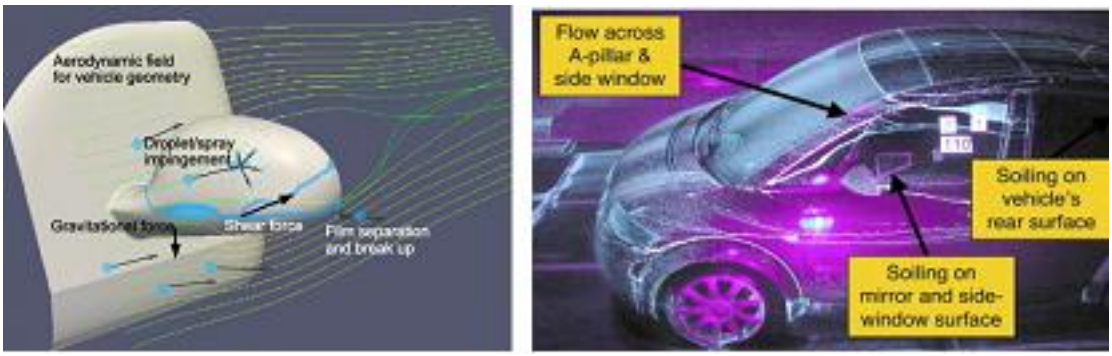

Figure 1.14 Soiling phenomena on side mirror (left); Wind tunnel experiments (right)

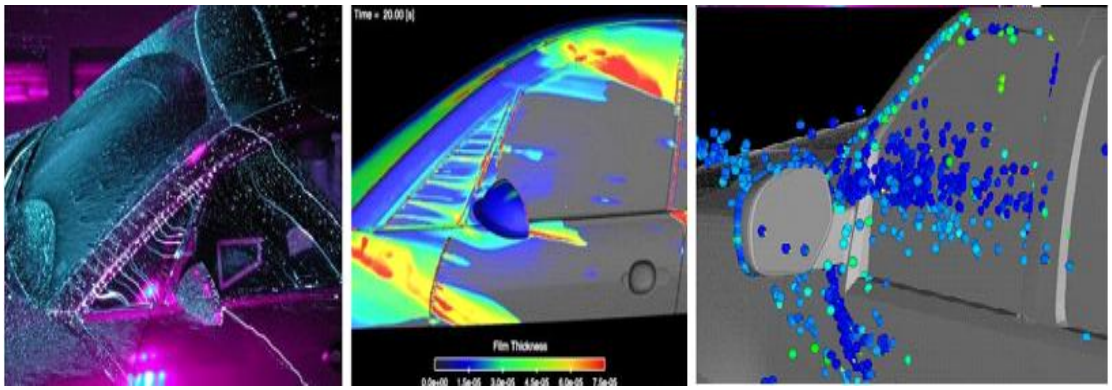

Figure 1.15 Wind Tunnel experiment (left); Soiling simulation using the Eulerian film model(middle) soiling simulation using a Lagrangian frame [16]

In 2011, a study on A-pillar vortex generation on the jaguar XF using transition turbulence models. The computational work was conducted in FLUENT v12 with standard and transition $k-\omega$ RANS turbulence models. Fine mesh was created to predict the turbulent flow over the A-Pillar [30]

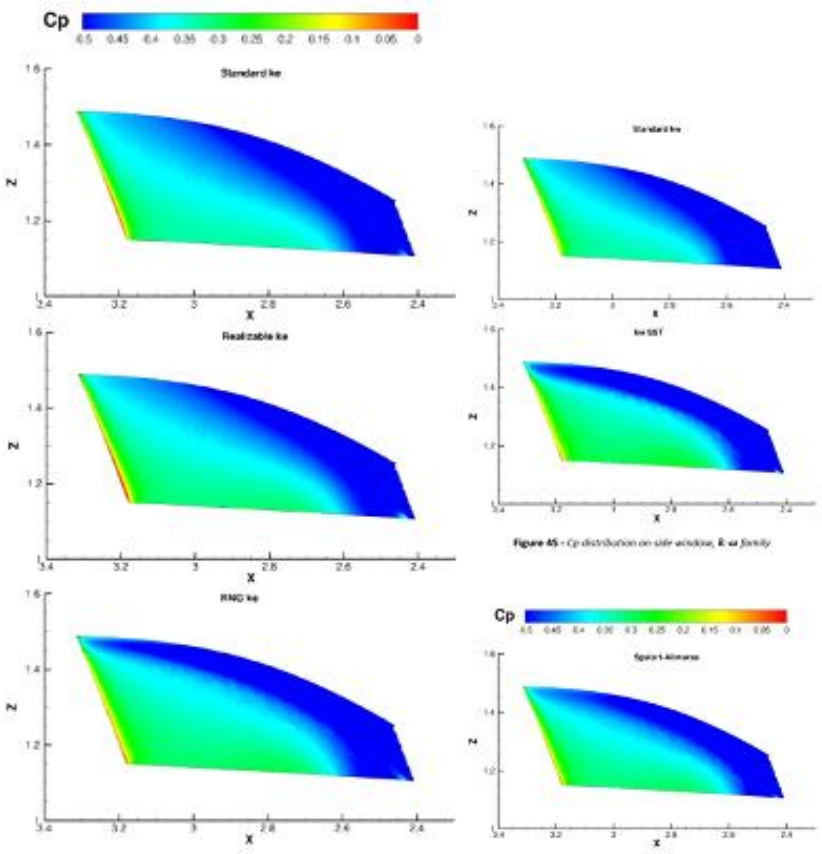

Figure 1.16 Results obtained by family (left), Standard (top right), SST (middle right) and Spalart Allmaras (bottom right) [14]

On comparing the two $k-\omega$ family models author showed that transition model generates better results than the standard $k-\omega$ model. Moreover, the results obtained by the $k-\omega$ family were further compared with the results obtained from Jaguar Land Rover (based on Lattice Boltzmann Method (LBM)). The data was extracted by locating probes on front side glass window as shown in Figure 1.17. The results showed that vortex positioning was quite similar in all the models on comparison. The data for pressure coefficient was in good agreement with that of LBM. Moreover, the thesis also included the visualization of vortex being generated behind the A-Pillar by extracting slices in x and z planes.

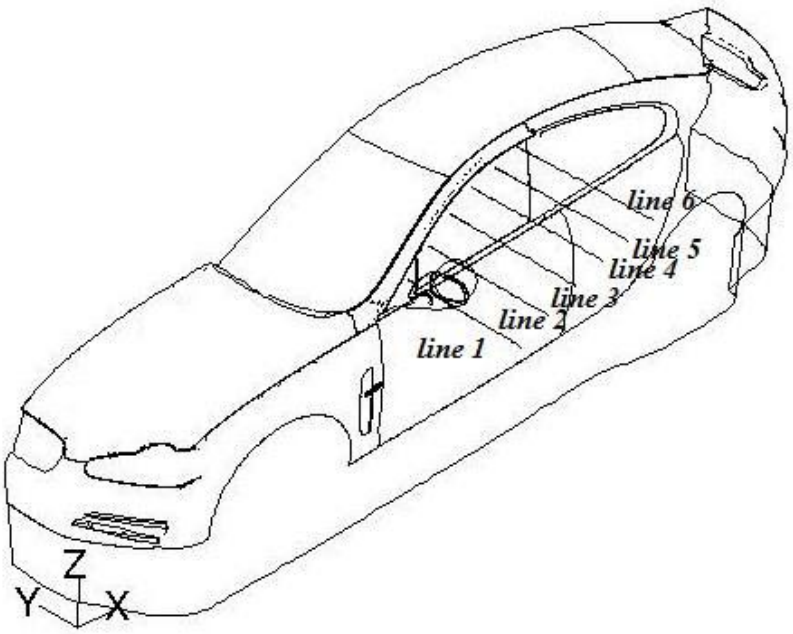

Figure 1.17 Probes location on front side glass window [30]

Figure 1.16 shows the comparison of analytical results obtained by Shah and Jaguar Land Rover.

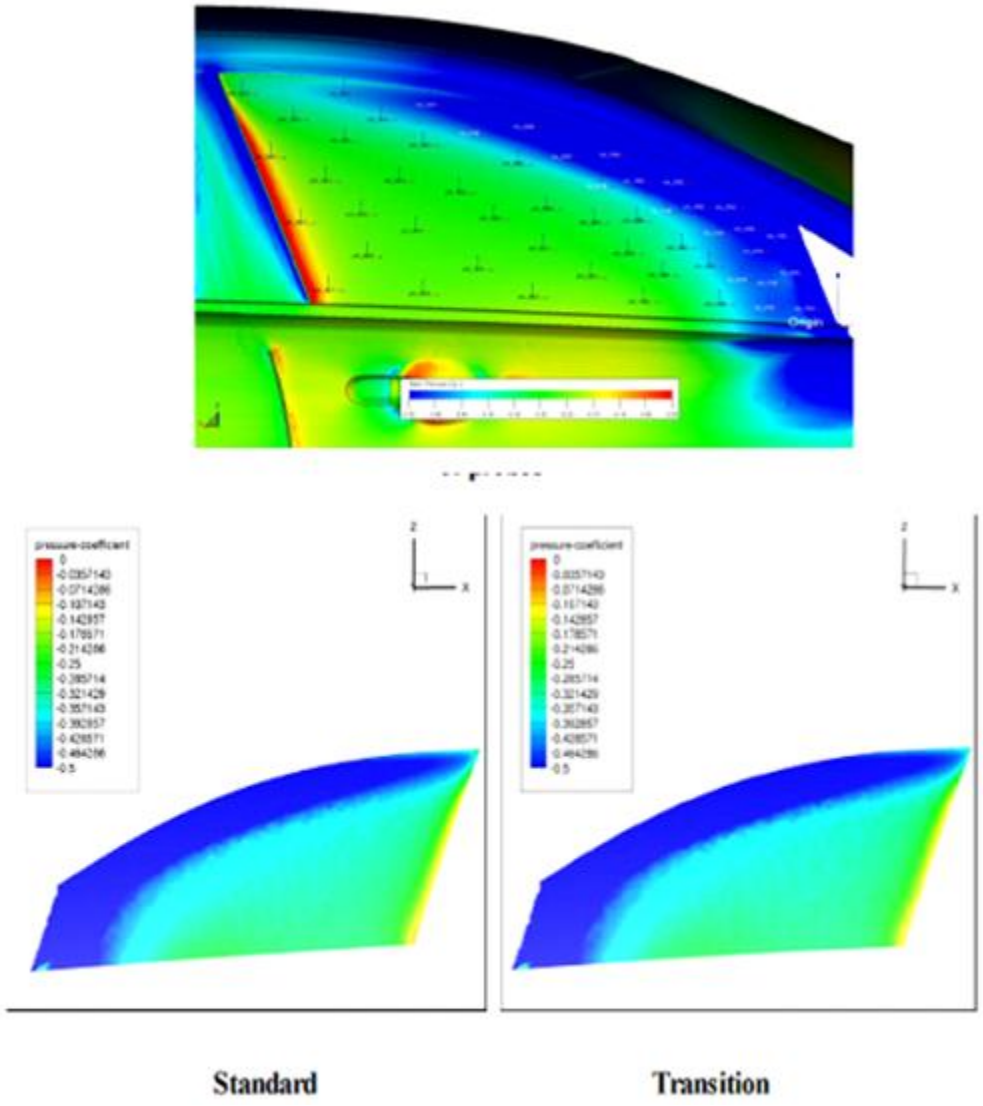

Figure 1.18: Pressure Coefficients on front side glass wondow for LBM method (upper) computational method (bottom) [30]

In 2011, Ghezzi [14] conducted a research on Jaguar XF with different RANS turbulence models such as $\boldsymbol{k-\varepsilon}$ model (Standard, Realizable, Renormalization Group (RNG); $\boldsymbol{k-\omega}$ (standard and Stress Transport (SST)) and Spalart Allmaras. A boundary layer noise source model was used to compute the SPL of this car. In This work visualized vortex formation by surface steak-line and Iso-surface of Q. Results based on the velocity plots predicted that the $\boldsymbol{k-\varepsilon}$ RNG model and $\boldsymbol{k-\omega}$ SST model showed more strong vortices than Standard $\boldsymbol{k-\varepsilon}$ and $\boldsymbol{k-\omega}$ model.

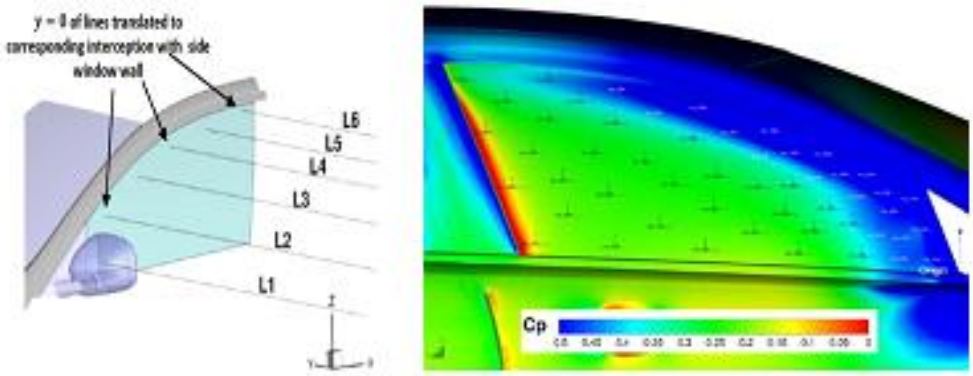

Figure 1.19: Line extraction in y-axis (left) and Pressure coefficient contour using LBM (Right) [14]

Figure 1.16 enumerates the results obtained in ANSYS Fluent for k-ε family, k-w $k-\omega$ family and Spalart Allmaras model. The results showed that the highest level of sound pressure level was near the top of joint structure of side mirror. Moreover, the side mirror wake contribution towards the noise generation and its influence on driver's ear was also discussed in her thesis. However, due to the lack of information regarding the diameter of the microphone there were some deviations experienced.

2 Governing Equations and Turbulence Modelling

This chapter discusses the evolution and development in the field of turbulence since da Vinci's time followed by different definitions of turbulence in first two sections. The section three gives a brief understanding of different length scales associated with the flow-field. The overview of different turbulence models such as RANS, DNS and LES are briefed in section 4, 5 and 6 respectively.

Note: Equations in this chapter are based on the incompressible flows.

2.1 Turbulence Background

The majority of flows such as at the boundary of earth's atmosphere, waterfalls, and smoke coming out of chimney or jet planes at supersonic speed etc. are turbulent in nature. The behaviour of turbulence in fluid flows is considered an intriguing, infuriating and important problem in classical physics [31]. Consequently, knowledge and deep understanding of characteristic behaviour of turbulence in fluid flows is imperative.

The identification of turbulence dates back since da Vinci's time. However, the its substantial progress was missing until 19th century when Boussinesq in 1877 postulated a hypothesis that Reynolds stresses $-\rho\overline{u_i{}'u_j{}'}$ are linearly proportional to the mean flow strain rate $\left(\frac{\partial U_i}{\partial x_j}+\frac{\partial U_j}{\partial x_i}\right)$ and is expressed as

$$-\rho\overline{u_i{}'u_j{}'} = \mu_t\left(\frac{\partial U_i}{\partial x_j}+\frac{\partial U_j}{\partial x_i}\right) \quad \textbf{(2-1)}$$

where μ_t is the eddy viscosity and also the proportionality constant of Boussinesq assumption.

This equation is considered as the keystone for all turbulence models revised thereafter. Osborne Reynolds [41] work was the most significant contribution in the field of turbulence. His experiment showed that in incompressible flow over the smooth surface, transition to turbulence is a consequence of Reynolds number. Taylor [44] extensively utilized the mathematics to an advance level for proposing statistical method of correlation, Fourier Transform and power

spectra. He showed that turbulence is a random phenomenon in which isotropic length scales can be analysed using statistical methods. This paper also examined experimental data generated by wind tunnel through mesh to show that turbulent flow can be observed as homogenous and isotropic.

A.N. Kolmogorov [25], [24] published the most frequently cited research papers when explaining the turbulence theory. The similarity hypothesis of Kolmogorov is discussed later.

In 1950 several books; published and revised later; on turbulence were published such as by Batchelor [8], Hinze [21] and Townsend [45]. They mainly emphasized on statistical approach towards turbulence and discussed the work conducted by Prandtl, Taylor and von Karman.

During the late 1950s the influence of coherent structures in turbulence was realized and became a noticeable point of investigation. In early 1960's, a meteorologist E.Lorenz published a paper. His research focussed on predicting the solution to Navier-Stokes Equation possessing numerous noticeable features that represents turbulence. In the same decade the closure problem as a result of unknowns in Navier-Stokes Equation were also considered.

Kraichnan published a paper wherein he make use of mathematical model from quantum theory for analysing the turbulence phenomenon whilst using Fourier series and transforms [26]. Other researches that were in the development stage in that decade included the dissipation of small scale eddies, boundary layer transitions, influence of scalar transport etc.

Other prime work in the 1970s to 1980s was the advancements in computational techniques capable of running on hardware. The first among these was suggested by Deardorff [10] for large eddy simulation and thereafter **D**irect **N**umerical **S**imulation (DNS) was proposed by Orszag and Patternson [37] and later RANS was introduced by Laundar and Spalding [27]. Owing to the lack computational facilities DNS was impossible for practical application and same was for the LES. Therefore, despite the limitations of RANS models scientists and engineers used this model. In the early 1990’s, computers that

can withstand the computational burden using LES for some applications. Since then there have been many advancements in computer capabilities. Nowadays the computers are not only efficient in solving the complex flows of higher Reynolds Number but also capable of using DNS exhibiting low Reynolds Numbers.

2.2 Definition of Turbulence

There are numerous definitions that define turbulence. Among them, da Vinci defined turbulence as:

> *"the small eddies are almost numberless, and large things are only rotated by the large eddies and not by small eddies and small things are turned by small eddies and large."*

Lewis Fery Richardson (1881-1953) described turbulence as

> *"Big whirls have little whirls that feed on their velocity, and little whirls have lesser whirls and so on to viscosity."*

Von Kerman [44] mentioned G.I. Taylorand defined turbulence as:

> *"An irregular motion which in general makes its appearance in fluids, gaseous or liquid, then they flow past solid surfaces or even when neighbouring streams of the same fluid flow past or over another"*

2.3 Length Scales in Turbulent Flows

Osborne Reynolds was the first one to introduce a statistical way of predicting the turbulence. He explained that large eddies are influenced by the mean flow properties leading towards instability which further breaks into smaller and further smaller eddies until smallest size eddy is obtained where the energy will be dissipated. Reynolds Number based on the eddy length is defined as the ratio of inertial to viscous forces

$$R_e = \frac{inertial\ forces}{viscous\ forces} = \frac{ul}{v} \quad \textbf{(2-2)}$$

The turbulent energies associated with large scales are of the order of ${u_o}^2$ and time scale $t_0 = l_o/u_o$ and the rate at which energy is transferred to small scales is ${u_o}^2/t_o = {u_o}^3/l_o$. Since the energy transfer rate should be the same as dissipation rate ε therefore, $\varepsilon \sim {u_o}^3/l_o$. The small scale eddies are uniquely defined by the viscosity (ν) and the rate of transfer, ε[25], from large eddies and are stated as

$$\eta = (\nu^3/\varepsilon)^{1/4} \quad \textbf{(2-3)}$$

$$\tau_\eta = (\nu/\varepsilon)^{1/2} \quad \textbf{(2-4)}$$

$$u_\eta = \eta/\tau_\eta = (\nu\varepsilon)^{1/4} \quad \textbf{(2-5)}$$

The Reynolds number at Kolmogorov scale is unity, i.e. $\eta u_\eta/v$ = 1.

The size of length scales existing within the domain ranging from large scale to the small scales can be approximated as,

$$\frac{l_o}{\eta} = \left(\frac{\varepsilon l_o}{v^3}\right)^{1/4} = \left(\frac{{u_o}^3 {l_o}^3}{v^3}\right)^{1/4} = {R_{el}}^{3/4} \quad \textbf{(2-6)}$$

where $R_{el} = u_o l_o/v$ based on turbulent fluctuating velocity. Similarly the time and velocity scales are written as

$$\frac{t_o}{t_\eta} = {R_{el}}^{3/4} \quad \textbf{(2-7)}$$

$$\frac{u_o}{u_\eta} = {R_{el}}^{1/4} \quad \textbf{(2-8)}$$

However, at higher Reynolds number there exists a range of scales larger than η but smaller than l_o such that $l_o \gg l \gg \eta$. which is known as Kolmogorov's second similarity hypothesis and states that " At sufficiently high Reynolds number, the statistics of the motion of scales (l) in the range $l_o \gg l \gg \eta$. have

universal form that is uniquely determined by ε and independent of ν" [25]. These eddies are slightly influenced by the viscosity. Moreover, Kolmogorov emphasized the importance of this intermediate stage and named it as the inertial range and proposed a relationship in this range in energy spectrum

$$E(K) = C_k k^{-5/3} \varepsilon^{2/3} \quad \textbf{(2-9)}$$

where C_k represents the Kolmogorov constant (value 1.4), k is the wave number and ε is the dissipation rate. Qualitative representation of these three scales have been presented in Figure 2.1

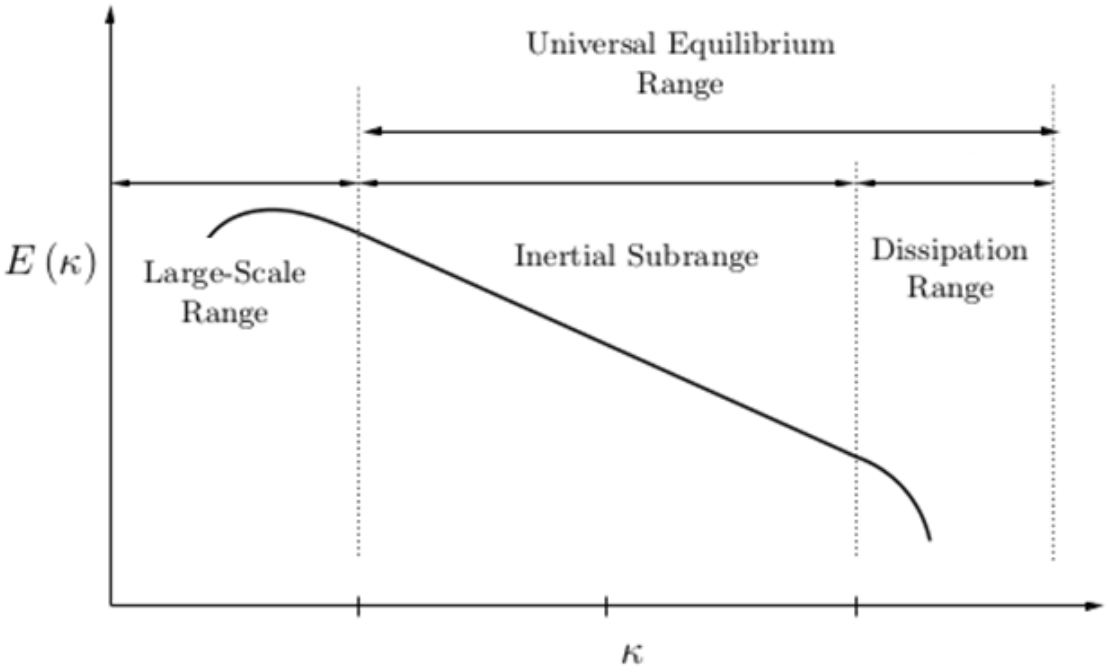

Figure 2.1 Qualitative representation of Energy Cascade

1.3 Reynold's Average Navier Stokes (RANS)

Continuity equation for an incompressible fluid flow is expressed as

$$\frac{\partial u_i}{\partial x} = 0 \quad \textbf{(2-10)}$$

and momentum equation as

$$\frac{\partial u_i}{\partial t} + \frac{\partial u_i u_j}{\partial x_j} = \frac{-1}{\rho}\frac{\partial p}{\partial x_i} + \nu \frac{\partial^2 u_i}{\partial x_j \partial x_j} \quad \textbf{(2-11)}$$

In the late 19th century, Osborne Reynolds suggested decomposing the flow properties into mean and fluctuating part. For example, velocity can be written as $u_i = \overline{u_i} + u_i'$ where (-) represents the mean and (') as fluctuating part.

On substituting this decomposition in equation (2-12), the updated equation will be

$$\frac{\partial \overline{u_i}}{\partial t} + \frac{\partial \bar{u}_i \bar{u}_j}{\partial x_j} = \frac{-1}{\rho}\frac{\partial \bar{p}}{\partial x_i} + \nu \frac{\partial^2 \bar{u}_i}{\partial x_j \partial x_j} - \frac{\partial \overline{u'_i u'_j}}{\partial x_j} \quad \textbf{(2-12)}$$

The whole Navier Stokes equation leads to 10 unknowns closed by Boussinesq assumption of eddy-viscosity. Different turbulence models in ANSYS Fluent v14.0 under RANS are Spalart Allamaras, $k-\varepsilon, k-\omega$ etc. but due to the research area of this thesis, they are not specified here.

1.4 Direct Numerical Simulation (DNS)

To obtain the full description of flow as a function of space and time, the DNS approach is used. The prime advantage of using DNS is that it does not require any additional models to close the system and it captures all scales in the domain as DNS resolves all scales; from large to the tiniest scale eddy existing in the flow-field.

Despite the advantages, DNS is very rarely used (even in academia). The computational cost associated with this approach is very high. The grid resolution required for DNS is very fine such as to capture dissipation scale

The estimation of number of points required for the whole domain is expressed as

$$N_x = \left(\frac{L_{domain}}{\Delta_x}\right)^3 \approx \left(\frac{L_{domain}}{l}\right)^3 {R_{e_l}}^{\frac{9}{4}} \quad \textbf{(2-13)}$$

where L_{domain} is the length of domain

Also, the computational time required by DNS is

$$N_t \approx \frac{T}{\Delta_t} \approx \frac{T}{\eta/u_l} \tag{2-14}$$

$$N_t \approx \frac{T}{\eta/u_l} {R_{e_l}}^{\frac{3}{4}} \tag{2-15}$$

and total cost associated with it is

$$N_{total} \propto N_t N_x \approx \frac{T}{\eta/u_l}\left(\frac{L_{domain}}{l}\right) {R_{e_l}}^3 \tag{2-16}$$

Thus the cost associated with DNS is very high and its use is limited to low Reynolds Number flows.

1.5 Large Eddy Simulation (LES)

Large **E**ddy **S**imulation (LES) targets the capability to simulate complex flows with higher Reynolds Number. In LES, the large scale eddies are directly computed whereas smaller ones are modelled using sub-grid scale models. The large scale eddies are anisotropic and transfer most of the momentum and energy into smaller eddies that are homogeneous and isotropic. The formulation of LES involves applying filtering function to the governing equation of fluid flow.. In order to filter these large and small eddies a filtering function is applied as specified in equation (2-17)

$$\bar{f} = \oint G(x, x', \Delta) f(x') dx' \tag{2-17}$$

where Δ represents characteristic filter width and G is the filtering kernel. In ANSYS Fluent v14.0, the top-hat type of filter is used that takes average of the whole volume

$$G(x, \Delta) = \begin{Bmatrix} \frac{1}{\Delta} & if\ |x'| \leq \Delta/2 \\ 0 & otherwise \end{Bmatrix} \tag{2-18}$$

On applying the filtering operation to the governing equation for an incompressible flow, the continuity equation and momentum equations are expressed as:

$$\partial \frac{\overline{u_j}}{\partial x_j} = 0 \qquad \textbf{(2-19)}$$

$$\partial \frac{\overline{u_j}}{\partial t} + \partial \frac{\overline{\overline{u_j}\,\overline{u_\iota}}}{\partial x_j} = \frac{-1}{\rho}\frac{\partial p}{\partial x} + \frac{\partial \tau_{ij}}{\partial x_j} + \vartheta \frac{\partial^2 \overline{u_\iota}}{\partial x_i x_j} \qquad \textbf{(2-20)}$$

The term τ_{ij}; recognised as sub grid scale stress; is responsible for modelling the small scale eddies. The expression for τ_{ij} appears as:

$$\tau_{ij} = \overline{\overline{u_\iota} u'_j} + \overline{u'_\iota \overline{u_j}} + \overline{u'_\iota u'_j} \qquad \textbf{(2-21)}$$

Selection of an appropriate turbulence model plays an important role in LES. The most frequently used sub-grid model based on the Boussinesq assumption is:

$$\tau_{ij} - \frac{1}{3}\delta_{ij}\tau_{kk} = -2\vartheta_{sgs} S_{ij} \qquad \textbf{(2-22)}$$

In order to come up with closure problem; $\boldsymbol{\vartheta_{sgs}}$ (sub-grid eddy viscosity) is modelled and ANSYS Fluent v14.0 provides four models of sub grid eddy viscosity. In this research the standard Smagorinsky-Lilly model was used and will be discussed.

In Smagorinsky-Lilly model the Smagorinsky constant (C_s) remains constant throughout the simulations and $\boldsymbol{\vartheta_{sgs}}$ is proportional to the square of selected length scale calculated based on equation

$$\vartheta_{sgs} = \rho L^2 |S| \qquad \textbf{(2-23)}$$

Where L is the mixing length scale and is computed as:

$$L = (kd, C_s, \Delta) \qquad \textbf{(2-24)}$$

where ‘k’ represents the von Karman constant (0.41) and ‘d’ is the distance from the wall, $\mathbf{C_s}$ is the eddy viscosity or Smagorinsky constant (specified according to the problem); taken default $\mathbf{C_s = 0.1}$ and Δ is the local grid scale. Other models available under LES in ANSYS Fluent v14.0 have not been considered in this research owing to the time constraints.

3 Computational Approach

3.1 Summary

The chapter will discuss the three grid resolutions generated for the current research project. The selected boundary conditions for inlet, outlet and walls will be discussed. The section concluding this chapter will be the numerical methods and the different errors expected to influence the simulations

3.2 Grid generation

The geometry model was provided by **J**aguar **L**and **R**over (JLR).It was amended by Ghezzi [14] [30]and Shah [30] according to the requirements such as door handles, closed underbody and side-mirror surface curvature were modified which can affect the overall quality and the skewness of the grids used.

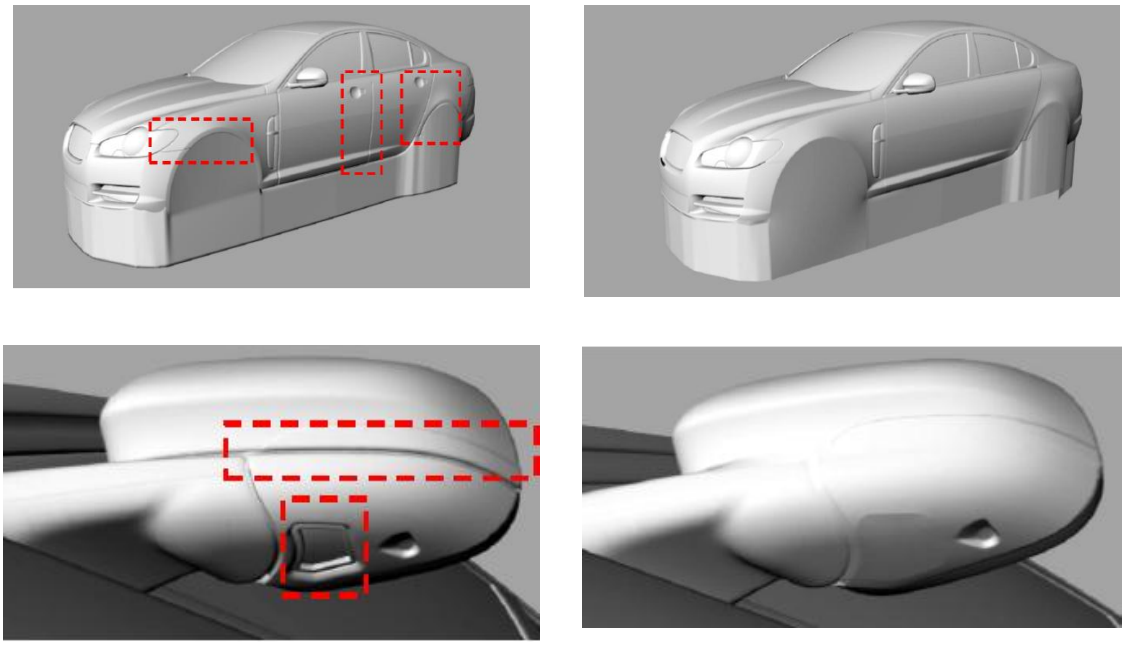

Figure 3.1 Ammended Geometry over front and door handles (top); side mirror (bottom) [14]

As the vehicle is symmetrical about the centre-line, only the half body is used for computational analysis as it will reduce meshing elements and computational burden. Figure 3.2 & Table 3.1 give an overview of vehicle dimensions and its location within the domain constructed in Ansys ICEM CFD.

Table 3.1 Dimensions of car and domain

Parameters	Dimensions (in metres)
Height of Car	1.55
Length of Car	4.96
Height of Domain	4.9
Width of Domain	3.95
Distance from the Inlet	9.3
Distance from the Outlet	19.84

Figure 3.2 Vehicle's location in domain [14]

3.2.1 Resolution requirements

Vortices over front side glass window are characterized by the strong gradient in pressure, velocity and the associated flow regimes as shown in section 4.2.1. To capture these gradients requires numerical simulation with precise grid resolution. However, refining the whole domain consumes higher computational burden. Therefore, the grid is refined locally according to the requirements. In the present work the grid was resolved locally at A-Pillar and front side glass window.

The present research aims to predicting vortex generation behind the A-Pillar which influences external wall pressure fluctuations generated on the front side glass window. To capture the flow-field and noise levels at desired locations the grid resolution should be fine enough especially at areas of interest considered

such as the hood, A-Pillar, side mirror and front side glass window. Three grid resolutions adopted for current work are specified in Table 3.2;

Table 3.2 Grid resolutions and averaged parameters

Parameters	Coarse[30]	Medium	Fine
Resolution (number of cells in millions)	2.7[30][30]	6	10
First cell height (in mm) (at areas of interest* / remaining)	0.34/ 0.34	0.25/ 0.34	0.1 / 0.34
Y^+ (at areas of interest* / remaining)	25/25	18/25	10/25
Prism layers	3	3	3
Geometric growth rate	1.2	1.2	1.2
Quality$^+$	0.77	0.82	0.96
Skewness$^+$	0.97	0.99	0.88

($^+$) 0 represents worst & 1 represents good quality elements)

(*) - front side glass wondow, A-Pillar, hood & side-mirror

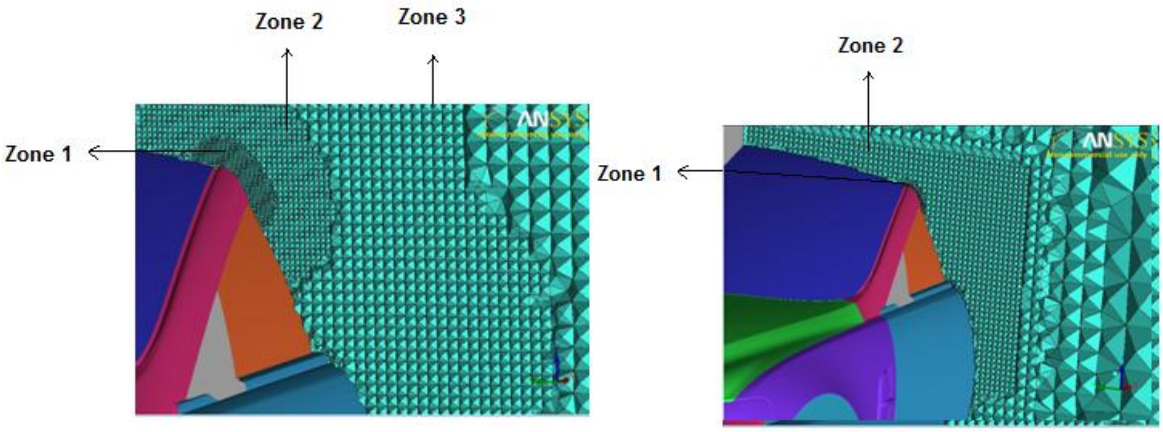

Figure 3.3 Mesh resolution for fine (left) and medium(right) case

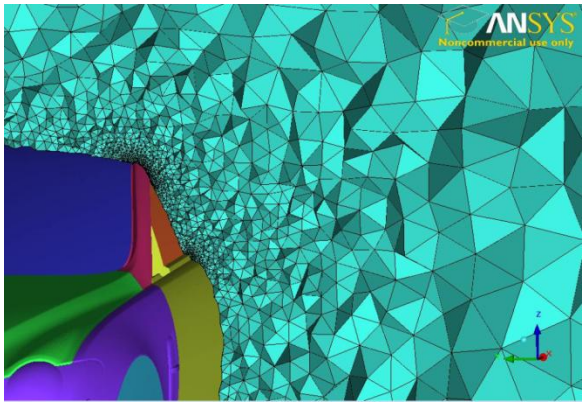

Figure 3.4 Mesh resolution for coarse case [30]

The mesh generated for the coarse, medium and fine case is shown in Figure 3.3 and Figure 3.4. The growth rate selected for tetra elements was 1.2 with most cells generated near the A-Pillar and A-Pillar wake region on front side glass window as shown in Figure 3.3 (left). The second zone with 1.2 growth rate covers the area of A-Post wake and reattachment zone over front side glass window. However, due to the skewness issues especially near the seals of the front and rear side glass windows, zone 2 did not include the area of the front side glass window up to seals. Similarly, in the medium mesh the maximum number of cells were allocated over and behind the A-Pillar at zone 1 shown in Figure 3.3 (right). Zone 2 covered the whole front side glass window.

The hybrid grid using an unstructured mesh and prism layers was generated using Ansys ICEM CFD. The tri mesh elements were generated all over the surfaces and tetra elements throughout the volume of domain with a prism layer at the boundary. Though structured mesh can also be selected but due to the ease of implementing unstructured mesh and its advantage at automatically adapting mesh near curvatures and filleted areas, the unstructured mesh with prism layers at boundary layers was adopted for current work. The motive in meshing was to achieve Y^+ = 1 at the A-Pillar, front side glass window, hood and side mirror. This will result in higher number of elements and not feasible for computations as well. Therefore, y-plus = 1 was confined to only the A-Pillar and front side glass window but this leads to poor mesh quality specifically at locations where different wall refinement met. Therefore, it was decided to initially generate mesh with a compromise of good mesh quality and number of

cells and later after importing in Ansys Fluent 14.0 the mesh can be refined at desired locations by using adaptive mesh refinement. Also, the number of prism layers was restricted to 3 only number of layers was deteriorating the overall quality of mesh. Nevertheless, highly skewed cells were located at the seals of front and rear side glass windows and side mirror structural joint though the front side glass window and side mirror were resolved

3.2.2 Boundary conditions

Boundary conditions of the physical model define the behaviour of flow variables such as pressure, velocity etc.; experienced on the boundaries and its selection plays a vital role during computational analysis. In the present work, once the mesh was generated in ANSYS ICEM CFD, the boundary conditions were assigned after importing the mesh in ANSYS Fluent 14.0. Table 3.3 gives an overview of the boundary conditions and their assigned values. The discussions on selected boundary conditions have been made in the subparts of this section.

Table 3.3 Boundary Conditions for computation in Ansys Fluent

Boundary	Specification	Assigned values
Inlet	Velocity Inlet	36 m/s
Outlet	Outflow	Flow Rate Weighting = 1
Road or Bottom wall of domain	Wall	No-slip and stationary type
Vehicle's Surface	Wall	No slip and stationary type
Domain's top and side walls	Symmetry	-

3.2.3 Inlet Boundary Conditions

Inlet boundary conditions are always the most challenging as inflow properties are convected downstream and wrong selection will directly influence the simulations. In current work, Velocity inlet **B**oundary **C**ondition (BC) have been selected. This type of BC are mostly used with incompressible flows Moreover, the location of the velocity inlet should be away from the body which will otherwise result in developing highly non-uniform inflow stagnation properties. Therefore, location of inlet for this current work is placed ahead of twice the length of car that will benefit in attaining fully developed flow.

3.2.4 Outflow

Outflow boundary conditions were selected in Ansys Fluent v14.0 as the outlet boundary condition. Outflow is selected to model the flow existing when velocity and pressure components are unavailable prior to the solution of the flow problem. One is not required to provide any condition on selecting outflow rather it extracts all the information from within the domain without an impact on upstream flow. Moreover, outflow considers zero diffusion flux for fully developed flows where velocity profile is consistent with time. However, one can select outflow boundary conditions even when the flow is not fully developed when the user is confident to expect negligible impact of zero diffusion flux at outlet.

Table 3.3 shows the inputs required to specify in ANSYS Fluent for outflow boundary conditions. Here, default value of flow rate weighting was used where value of 1 signifies equally divided flow for outflow boundary. However, if the case is concerned with two outlets; specifically when the amount of flow exiting from both outlets is not the same; one needs to specify the inputs accordingly.

3.2.5 Symmetry

Symmetry boundary condition was selected for side walls and the top wall of the domain which; in Ansys Fluent v14.0; assumes zero flux of all quantities throughout their boundary. Furthermore, symmetry involves no convective flux

for the selected walls which assumes negligible or zero effect of normal gradient of all flow variables at selected walls.

3.2.6 Wall Bounded Conditions

The model selected for this thesis considers no slip conditions when flow interacts with the surface of vehicle. The no slip boundary condition assumes tangential velocity to be zero at the walls. The grid generated is fine enough; specifically on A-Pillar and front side glass window; to capture the viscous effects on the wall.

3.2.7 Material Selection

The medium selected for flow within the domain is air. The viscosity, density and temperature of air assumes the default value in Fluent (17.894 μ Pa·s and 1.225 kg/m^3 and 298 K).

3.3 Solver Sittings:

The solver settings specified in Table 3.4 were same for all simulations using three grid resolutions.

Table 3.4 Transient Simulation Setup

Turbulence Model	**LES Model (Standard Smagorinsky-Lilly Model)**
Fluid Property	Air
	Density-1.225 kg/m^3
	Kinematic Viscosity- 1.7894E-05 kg/(m·s)
Transient Formulation	Non-Iterative Time Advancement (NITA)
Pressure-Velocity Coupling	SIMPLEC
Gradient Method	Least Squares Cell-Based
Inlet	Velocity inlet; V = 36 m/s
	No Pertubations
Outlet	Outflow
Time Step Size	100 µ sec

3.3.1 Pressure-Velocity Coupling

For an incompressible flow the prediction of pressure has always been tricky; as density is constant and the momentum equation always requires a value of pressure for solving the velocities; until [39] proposed a pressure velocity coupled method which has been incorporated in Ansys Fluent v14.0. This method is known as the pressure correction method. In this method, initially a guess for pressure is made and later with an iterative process the correct pressure value is obtained and at the same time velocity is updated and the process continues until convergence is achieved. Different pressure correction methods available in Ansys Fluent v14.0 are **S**emi **I**mplicit **M**ethod for **P**ressure **L**inked **E**quation (SIMPLE), **S**emi **I**mplicit **M**ethod for **P**ressure **L**inked **E**quation **C**orrected (SIMPLEC) or **P**ressure **I**mplicit with **S**plitting of **O**perators (PISO). In

current work, SIMPLEC pressure correction method was implemented as it helps in achieving convergence more quickly.

The SIMPLEC method is capable of handling higher skewed grid; as in this case; and is faster than the SIMPLE method. The algorithm for SIMPLEC; as shown in Figure 3.5; is the same as of SIMPLE but the difference lies in the way coefficient $d_{i'j}$ is calculated. (3-1) and (3-2) present the velocity correction equation and the way of calculating coefficient $d_{i'j}$ using SIMPLE and SIMPLEC method of pressure-velocity coupling.

$$u_{i,j} = d_{i',j}\left(p'_{i-1,j} - p'_{i,j}\right) \quad \textbf{(3-1)}$$

$$d_{i',j} = \begin{cases} = \frac{A_{i,j}}{a_{i',j}} & SIMPLE \\ = \frac{\boldsymbol{A_{I,j}}}{\boldsymbol{a_{i',j} - \sum a_{nb}}} & SIMPLEC \end{cases} \quad \textbf{(3-2)}$$

Although, Pressure-Implicit with Splitting of Operators (PISO) is also applicable but the selected time step size in the current work is very small (of the order of 10 - 100 µsec) and can result in higher computational expenses therefore SIMPLEC method was opted.

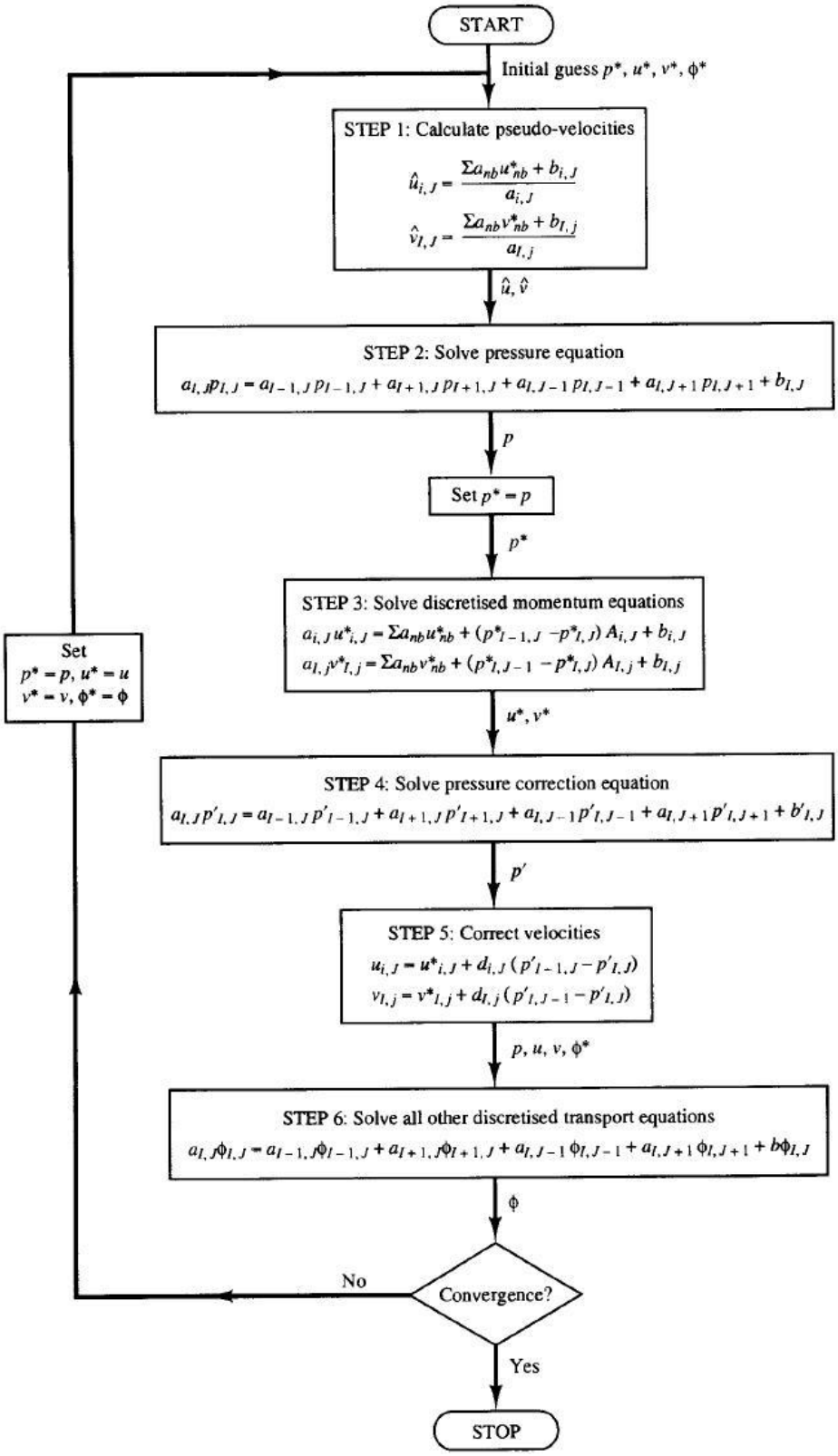

Figure 3.5 SIMPLEC Algorithm [15]

3.3.2 Spatial Discretization

Ansys Fluent v14.0 is based on the control volume based approach for converting the general scalar transport equation into algebraic form as expressed in Equation 3.3.

$$\int_V \frac{\partial \rho \phi}{\partial t} dV + \oint \rho \phi \vec{v}.d\vec{A} = \oint \Gamma_\phi \nabla \phi.d\vec{A} + \int_V S_\phi dV \qquad \textbf{Equation 3.3}$$

where ρ is the density, v is the velocity vector, $\vec{A}$ is the surface area vector, $\nabla\phi$ is gradient of ϕ, Γ_ϕ is the diffusion coefficient for ϕ and S_ϕ is the source of ϕ per unit volume.

The control volume technique integrates the transport equation about each control volume, resulting in discrete equations that conserve each quantity on a control volume basis. The numerical scheme is fully implicit adaptable to both structured and unstructured grid. For LES the default spatial discretization scheme is the Bounded Central Difference (BCD) Scheme owing to its advantage of lower numerical diffusion. BCD is based on **N**ormalized **V**ariable **D**iagram (NVD) approach discussed in [28]. Moreover, when LES turbulence model is selected for computations in Ansys Fluent v14.0 the convective discretisation schemes for all transport equations is switched to BCD.

3.3.3 Time Discretization:

When using the time dependant computations the governing equations should be discretised in space and time. Time discretization involves integrating every term of governing equations over every time step Δt. In pressure based solvers (current work) the time discretization error is determined by temporal desitization and the type of advancement scheme adopted. Second order Non Iterative Time Advancement (NITA) method was adopted for current simulations as shown in Equation 3.4 and algorithm of NITA in Figure 3.6.

$$\frac{3\phi^{n+1} - 4\phi^{n} + \phi^{n+1}}{2\Delta t} = F(\phi) \qquad \textbf{Equation 3.4}$$

where ϕ is the scalar quantity, n is value at time step t, $n+1$ is the value at time step $t+\Delta t$, $n-1$ is the value at time step $t-\Delta t$, $F(\phi)$ is the spatial discretization. This scheme only requires one outer iteration per time-step which speeds up the time dependant simulations [7].

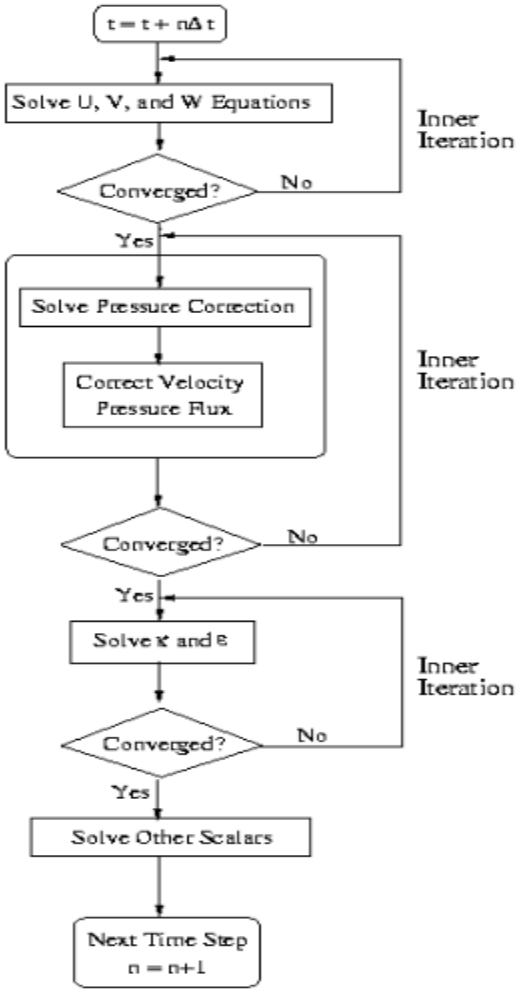

Figure 3.6 NITA Algorithm [7]

4 Computational Results and comparison

The pictorial overview of the computational methodology adopted is depicted in Figure 4.1. Firstly, grid convergence study was conducted on the basis of residuals and drag Secondly; the qualitative analysis includes flow visualization over the entire vehicle using different visualization methods. Later in this section vortex identification behind the A-Pillar will be presented using 3-D and surface streamlines slices and iso-surface of Q visualization techniques. Finally, the quantitative analysis will focus on comparing the averaged pressure data extracted at 51 probes (flush mounted) located over the front side glass window and later compared with the data provided by JLR. This section will also cover the comparative study of sound pressure levels generated at 10 probe locations over the front side glass window with aero-acoustic wind tunnel (AWT) results provided by JLR.

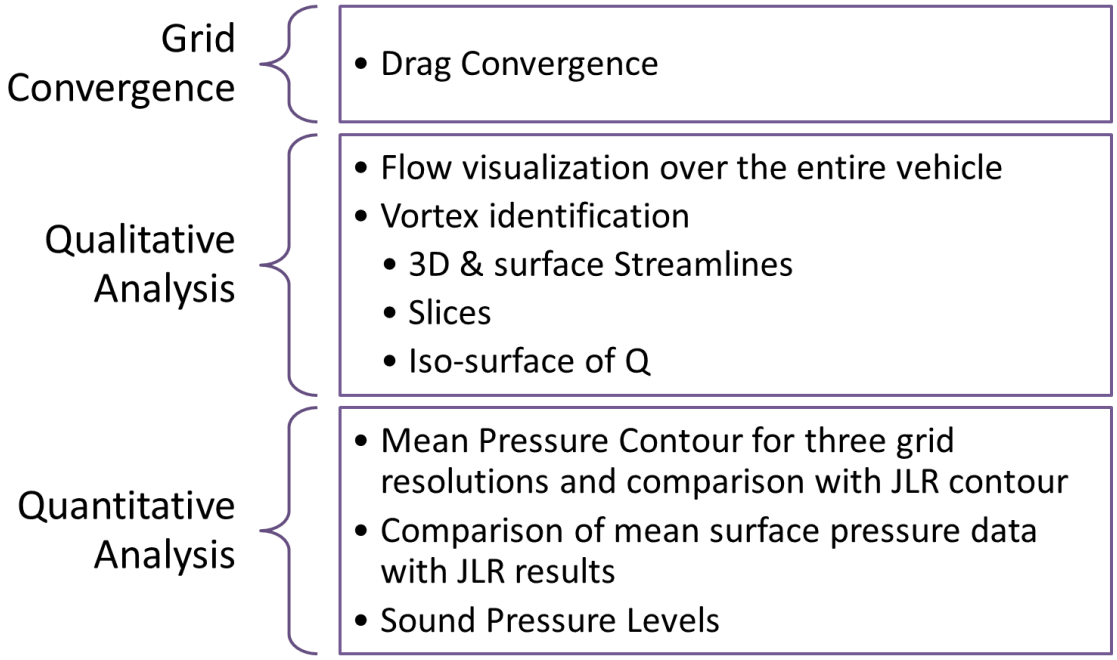

Figure 4.1 Pictorial view of computational Results and Discussion

4.1 Simulation Set-up

Prior to time dependant solution steady state RANS simulations; using K-ω SST model; were run for enough time to initialize the solution. Table 4.1 shows the inputs used for running time independent simulations.

Table 4.1 Steady State Simulation Setup

Turbulence Model	K-ω SST Model
Fluid Property	Air
	Density-1.225 kg/m^3
	Kinematic Viscosity- 1.7894E-05 kg/(m·s)
Pressure-Velocity Coupling	SIMPLE
Gradient Method	Least Squares Cell-Based
Inlet	Velocity inlet; V = 36 m/s
	Turbulence intensity-1.9%
	Turbulence Length scale-0.25
Outlet	Outflow

The residuals convergence was set to maximum value of 10^{-4} and solution run until this criteria was met and all residuals stabilizes. The residuals stabilize after 6000 iterations to a maximum value of 10^{-5}.

The simulations were thereafter switched to time dependant computations using a built in command in Ansys Fluent 14.0 *init-instantaneous-vel* that provides more realistic instantaneous velocity fields specially when switching from time independent to LES simulations. The inputs for LES simulations are enlisted in

table 1.2. LES using Dynamic Smagorinsky-Lilly model was selected owing to its advantages over the standard model as discussed in the previous chapter.

The first step for time dependant simulations is to calculate the time step size required for simulation on the basis of which time required for different grid resolutions is approximated.

4.1.1 Time step size calculation

The time step size was calculated using the Courant-Friedrich-Lewy condition. Since the current work is based on implicit time integration therefore the Courant-Friedrich-Lewy condition was not restricted to the value of 1. However, the time step size was calculated on the basis of grid spacing for fine case; as specified in Table 3.2; and using CFL = 1 as;

$$CFL = \frac{u\Delta t}{\Delta x}$$

$$\leftrightarrow \Delta t = \frac{CFL \times \Delta x}{u} \approx 2.77E-06\ sec$$

Here, u is the free-stream velocity (36 m/s), Δx is the grid spacing. The time step size calculated at CFL=1 yields very lower time step and demands higher computational burden. Therefore, higher time step size of 1E-04 sec was used which yields CFL of around 36 for fine grid case.

4.1.2 Physical Time

Physical time is defined as the time required for covering the entire length of the car based on characteristic length and free-stream velocity and is expressed as:

$$time\ (t_{car}) = \frac{charaterisitic\ length\ of\ the\ vehicle}{free-stream\ velocity\ (U_\infty)} = \frac{4.961}{36} = 0.13sec \qquad \textbf{(4-1)}$$

This implies that 0.13 second of real-time is required to simulate the flow over the car once which includes 1300 time steps .Also, in order to get statistical convergence it was required to run at least characteristic times (approximately $10\ t_{car}$) which corresponds to 1 sec flow-time.

4.1.3 Computational Time

The computational time required to complete one flow over the vehicle; for coarse, medium and fine grid; is presented is table. The results were simulated using high computing performance (HPC) server

Table 4.2 Time required for numerical simulations using coarse, medium and fine grid

Simulation Run	**Computational Time (hours)**		
	Coarse	**Medium**	**Fine**
One flow over the vehicle (1 t_{car})	18.0	40.0	72.0
Until statistical steady state	304.0	674.0	1216.0
Averaging over 10 t_{car} after statistical steady state	180.0	400.0	720.0

The values listed in Table 4.2 were extracted by running 1300 iterations (1 t_{car}).using 16 cores.

4.2 Qualitative Analysis:

4.2.1 Flow Physics

The results presented in this section are computed using LES simulations. The main area of interest is the vortex formation behind the A-Pillar but before that flow over the vehicle will be discussed briefly. The flow visualizations presented are extracted by post-processing the computational results; for 10 tcar flow-time after the statistical steady condition; in CFD-Post. Pressure and velocity contours, surface and 3-D streamlines are used to visualize the flow behaviour over the vehicle. The flow physics discussed here involves visualizations based on finest case if not otherwise stated.

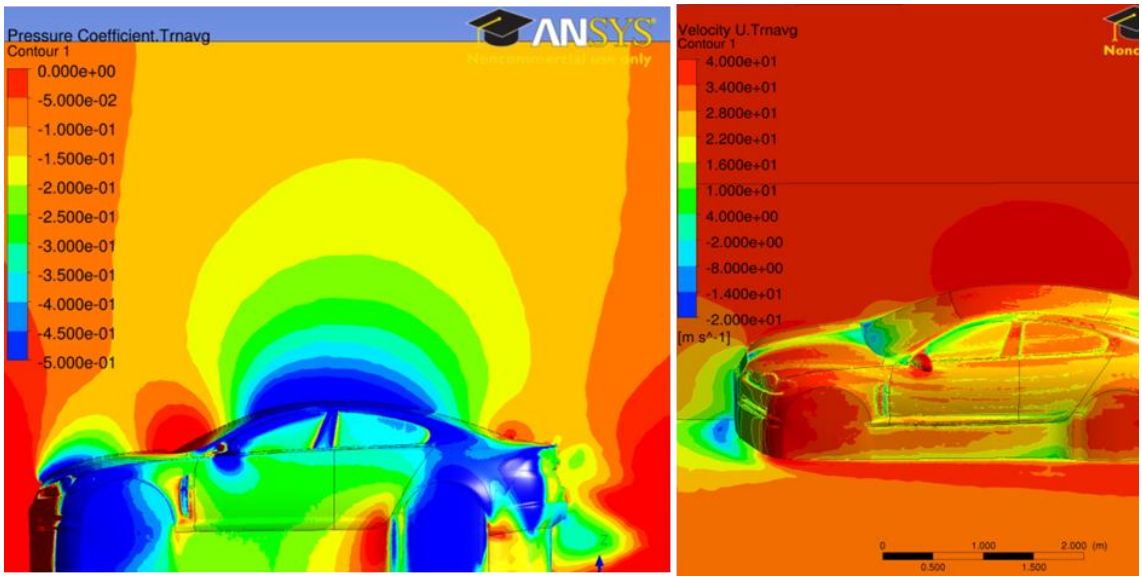

Figure 4.2 Pressure (left) and X-Velocity (right) plot over the vehicle

- Figure 4.2 shows the pressure and X-velocity contours over the vehicle. By post processing the results obtained, following features were observed on the basis of time averaged contours and streamlines.
- As the flow interacts with the front of the vehicle at blanking area sudden increase in the pressure is noticed as a result of stagnation point. However, this does not reflect a true representation of reality since current work does not considers air from the underside of the vehicle.

- The importance of curvatures on the hood can be visualised using 3-D streamlines in Figure 4.3 which directs the streamwise flow towards midway of front door thereby preventing higher sound level generation over front side glass window due to oncoming flow. However, the small separation visualised above the front grille in Figure 4.4; also seen in x-velocity contour in Figure 4.2; is due to the front intake being closed in this simplified computational model.

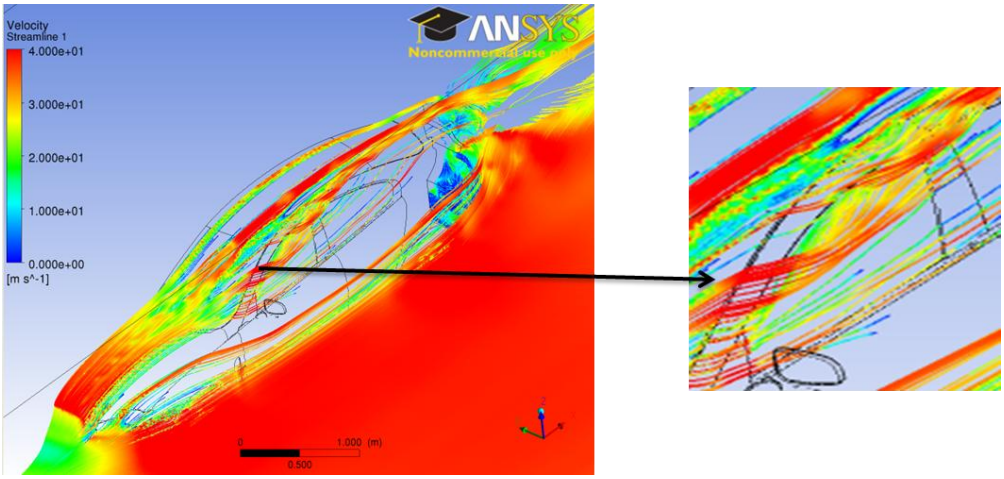

Figure 4.3 3-D streamlines in xy plane at z = 0.5 m

The cowl vortex formation at the base of front windscreen, primarily due to the inflection between bonnet and windscreen; depicts wider cowl vortex near the centreline. Further in the negative spanwise direction; near the hood/windshield area; the cowl vortex converges as presented by surface streamline in Figure 4.4 and later contributes in side mirror wake near front side glass window via root of A-Pillar as shown in vortex identification section. Thereafter, the flow reattaches over the windshield and due to the curved design of windshield the flow is directed partially on the roof and partially towards the A-Pillar as visualised in Figure 4.3 and Figure 4.4 which later contributes in the rear wake of the vehicle.

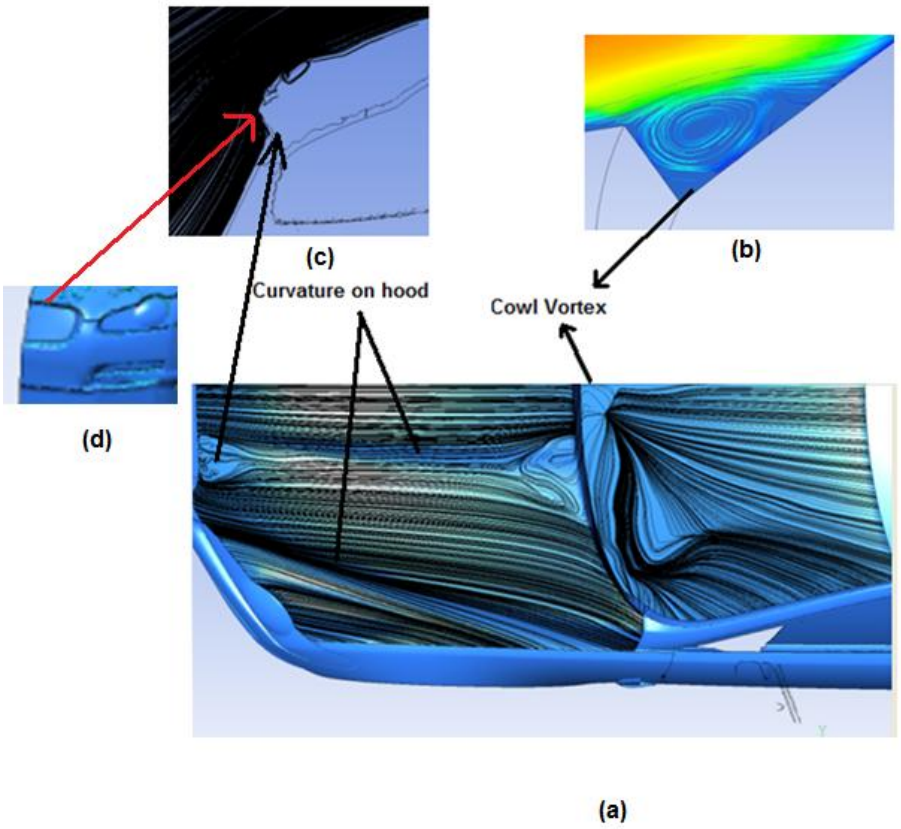

Figure 4.4 (a) Surface Streamlines over hood and front windshield area; (b) zoomed cowl vortex; (c) bubble formation at front of hood); and (d) design of radiator grill and front hood

- The flow remains attached over the roof until the last stagnation point at the rear windshield is incurred as visualised in Figure 4.2
- Surface streamlines at centreline gave better understanding of rear wake where two counter rotating vortices were noticed in Figure 4.5. However, the real situation will be different as current work excludes airflow from the underside of the vehicle and considers only half model owing to the area of research.

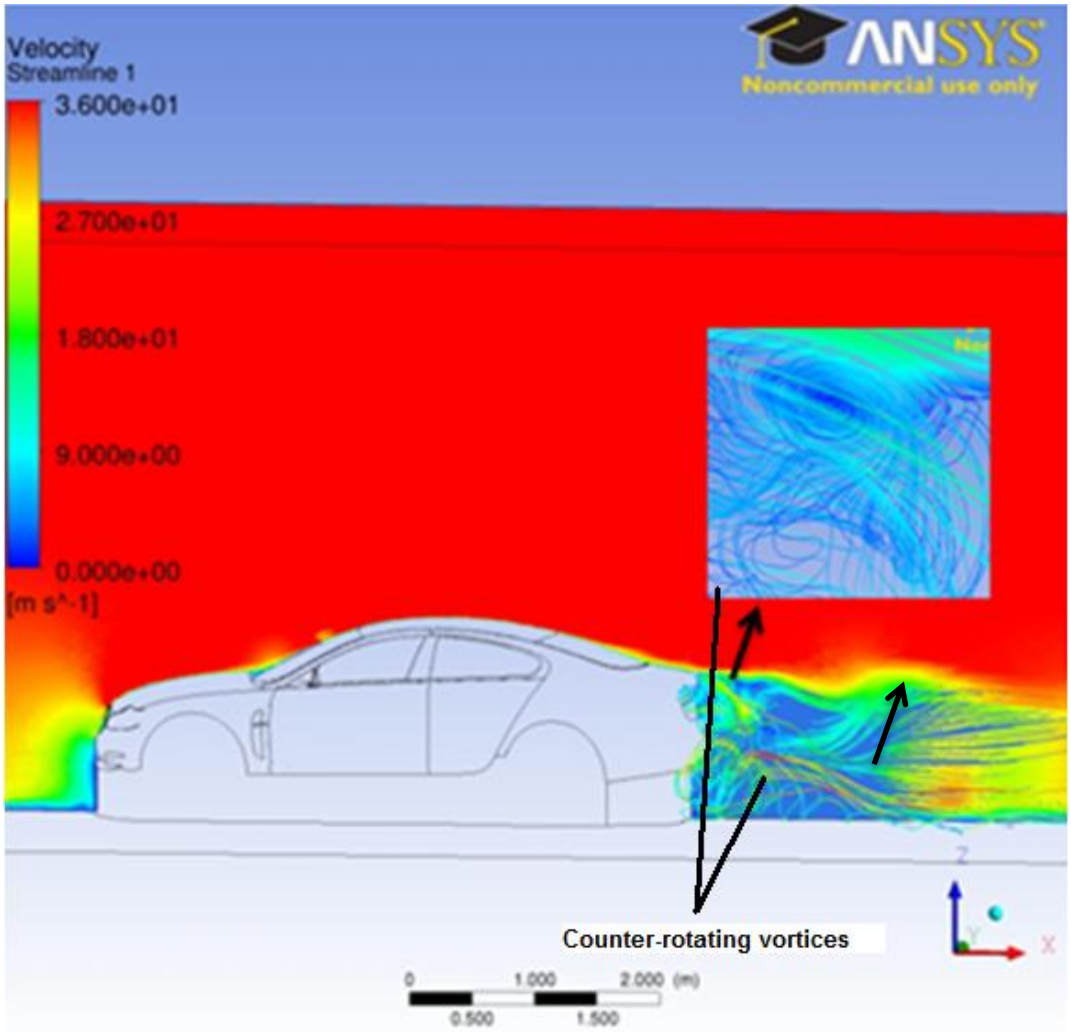

Figure 4.5 Surface streamlines at centreline with counter rotating vortices at rear wake

Flow visualization presented in section 4.2.1 clearly illustrates the vortex formation behind A-Pillar and rear wake. The rear wake will not be considered here as illustrated in section 4.2.1. To get more insight into vortex formation behind A-Pillar different visualization methods were used:

4.2.1.1 Streamlines:

Streamlines are widely used to present and analyse the turbulent structures experienced within the domain considered. Streamlines are basically the lines drawn in such a way that at any point in space is parallel to fluid's instantaneous velocity vector at that point. 3-D and surface streamlines are used to visualize

the separations and reattachments experienced within flow domain. As discussed in section 4.2.1 flow visualised using streamlines revealed locations prone to unsteadiness. To get closer view of unsteadiness experienced over the front side glass surface, surface streamlines were extracted as shown in Figure 4.6. Flow regime over the front side glass surface visualised by the current work correlates well with fluorescence visualizations carried out in full scale wind tunnel at MIRA and computational results extracted by JLR using PowerFLOW. Separation on the surface of A-Pillar, flow directed by the under mirror surface, cheater re-attachment line and A-Pillar vortex entrainment generated similar trend visualised in CFD results of [11]. However, size of A-Pillar vortex was over-predicted by the current fine grid in comparison to fluorescence as well as CFD results. Side Mirror wake near the side mirror location and further upstream in positive x-direction confirms the same trend as shown Figure 4.6 (a) & (c).

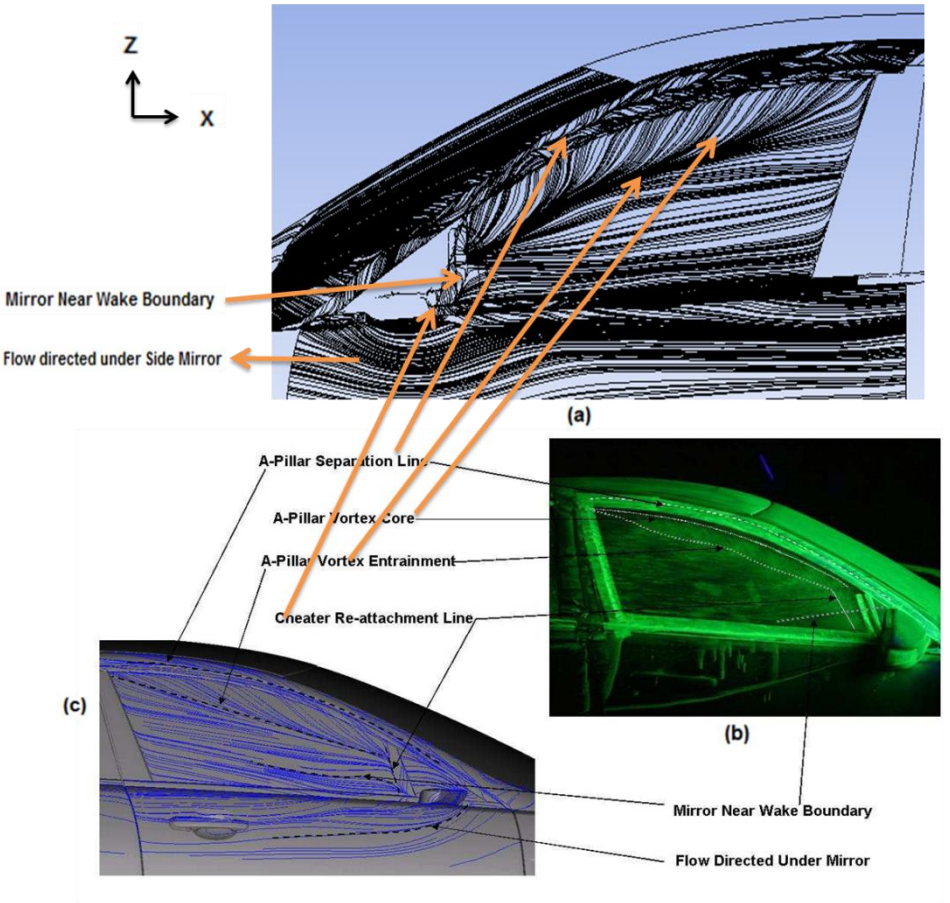

Figure 4.6 Flow regimes over front side glass window using (a) post-processing of fine mesh(current work); (b) Flouroscence flow visualization in FSTW at MIRA [11]**; and (c) Exa PowerFLOW software used by JLR** [11]

4.2.1.2 Slices:

Extracting slices gives a better and closer understanding of the flow-field. In the current work, slices were extracted to visualize the flow field behind the A-Pillar, slices are extracted in yz plane at certain distances; over the front side glass window as shown in Figure 4.7. The origin lies at the front of vehicle as shown in Figure 1.1. These slices are presented with surface streamlines coloured by time averaged pressure coefficient that can clearly reflect the extent of vortex generated over this region.

Six slices were extracted in yz plane over the front side window as show in Figure 4.7.

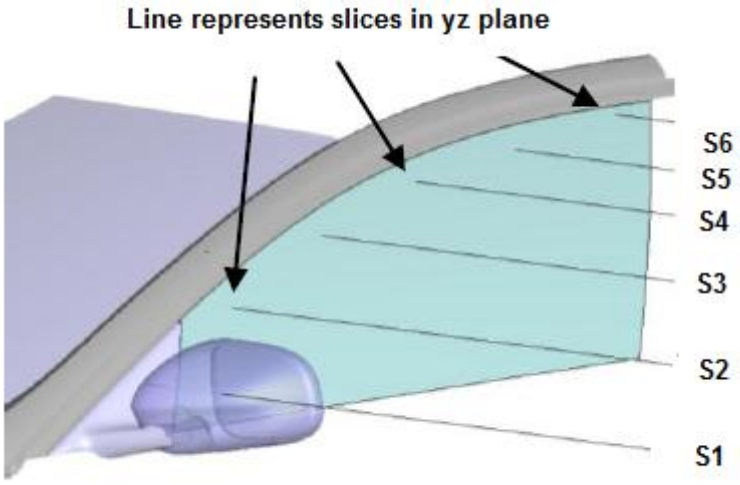

Slice	x-axis
1	2.375
2	2.55
3	2.725
4	2.9
5	3.075
6	3.25

Figure 4.7 Slice Location over front side glass window

Surface streamlines coloured with pressure contour were extracted in yz plane at x = 2.375 which covers the top portion of side mirror as shown in Figure 4.8. The reason for this slice was to capture the streamwise flow along with influence of the root of the A-Pillar and cowl vortex directed from hood/windshield area. The pressure coefficient predicted for all the mesh resolutions is approximately the same. The small separations above and below the side mirror structural joint and on either side of side mirror were well captured by all mesh resolutions. However, the coarse mesh over predicted the pressure levels near the right side of side mirror as compared to medium and fine mesh

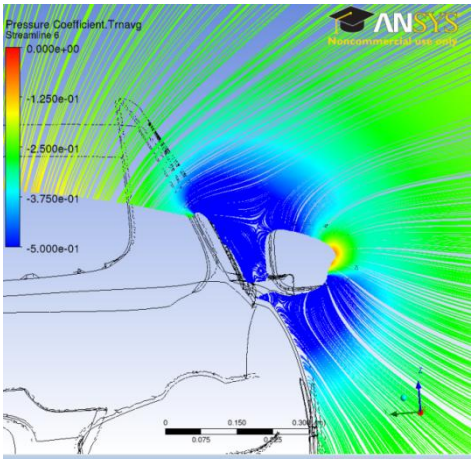

Coarse

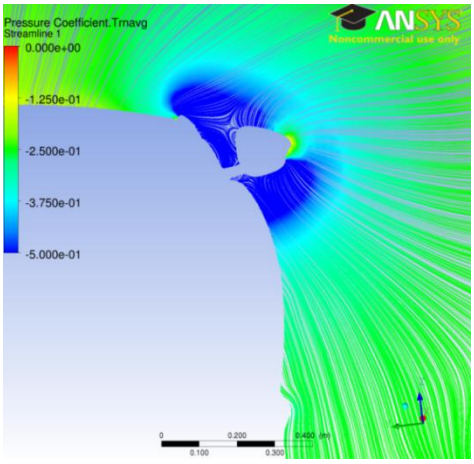

Medium

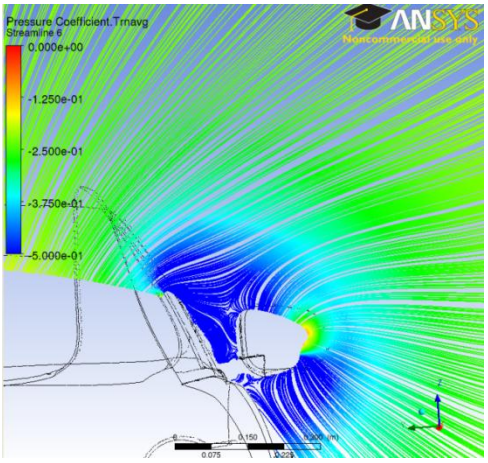

Fine

Figure 4.8 Slice 1 with surface streamlines in yz plane at x = 2.375

Slice 2 extracted at x = 2.55 over from side glass surface differentiates side mirror wake for three grid resolutions. Only fine case was able to capture the vortex formation (secondary vortex) caused by side mirror structural joint; shown in Figure 4.8; that later directs towards front side glass surface (shown in slice 3). The separation over upper surface of side mirror and side mirror wake was captured by all grid resolutions. However, the cheater re-attachment line formed as a result of combined effect of oncoming flow over side mirror and root of A-Pillar as shown in Figure 4.6; was captured by the fine mesh case only.

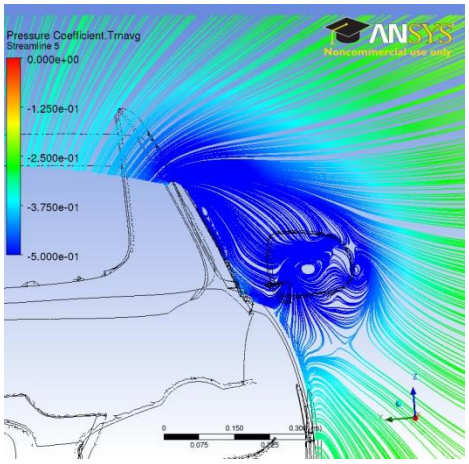

Coarse

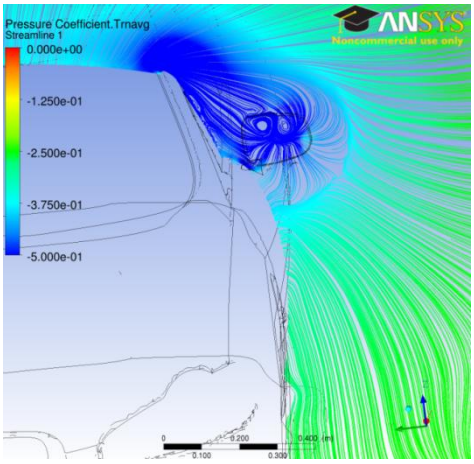

Medium

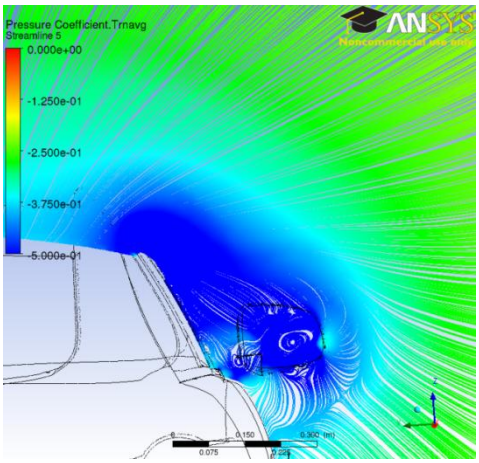

Fine

Figure 4.9 Slice 2 with surface streamlines in yz plane at x = 2.55

From slice 3 extracted at x = 2.725 over front side glass surface the vortex formation at the A-Pillar wake was visualised in all mesh cases. Clear and distinguished flow fields captured by fine mesh case for side mirror wake, side mirror structural joint.

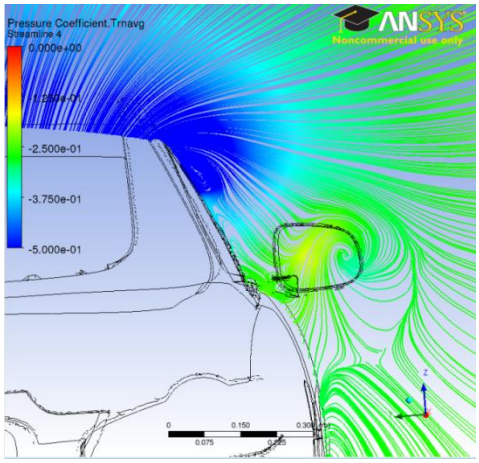

Coarse

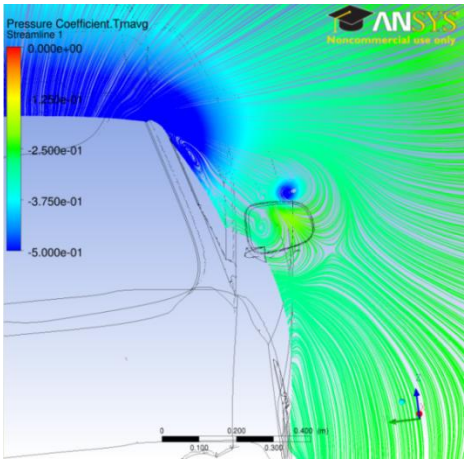

Medium

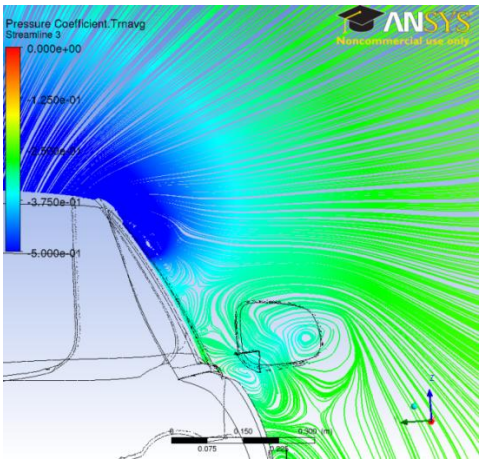

Fine

Figure 4.10 Slice 3 with surface streamlines in yz plane at x = 2.725

Noticeable points on slices 4, 5 and 6 extracted over front side glass surface include:

1. A-Pillar wake vortex grows further downstream of front side glass surface which leads to an over-prediction of the negative pressure coefficients as justified in the quantitative analysis section
2. Primary vortex formation at the side mirror wake suppresses the secondary vortex further downstream as depicted in Figure 4.11, Figure 4.12, and Figure 4.13

3. Slice 5 shows the combined effect of the secondary vortex of side mirror wake and reattachment zone near the middle of front side glass window
4. Slice 6 shows a high pressure coefficient region at the middle of front side glass surface due to the flow interaction over the bulged surface of B-Pillar.

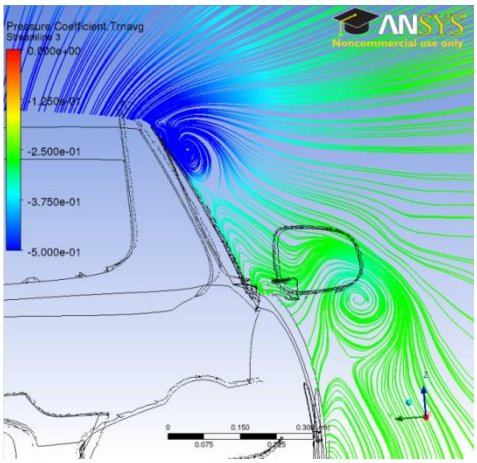

Coarse

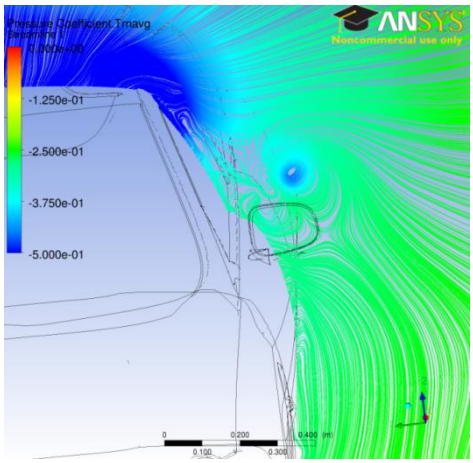

Medium

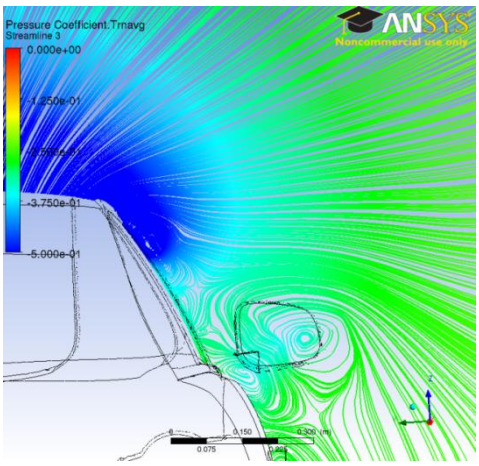

Fine

Figure 4.11 Slice 4 with surface streamlines in yz plane at x = 2.9

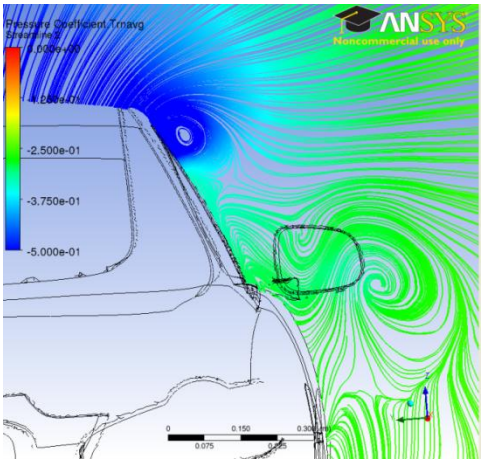

Coarse

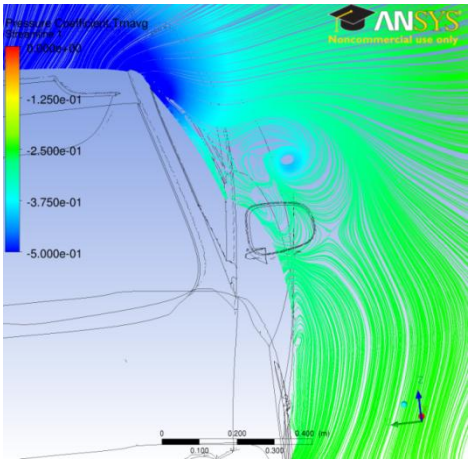

Medium

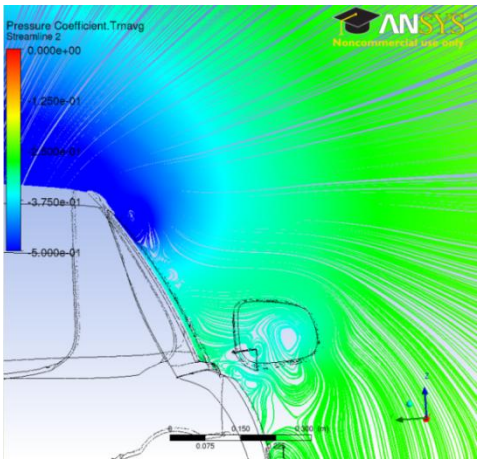

Fine

Figure 4.12 Slice 5 with surface streamlines in yz plane at x = 3.075

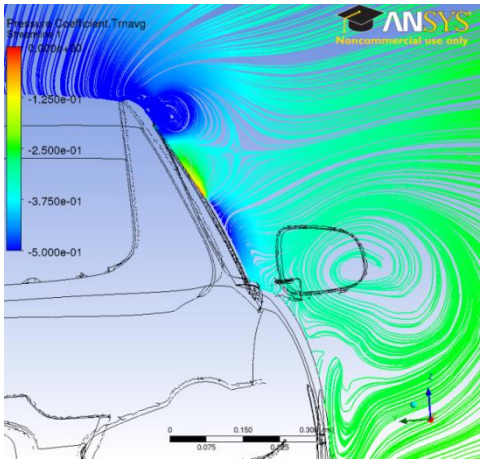

Coarse

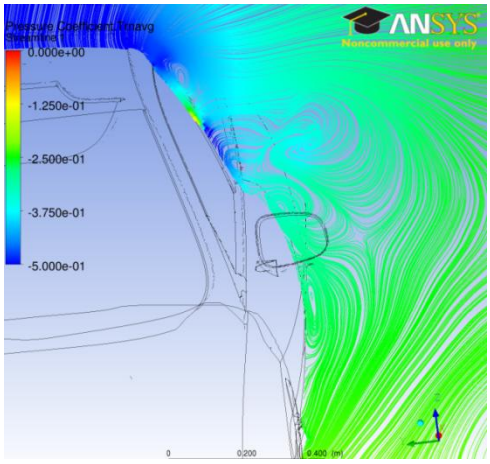

Medium

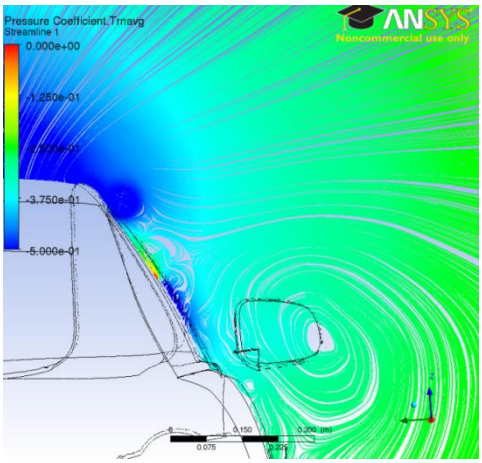

Fine

Figure 4.13Slice 6 with surface streamlines in yz plane at x = 3.25

4.2.1.3 Iso-surface of Q:

Vortices over the front side glass window are characterized by the strong gradient in pressure, velocity and the associated flow-field.

To capture these gradients a numerical simulation with appropriate grid resolution is a prerequisite. In the current case refining the entire domain demands a higher computational burden and cost associated. Therefore, the grid is resolved locally in the important locations such as the A-Pillar and front side glass window.

The conical vortex formation over the front side glass surface was visualised using iso-surface of Q method (Q-Criterion).

The Q-criterion (second invariant of velocity gradient) is widely used to visualize the turbulent (concurrent) fields for 2-D and 3-D flow regimes; proposed by [23]. The Q criterion gives the local balance between strain rate and vorticity magnitude [23]. This method is frequently used to investigate the vortices and is applicable to both 2-D and 3-D flows and is defined as

$$Q = \frac{1}{2}\Omega_{ij}\Omega_{ij} - S_{ij}S_{ij}$$ **Equation 4.2**

Where S_{ij} and Ω_{ij} are symmetric and anti-symmetric components of velocity gradient tensor and are defined as:

$$S_{ij} = \frac{1}{2}(\partial_j\langle\overline{u_i}\rangle + \partial_i\langle\overline{u_j}\rangle)$$ **Equation 4.3**

$$\Omega_{ij} = \frac{1}{2}(\partial_j\langle\overline{u_i}\rangle + \partial_i\langle\overline{u_j}\rangle)$$ **Equation 4.4**

Instantaneous flow-visualization using iso surfaces of Q for coarse and fine grid resolutions are shown in Figure 4.14 to Figure 4.17 respectively, at 6×10^4 $/s^2$ value. On comparing the coarse and fine grid resolutions following important points were withdrawn:

Both grids visualised showed cowl vortex travelling in spanwise direction from the centreline at hood/windshield intersection, contributes into side mirror wake via root of A-Pillar and side mirror structural joint.

Though the streamwise flow interacting with windshield area and later emerging in conical vortex behind A-Pillar can be seen in both the grids but the formation of a hairpin type vortex over the windshield was only seen using the fine grid. Hairpin vortex is formed when streamwise flow is lifted off from the surface through mutual induction of its counter-rotating legs forming a loop [47]. They carry air adjacent to the wall up through the legs and into the head and its growth continue until it leaves the shear layer which can be seen in Figure 4.17 where the hairpin vortex emerging in conical vortex behind A-Pillar was depicted at different flow intervals.

Though both grids showed the vortex formation behind the A-Pillar, the coarse grid; in comparison to fine grid; shows strong coherent structure at the upper location and vortex gets stronger and wider as we move further downstream of front side glass window as depicted in Figure 4.14 and Figure 4.16. The reason for wider coherent structure for coarse grid is because of the lower mesh resolution which leads to inability to capture the large scales.

The flow field at the reattachment line over front side glass window did not show any vortex formation for the coarse case; due to the lower resolution; but the fine case provided useful information. The flow-field at reattachment zone is fed partially through the root of the A-Pillar and partially due to the side mirror wake as depicted in Figure 4.16 Figure 4.17.

The conical type of vortex formation over front side glass window was captured by both grids however coarse grid visualised stronger and wider vortex formation when compared to fine grid.

Overall, the unsteadiness is clearly captured. However, the range of length scales captured is rather limited even at the finest grid resolution. This is due to the computational effort required to resolve the whole vehicle and relatively low order of accuracy scheme employed by Ansys Fluent 14.0. Such schemes are

not optimum for LES. The simulation can be clarified at best as Very Large Eddy Simulation (VLES) in the A-Pillar region.

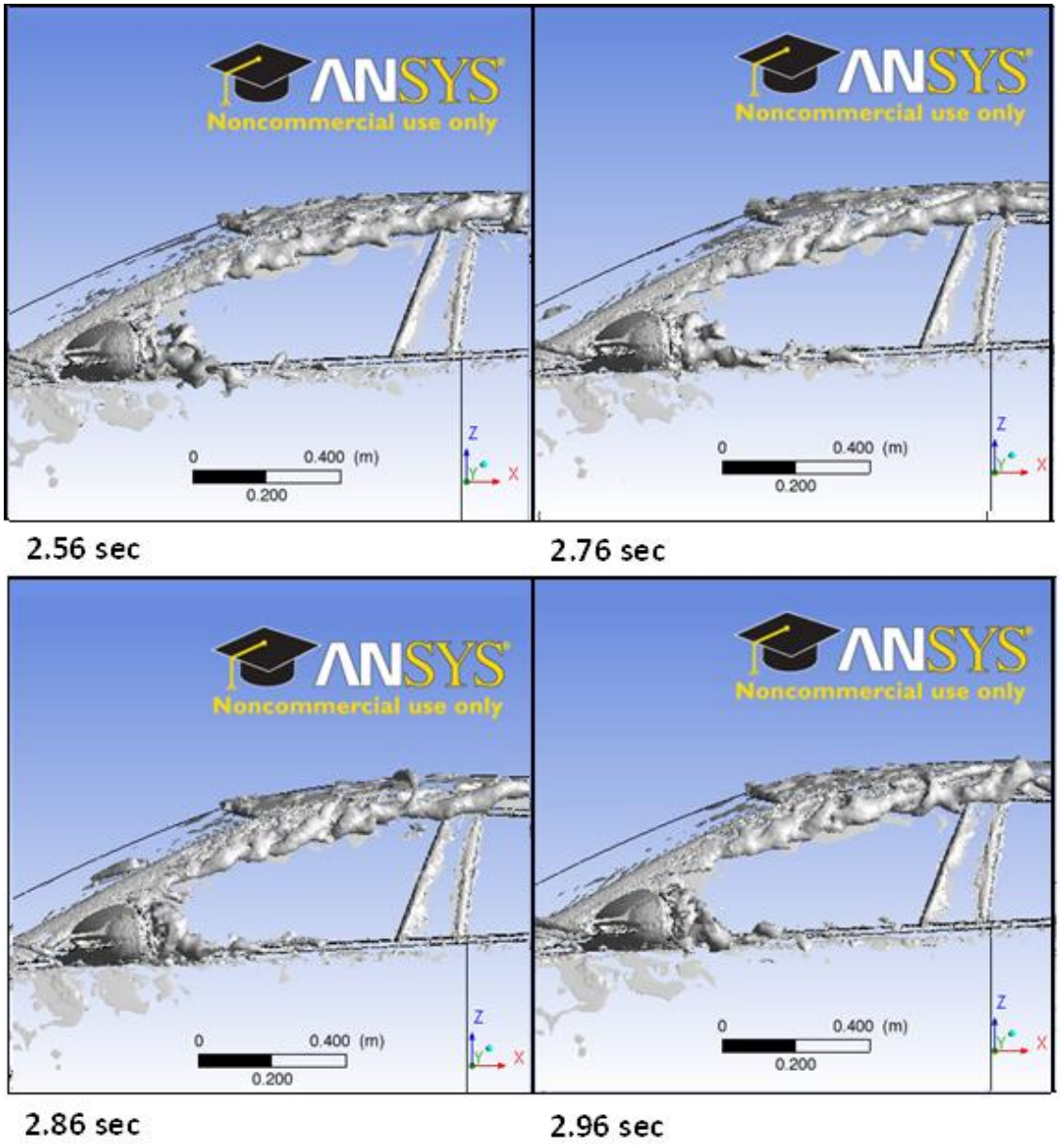

Figure 4.14 Q-Criterion (6× 10^4 /s^2) with different time steps using coarse mesh (side view)

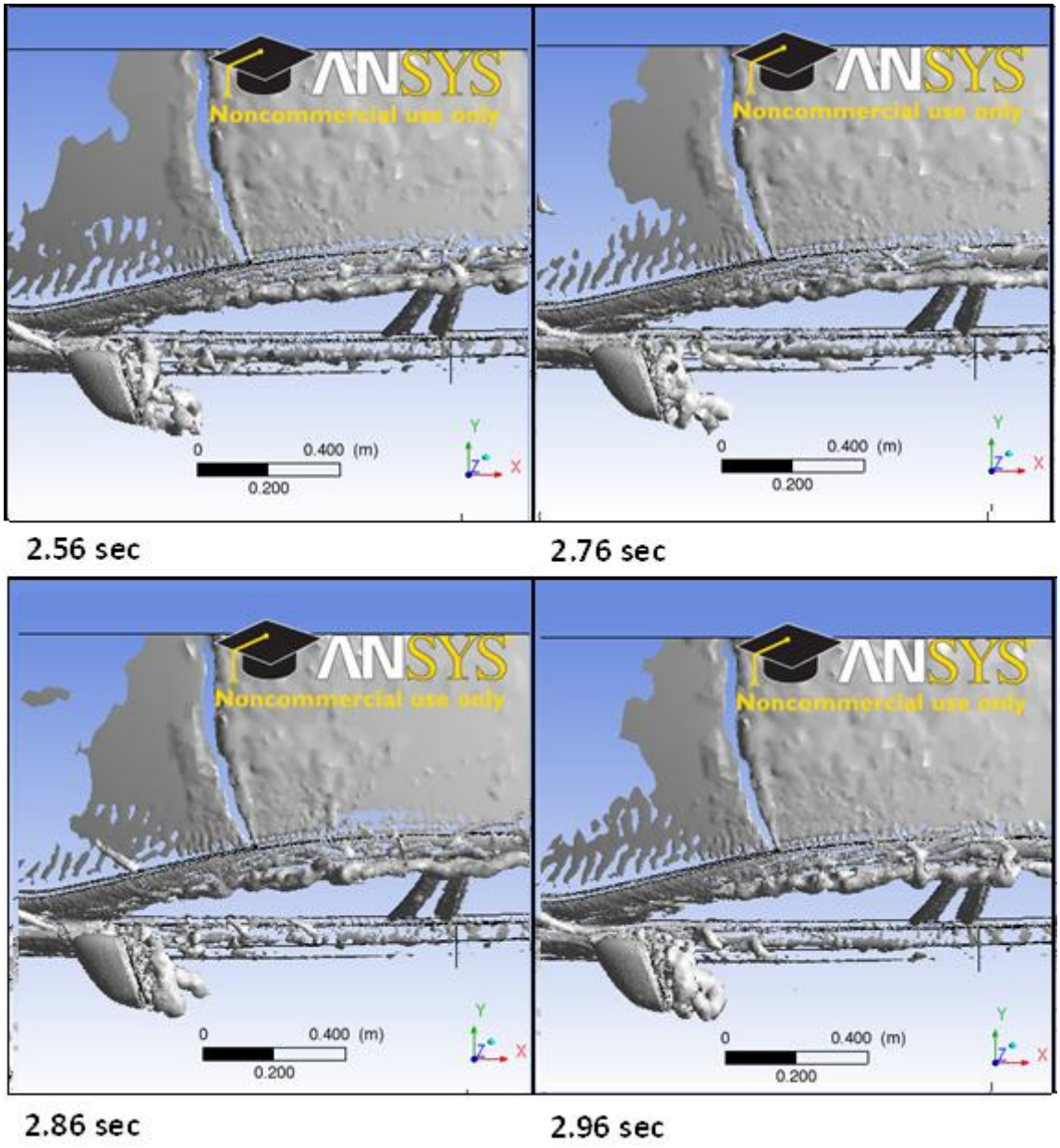

Figure 4.15 Q-Criterion (6×10^4 /s^2) with different time steps using coarse mesh (top view)

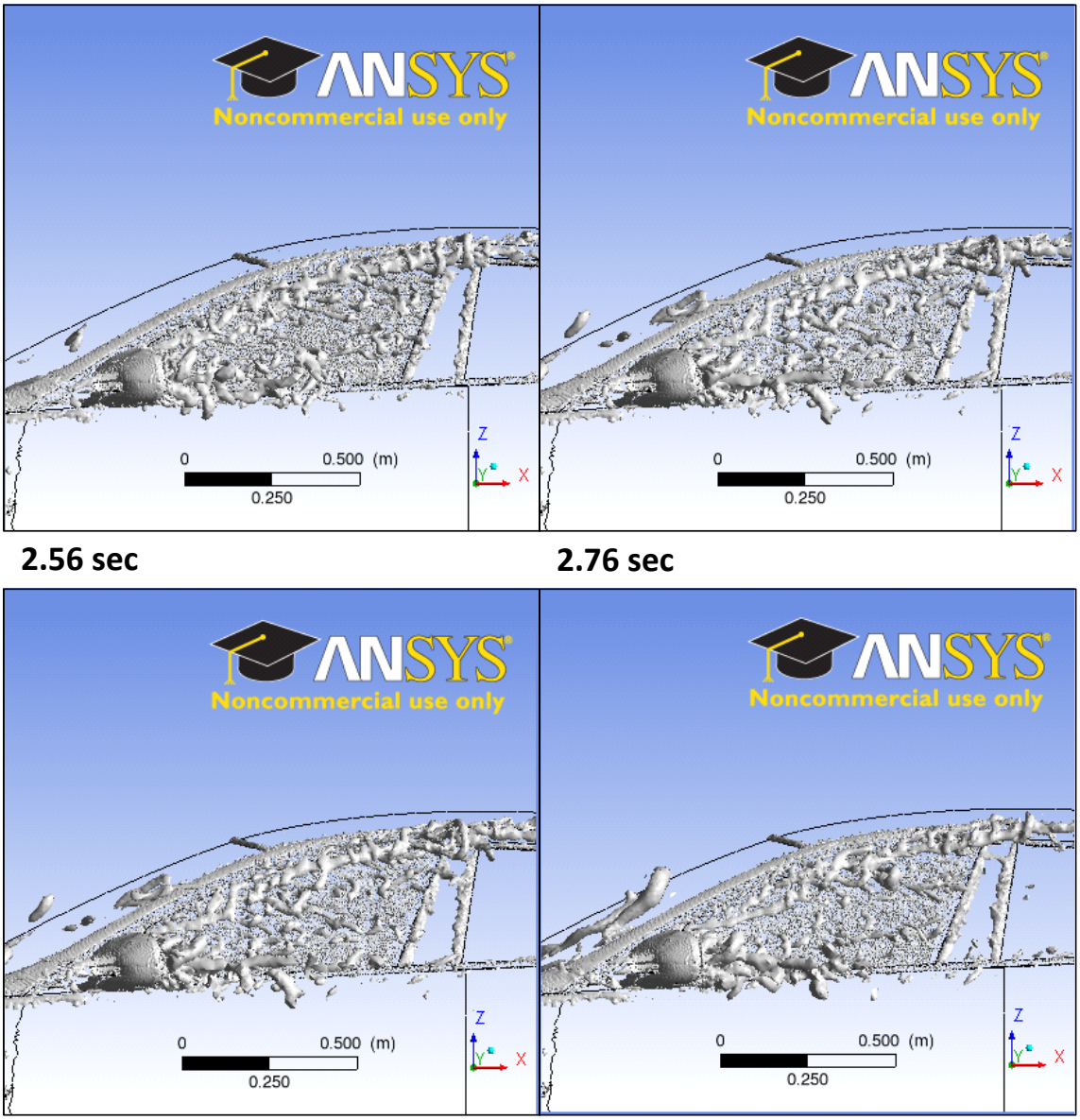

Figure 4.16 Q-Criterion (6× 10^4 /s2) with different time steps using fine mesh (side view)

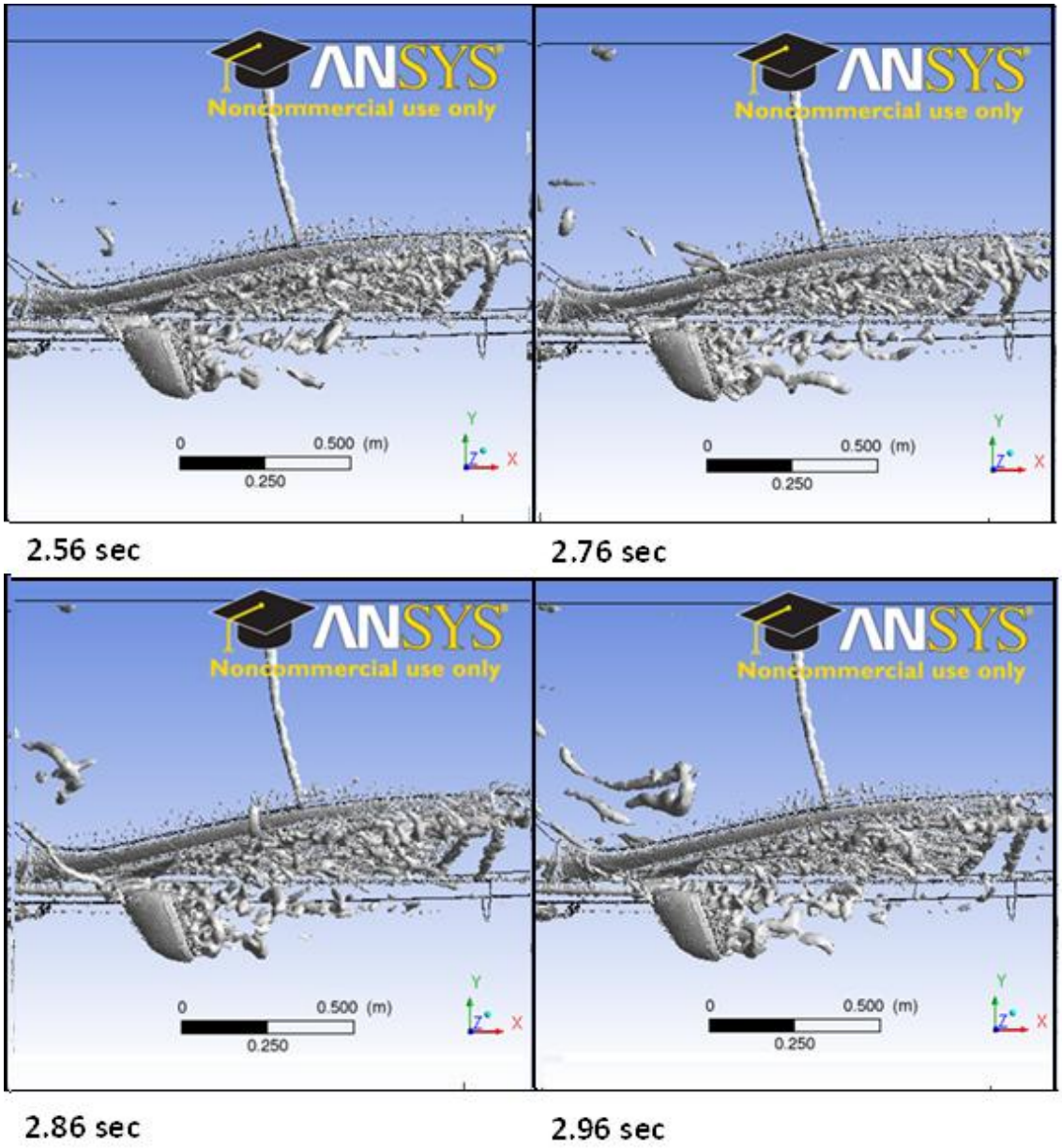

Figure 4.17 Q-Criterion (6× 104 /s2) with different time steps using fine mesh (top view)

4.3 Quantitative Analysis:

4.3.1 Statistical convergence:

The method selected for statistical convergence in current work is based on the personal conversation with Adrian Gaylard at Jaguar Land Rover. For statistical convergence, drag was monitored at every time step using 100 μs time step size until it reaches the statistical steady state. The method opted for statistical convergence was discussed and implemented Initial data set has been excluded because of unphysical statistics in the beginning which after few time steps settles down into physical realistic values about the mean. Although the convergence was achieved at nearly 2 sec flow-time but the drag was monitored for more time steps as bigger is the sample size more precisely the results can be predicted. In order to determine the start-up phase and valid data set selection, reverse averaging was established. Reverse averaging means calculating successive averages that progressively exclude data points from early in the time series, whilst always including the latest result. Usually there are three distinct features when plotting the reverse averages:

1. Start-up phase where unphysical results are generated and are normally excluded;
2. A Plateau where averaged values tend to stabilize; and
3. Settling phase where excluding valid data destabilizes the averaged data

The end of start-up phase considers the earliest drag average; starting of plateau, where minimum data varies about the mean value and the start-up phase should be excluded from the plot. From the beginning of the plateau forward averaging is plotted as show in all drag plots. The drag statistics for three grid resolutions including the reverse and forward drag plots is shown in Figure 4.18, Figure 4.19, and Figure 4.20.

Figure 4.21 to Figure 4.23 shows the reverse averaging and forward averaging plots for drag with three grid resolutions.

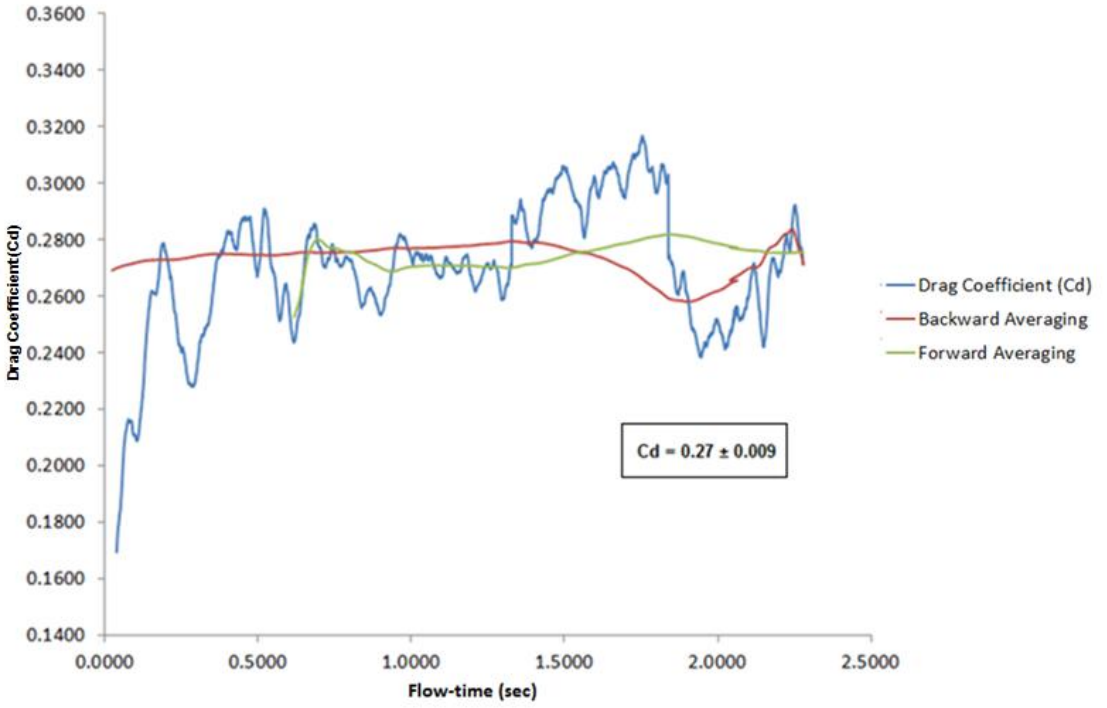

Figure 4.18 Drag plot for Coarse Grid

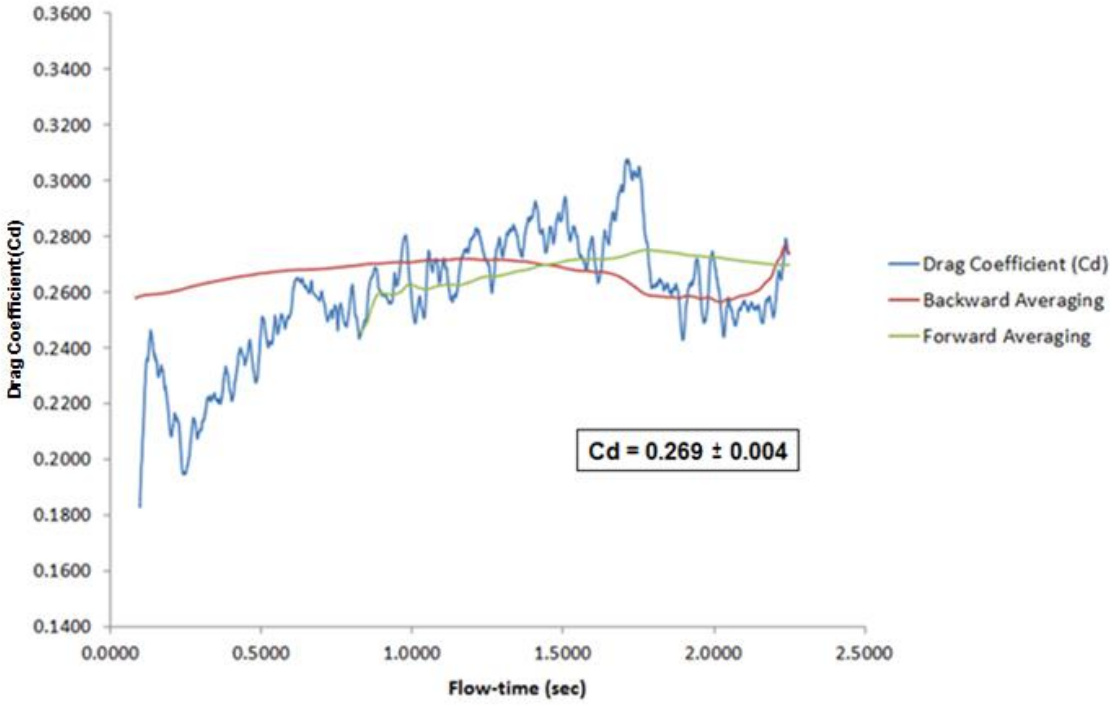

Figure 4.19 Drag plot for Medium Grid

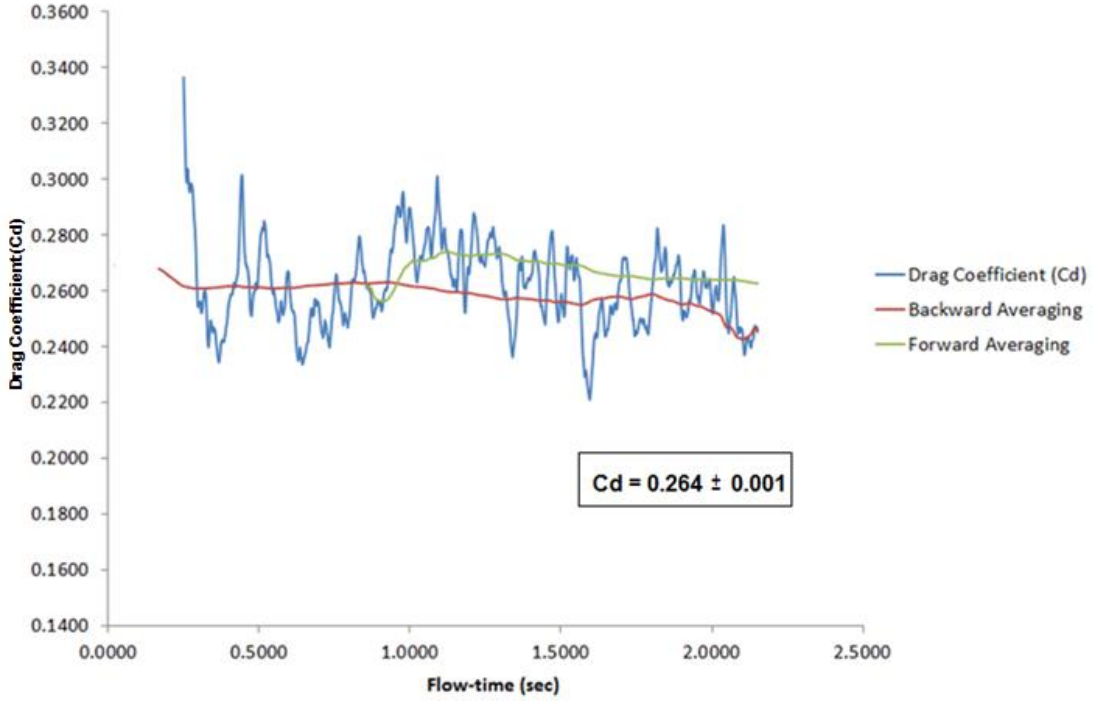

Figure 4.20 Drag plot for Fine Grid

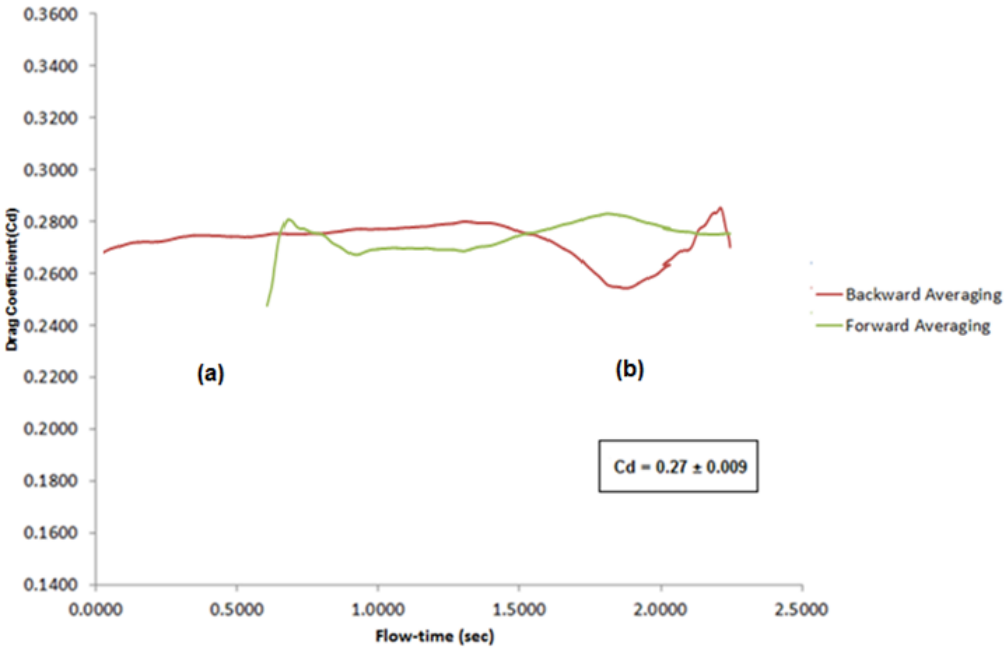

Figure 4.21 Drag coefficient for coarse grid with reverse averaging (a) showing plateau and stabilization phase (b) and forward averaging excluding the start-up phase

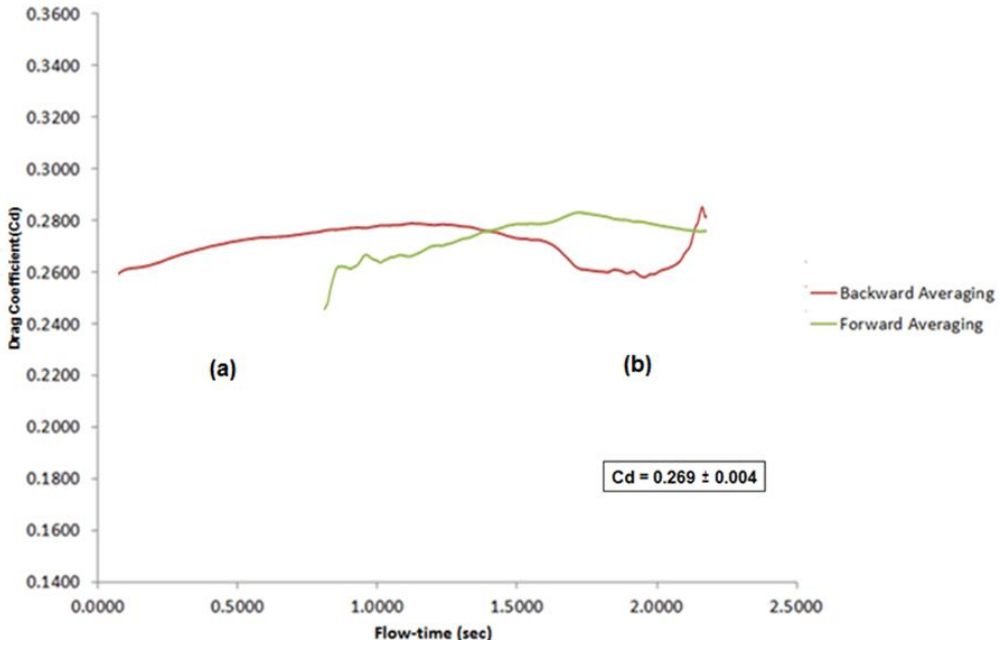

Figure 4.22 Drag coefficient for medium grid with reverse averaging (a) showing plateau and stabilization phase (b) and forward averaging excluding the start-up phase

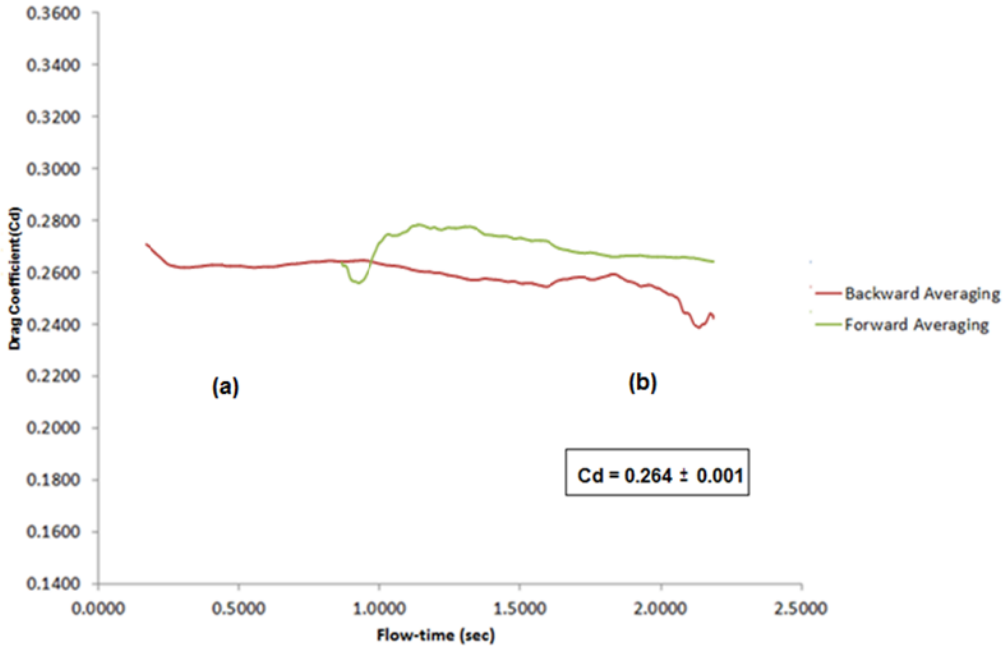

Figure 4.23 Drag coefficient for fine grid with reverse averaging (a) showing plateau and stabilization phase (b) and forward averaging excluding the start-up phase

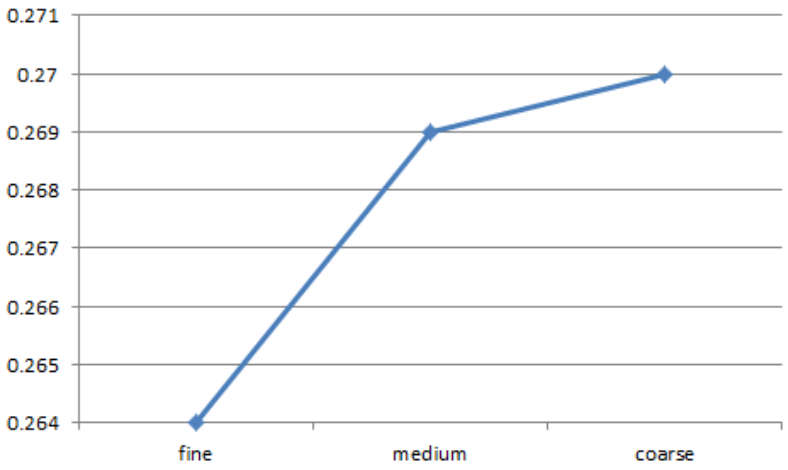

Figure 4.24 Drag Convergence with grid resolution

Using above stated method for checking statistical steady state, three probes; at top, middle and bottom position; were located over the front side glass surface to monitor the velocity fluctuations as shown in Figure 4.25

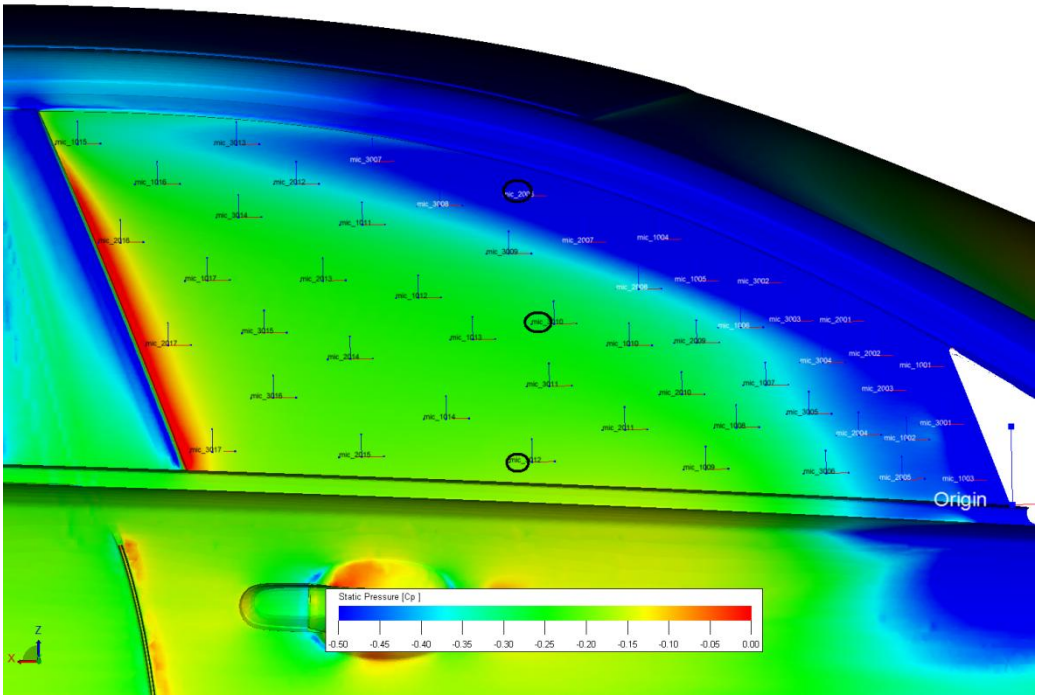

Figure 4.25 Probes located for monitoring statistical steady state

The start-up phase was not captured as monitoring the velocities at probes located only after 7 t_{car} which corresponds to approximately 0.9 sec flow-time. The plots are shown from Figure 4.26 to Figure 4.28. From the forward averaging in these plots we can see that the velocity magnitude stabilizes for all probes after 1.65 sec of flow-time. Moreover, this agrees with the drag plots for the fine case as well where the flow stabilizes approximately after 1.65 sec of flow-time as shown in Figure 4.20.

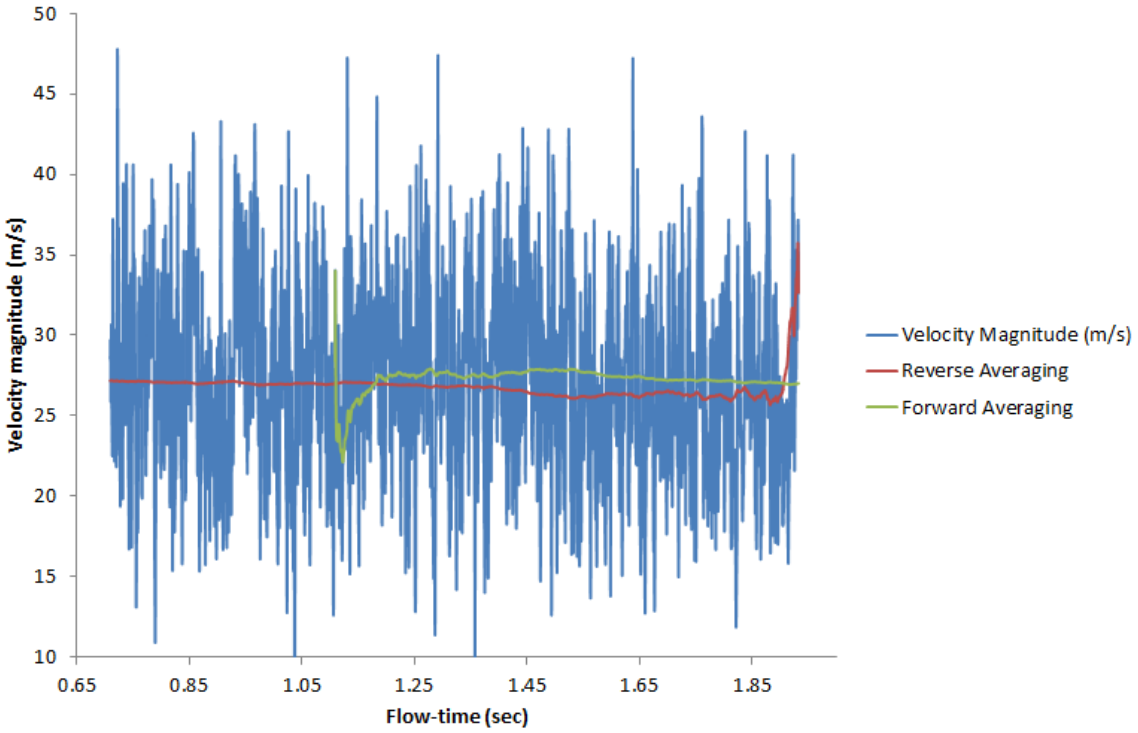

Figure 4.26 Velocity magnitude (m/s) monitored at top position of front side glass surface

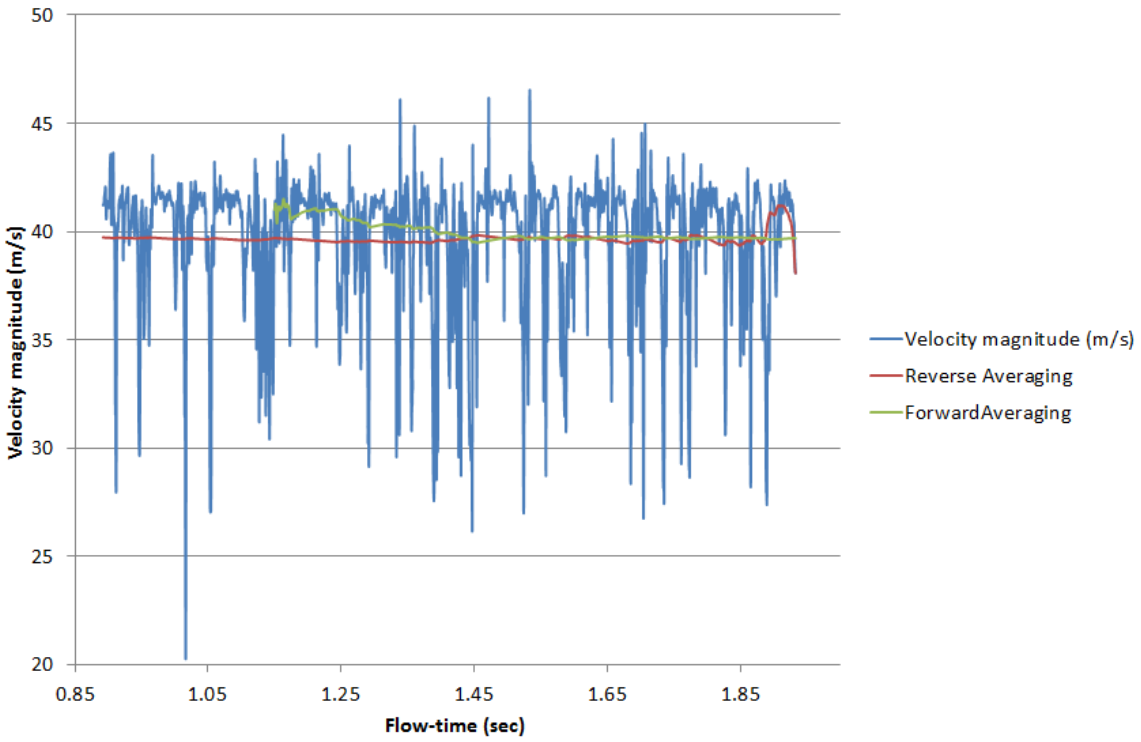

Figure 4.27 Velocity magnitude (m/s) monitored at middle position of front side glass surface

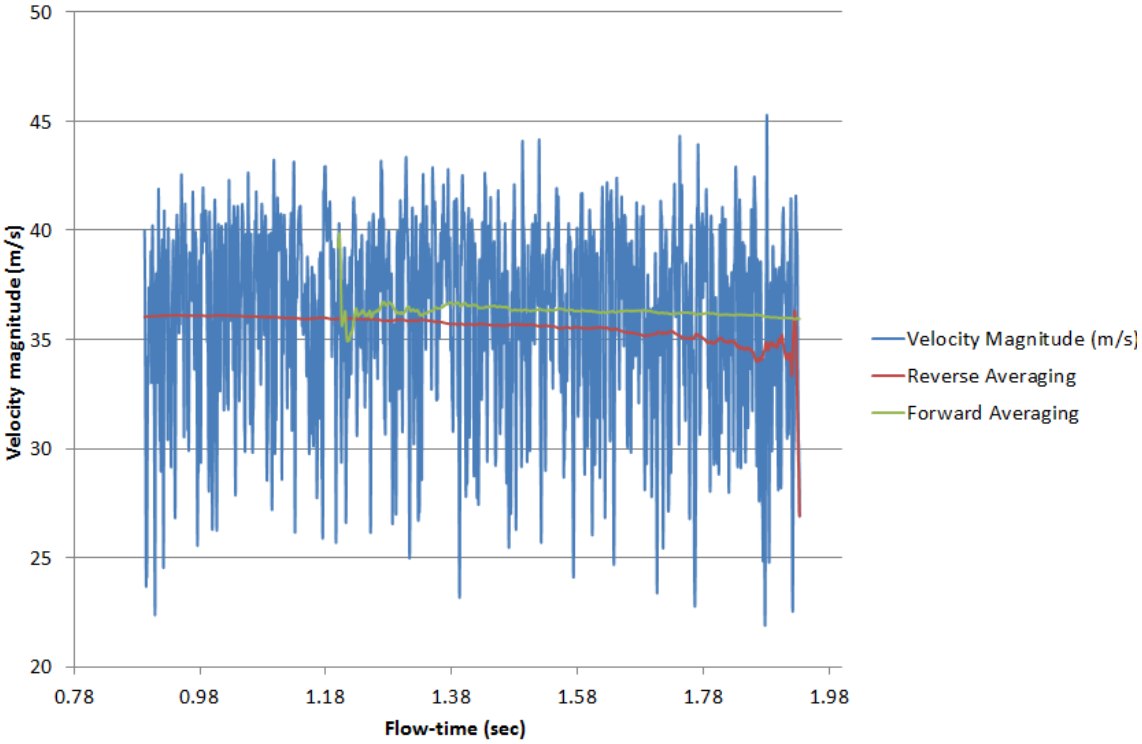

Figure 4.28 Velocity magnitude (m/s) monitored at bottom position of front side glass surface

In this section the averaged pressure (C_p) using three grid resolutions over the front side glass window were compared with results provided by JLR as shown in Figure 4.29.

But before we compare the results, the C_p was imported into MATLAB to analyse the recorded pressure statistically. This was done in order to confirm that whether after reaching statistical steady state there exist any variation for C_p. For this, only fine mesh was considered.

From Figure 4.29 it is very clear that the shape of the A-Pillar wake generated by computational analysis is comparable to results provided by JLR (using ExaPowerFLOW), except the coarse mesh where A-Pillar vortex entrainment was over-predicted and looks smeared with low pressure (C_p) regions at upstream of the front side glass window since the grid is too coarse to capture the smaller scale. The cheater re-attachment line where separation occurs due to side mirror structural joint was seen in all grid resolutions. The side mirror wake region was captured in case of fine and medium grid only. Also, the

reattachment zone for all grid resolutions over-predicted the negative pressure in comparison to JLR results. More details of flow behaviour were visualised using the surface streamlines over front side glass window as shown in Figure 4.6. As there are no small scales captured, the A-Pillar vortex is stronger as it does not transfer energy to smaller vortices.

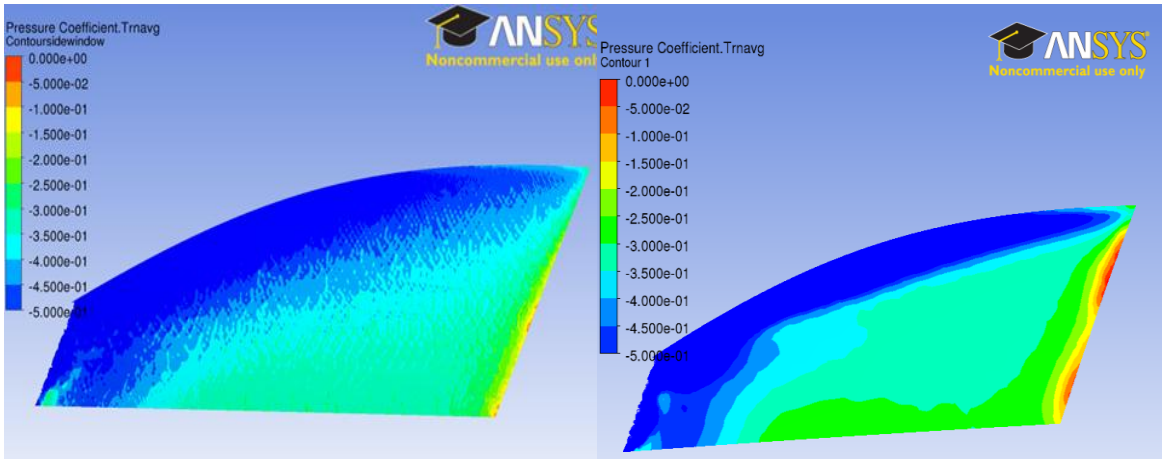

Coarse case Medium case

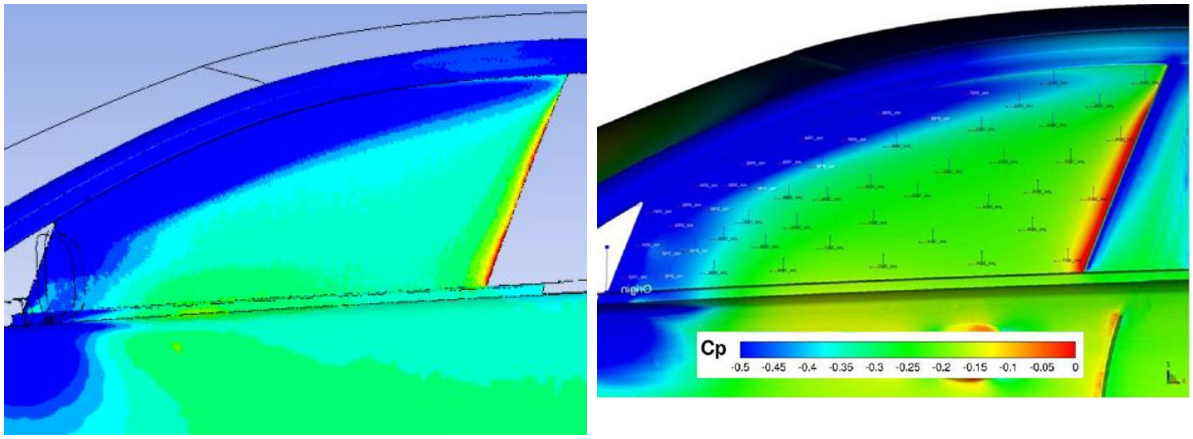

Fine Case JLR (using PowerFLOW)

Figure 4.29 Comparison of averaged pressure distribution over front side glass window using coarse mesh (top left); medium mesh (top right); fine mesh (bottom left); and JLR (using Exa PowerFLOW)) with pressure (C_p) ranging from ($-0.5 \leq C_p \leq 0$)

In order to quantify the deviations, probes were located on the front side glass window and compared with JLR pressure data. The location of probes is shown in Figure 4.30. The pressure data comparison can be seen from Figure 4.31 to Figure 4.38. It is noteworthy that the probes located over front side window had a maximum error; in locating on its surface; of approximately ±0.01 m

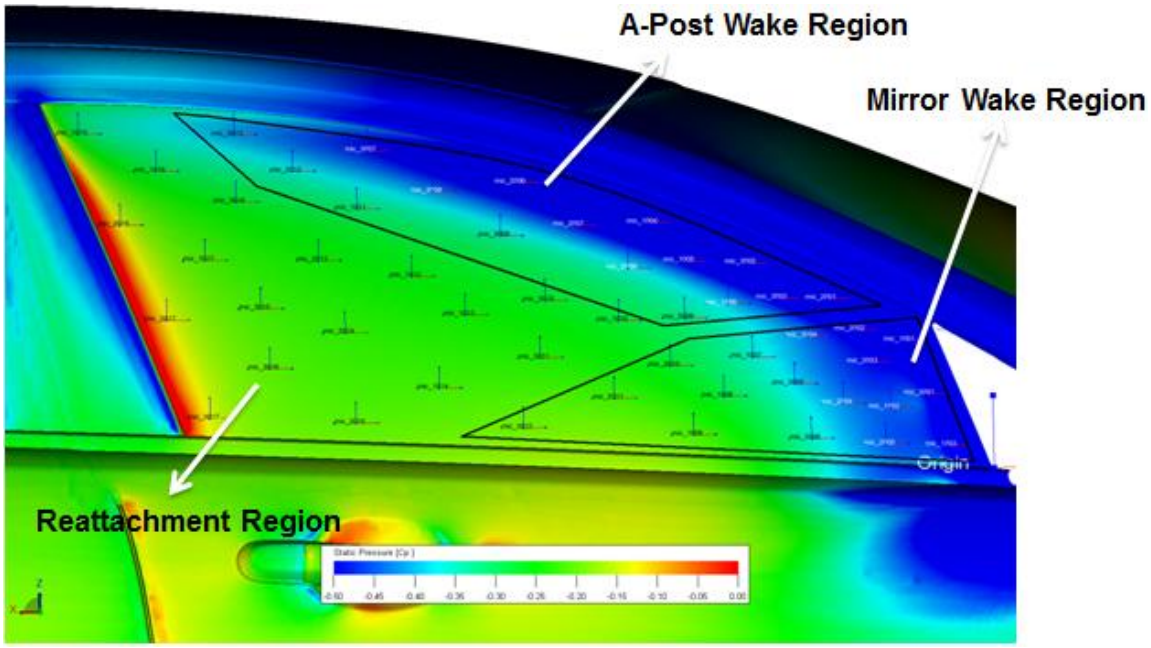

Figure 4.30 Probes location on front side window

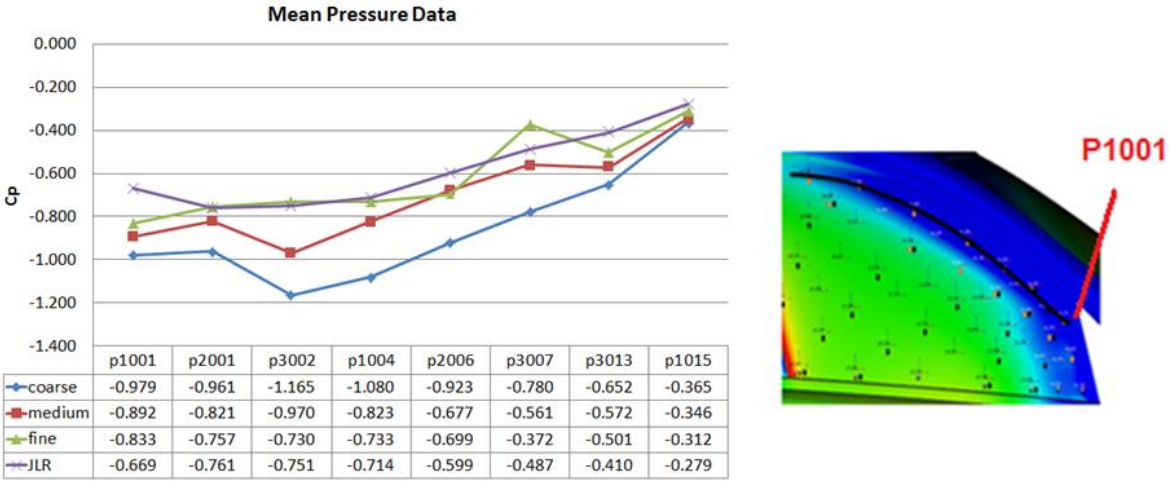

	p1001	p2001	p3002	p1004	p2006	p3007	p3013	p1015
coarse	-0.979	-0.961	-1.165	-1.080	-0.923	-0.780	-0.652	-0.365
medium	-0.892	-0.821	-0.970	-0.823	-0.677	-0.561	-0.572	-0.346
fine	-0.833	-0.757	-0.730	-0.733	-0.699	-0.372	-0.501	-0.312
JLR	-0.669	-0.761	-0.751	-0.714	-0.599	-0.487	-0.410	-0.279

Figure 4.31 Quantitative analysis of probes located over front side glass window (1)

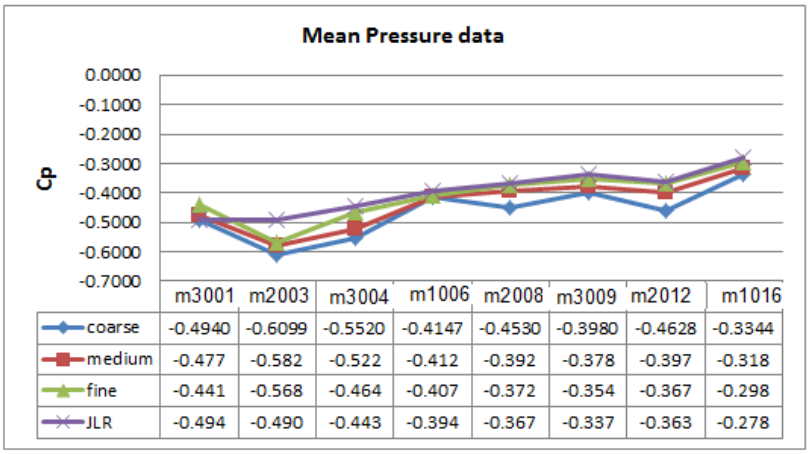

	m3001	m2003	m3004	m1006	m2008	m3009	m2012	m1016
coarse	-0.4940	-0.6099	-0.5520	-0.4147	-0.4530	-0.3980	-0.4628	-0.3344
medium	-0.477	-0.582	-0.522	-0.412	-0.392	-0.378	-0.397	-0.318
fine	-0.441	-0.568	-0.464	-0.407	-0.372	-0.354	-0.367	-0.298
JLR	-0.494	-0.490	-0.443	-0.394	-0.367	-0.337	-0.363	-0.278

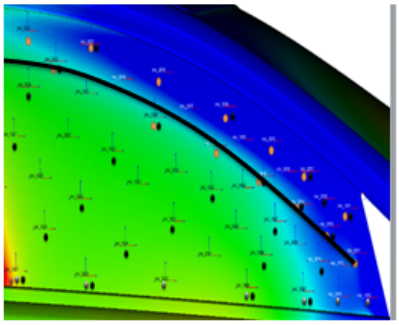

Figure 4.32 Quantitative analysis of probes located over front side glass window (2)

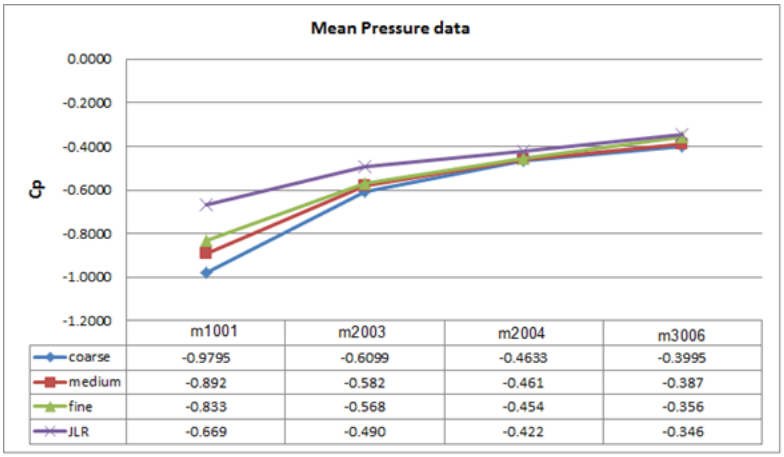

	m1001	m2003	m2004	m3006
coarse	-0.9795	-0.6099	-0.4633	-0.3995
medium	-0.892	-0.582	-0.461	-0.387
fine	-0.833	-0.568	-0.454	-0.356
JLR	-0.669	-0.490	-0.422	-0.346

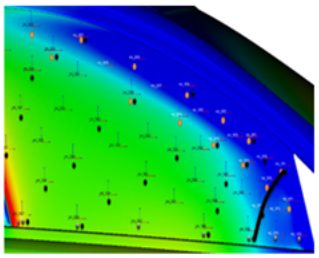

Figure 4.33 Quantitative analysis of probes located over front side glass window (3)

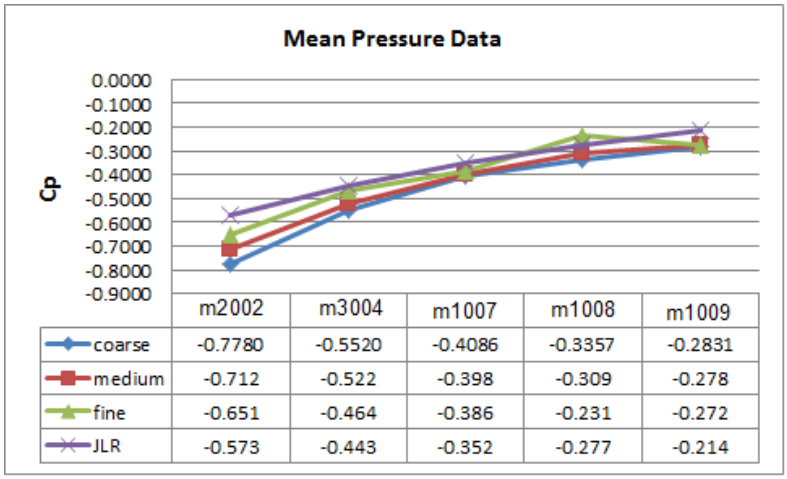

	m2002	m3004	m1007	m1008	m1009
coarse	-0.7780	-0.5520	-0.4086	-0.3357	-0.2831
medium	-0.712	-0.522	-0.398	-0.309	-0.278
fine	-0.651	-0.464	-0.386	-0.231	-0.272
JLR	-0.573	-0.443	-0.352	-0.277	-0.214

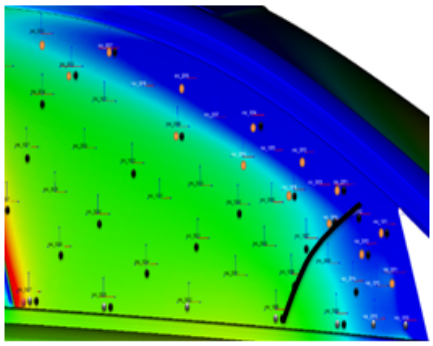

Figure 4.34 Quantitative analysis of probes located over front side glass window (4)

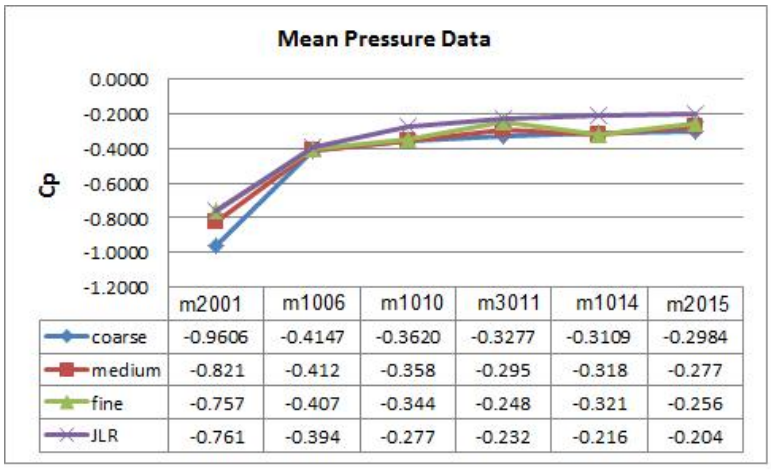

	m2001	m1006	m1010	m3011	m1014	m2015
coarse	-0.9606	-0.4147	-0.3620	-0.3277	-0.3109	-0.2984
medium	-0.821	-0.412	-0.358	-0.295	-0.318	-0.277
fine	-0.757	-0.407	-0.344	-0.248	-0.321	-0.256
JLR	-0.761	-0.394	-0.277	-0.232	-0.216	-0.204

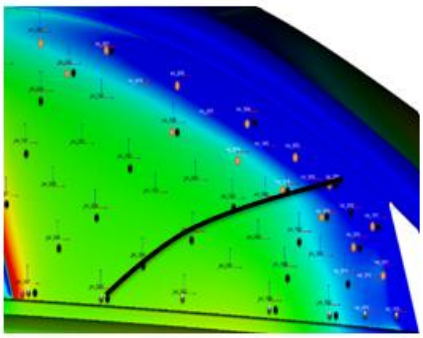

Figure 4.35 Quantitative analysis of probes located over front side glass window (5)

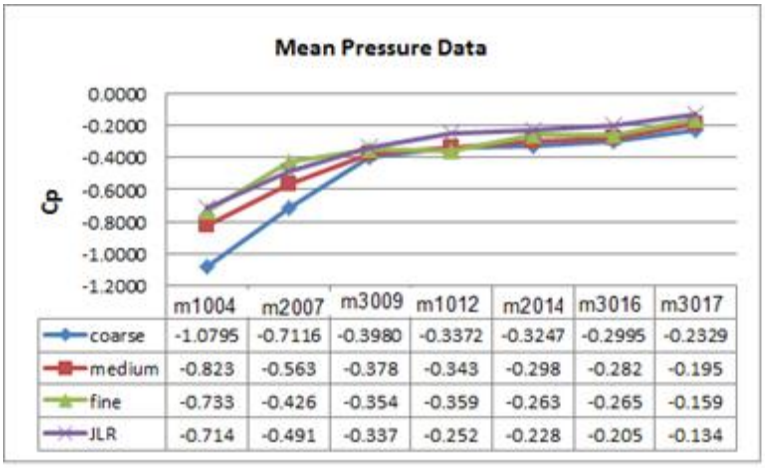

	m1004	m2007	m3009	m1012	m2014	m3016	m3017
coarse	-1.0795	-0.7116	-0.3980	-0.3372	-0.3247	-0.2995	-0.2329
medium	-0.823	-0.563	-0.378	-0.343	-0.298	-0.282	-0.195
fine	-0.733	-0.426	-0.354	-0.359	-0.263	-0.265	-0.159
JLR	-0.714	-0.491	-0.337	-0.252	-0.228	-0.205	-0.134

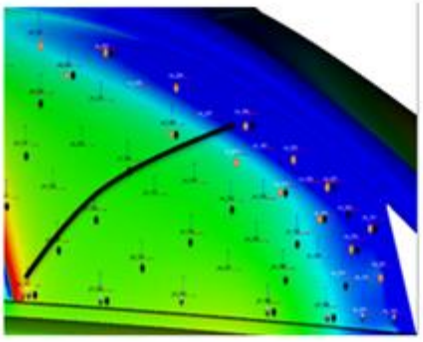

Figure 4.36 Quantitative analysis of probes located over front side glass window (6)

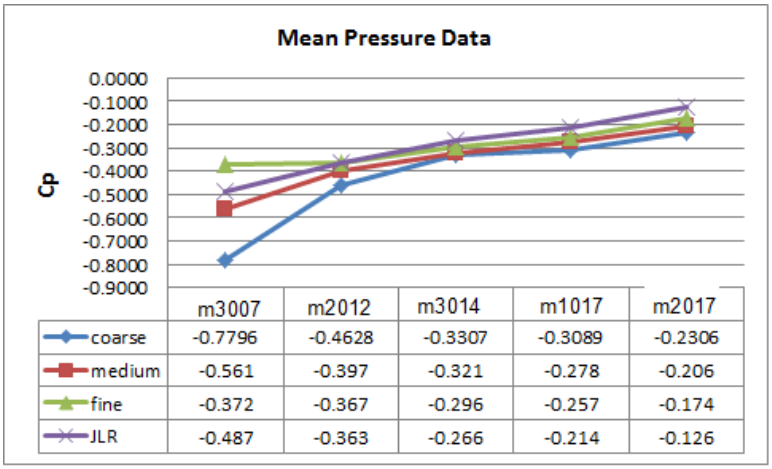

	m3007	m2012	m3014	m1017	m2017
coarse	-0.7796	-0.4628	-0.3307	-0.3089	-0.2306
medium	-0.561	-0.397	-0.321	-0.278	-0.206
fine	-0.372	-0.367	-0.296	-0.257	-0.174
JLR	-0.487	-0.363	-0.266	-0.214	-0.126

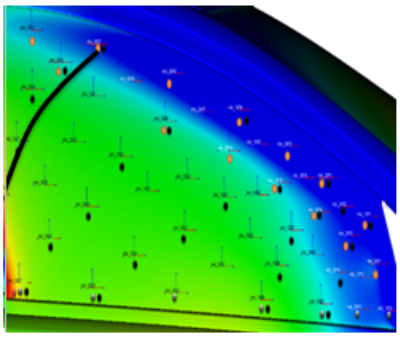

Figure 4.37 Quantitative analysis of probes located over front side glass window (7)

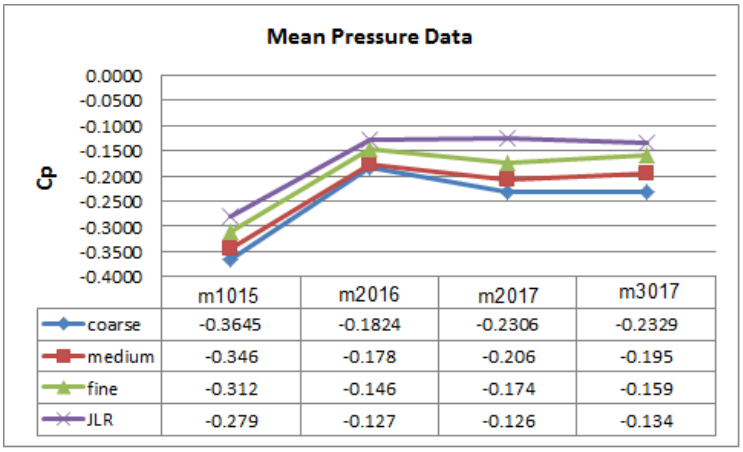

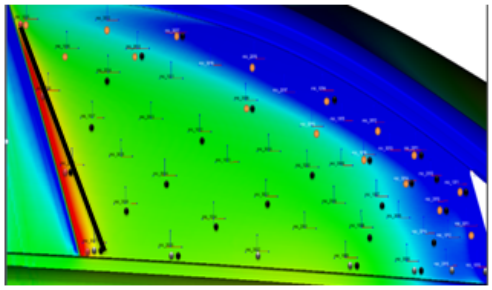

Figure 4.38 Quantitative analysis of probes located over front side glass window (7)

The A-Post wake region over-predicted the negative pressure data throughout the A-Pillar wake region (as shown in Figure 4.31 and Figure 4.32) with average difference of $-0.17 \leq C_p \leq -0.01$ for fine case. The worst location that highly over-predicted negative C_p was P1001 located at behind side mirror structural joint and cheater re-attachment area. The flow in this area gives a small separation due to high velocity flow squeezing through the side mirror structural joint and collates with cheater re-attachment area. The wake of side mirror was well predicted by the probes located in side mirror wake region, it can be seen that probes located in this region well predicted the wake of side mirror. Mirror wake region showed comparable results with JLR for all grid resolutions However; the reattachment zone shows fairly a good agreement with average difference of $-0.1 \leq C_p \leq -0.017$.

5 Sound Pressure Levels

The external wall pressure fluctuations at front side glass window were examined by locating probes over the front side glass surface. However, due to the restrictions using Ansys Fluent 14.0 (non-commercial use), only ten probes were located and are shown in Figure 5.1. sound pressure levels were generated by post-processing importing the pressure data recorded at every time step into the MATLAB using the Fast Fourier Transform. But before we discuss the results, post processing of pressure data is discussed briefly.

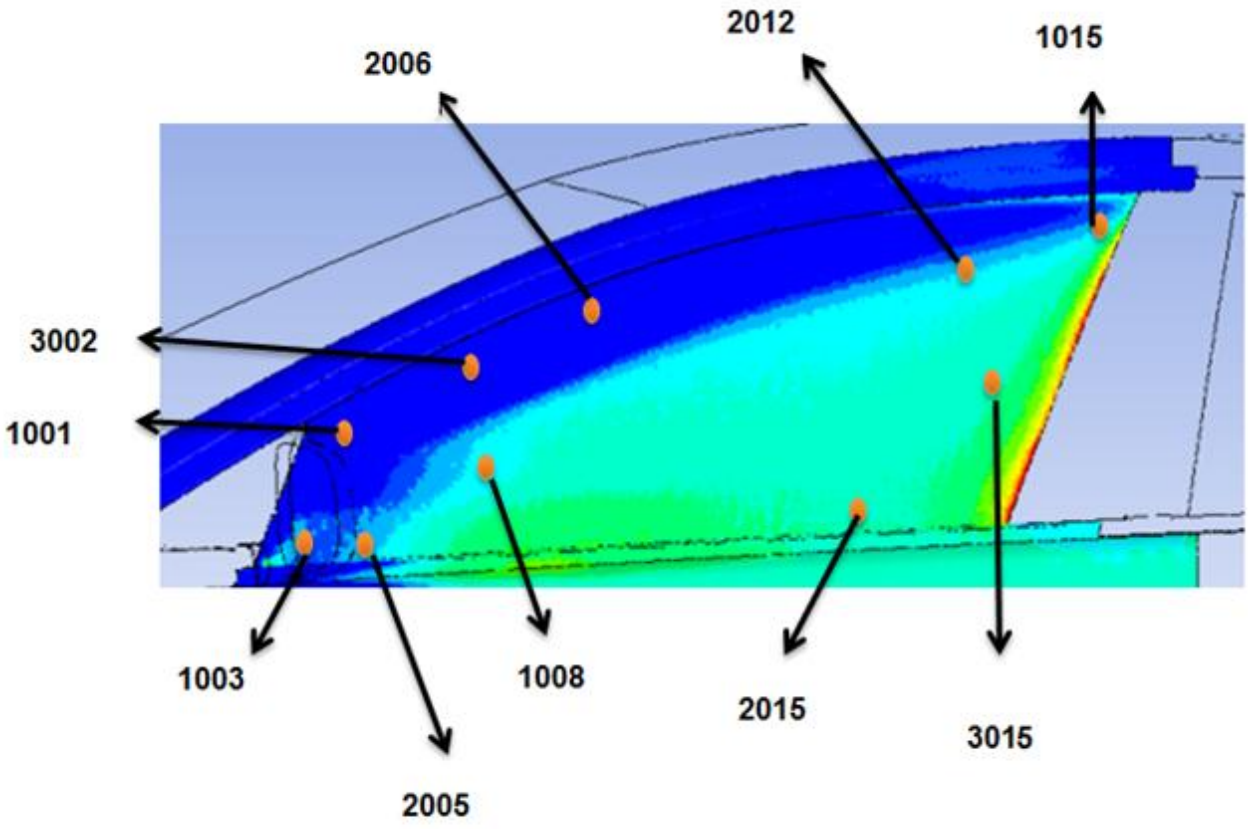

Figure 5.1 Probes location over front side glass window

5.1 Post processing surface pressure (static):

The results obtained from simulations at specified probe location consists of pressure (static) generated at every time step (Pressure v/s time). To obtain better statistical properties, the data generated was averaged for 10 tcar. This data was imported into the MATLAB for generating the Sound pressure levels

with respect to frequency. To obtain information as a function of frequency rather than time, Fast Fourier Transform was applied which decomposes the signal as a sum of sine and cosine waves, expressed below:

$$f(t) = a_o + \sum_{n=1}^{\infty} (a_n \sin(2\pi nt) + (b_n \cos(2\pi nt)\,) \quad \textbf{(5-1)}$$

Where $f(t)$ is the signal in the time domain, a_n and b_n are the unknown coefficient and n is the frequency of the wave. The unknown coefficients a_n and b_n can be calculated by applying FFT function in MATLAB that gives a complex number c_n in terms of real and imaginary part, as written in equation (5-2 and (5-3)

$$a_n = \frac{1}{2N} imag(c_n) \quad 0 < n < \frac{N}{2} \quad \textbf{(5-2)}$$

$$b_n = \frac{1}{2N} real(c_n) \quad 0 < n < \frac{N}{2} \quad \textbf{(5-3)}$$

where N represents the number of samples. However, the real part and imaginary parts represents cosine and sine series respectively cannot be directly used to generate the power spectrum therefore the absolute value of c_n should be considered. By squaring the absolute value of c_n, the power spectrum can be extracted.

Figure 5.2 shows the plot of pressure v/s time recorded by simulations in Ansys Fluent 14.0. Likewise, the pressure v/s time data was extracted from other nine probes located at front side glass surface. The sampling frequency satisfied the Nyquist Sampling theorem which suggests that the minimum frequency at which the data had to be sampled should be at least twice the maximum signal frequency.

By taking the absolute of results obtained using FFT results and then squaring them gives the Power or Amplitude which can be later converted into Sound Pressure Levels using equation

$$SPL = 20\ log\ \left(\frac{Power}{4 \times 10^{-10}}\right) \quad \textbf{(5-4)}$$

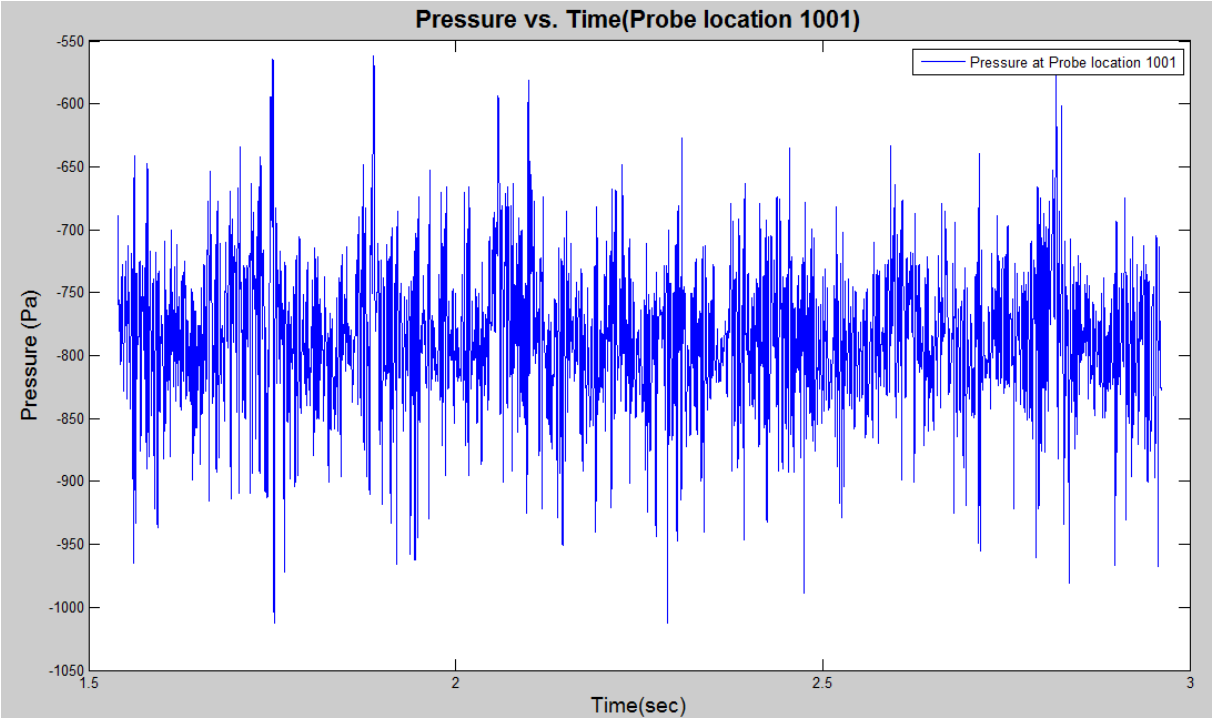

Figure 5.2 Pressure v/s time signal extracted at probe location 1001 over front side glass window

5.2 Analysis of Sound Pressure Levels

Figure 5.3 to Figure 5.5 shows the SPL for the selected probe locations have been plotted. This section will be sub-divided into three sections according to the region; namely A-Post wake zone, side mirror wake zone, and reattachment zone over the front side glass window as shown in Figure 4.30. However, only one probe location from each zone is presented here and rest are shown in Appendix

Table 5.1 Probes location over front side window with respect to zones

Zone	Number of Probes	Probes location
A-Post Wake	4	1015, 2006, 3002 and 2012
Side mirror Wake	4	1001, 1003, 1008 and 2005
Re-attachment area	2	2015 and 3012

5.2.1 A-Post Wake Zone

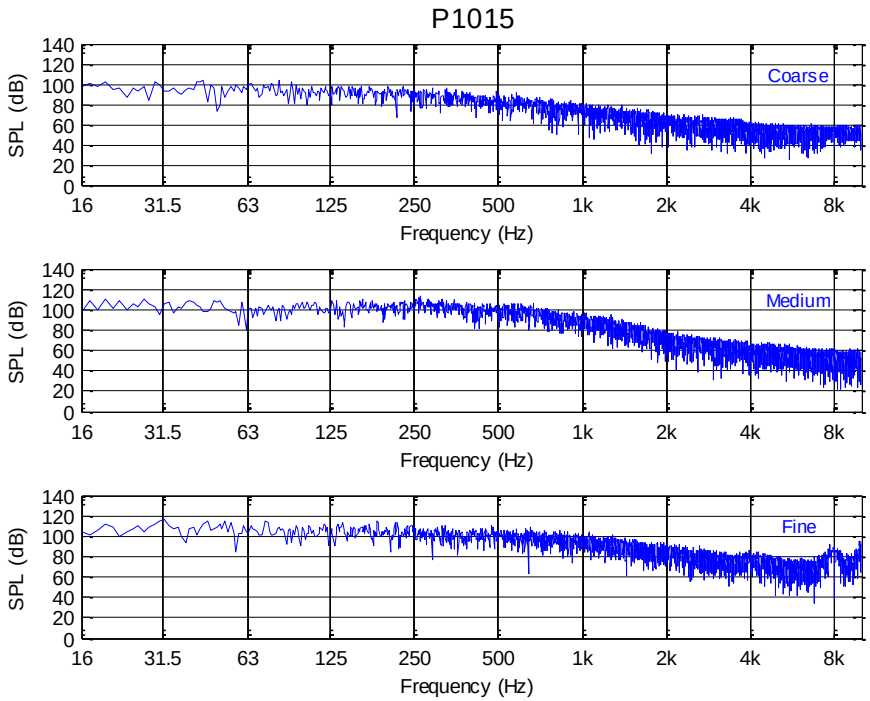

Figure 5.3 SPL (1/3rd Octave) (dB) V/s Frequency (Hz) at probe location 1015

5.2.2 Side Mirror Wake Zone

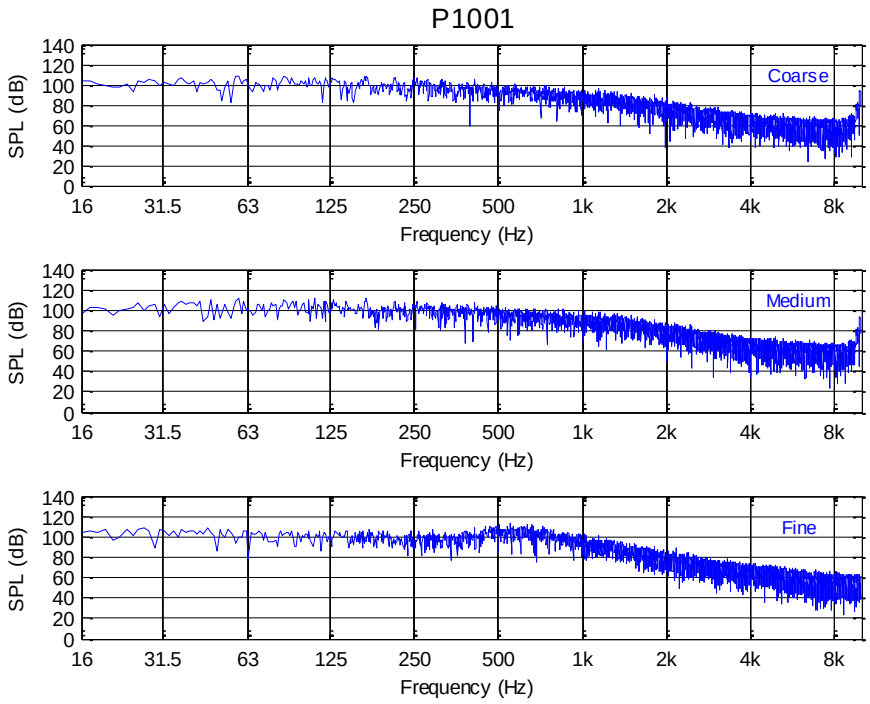

Figure 5.4 SPL (1/3rd Octave) (dB) V/s Frequency (Hz) at probe location 1001

5.2.3 Re-attachment zone

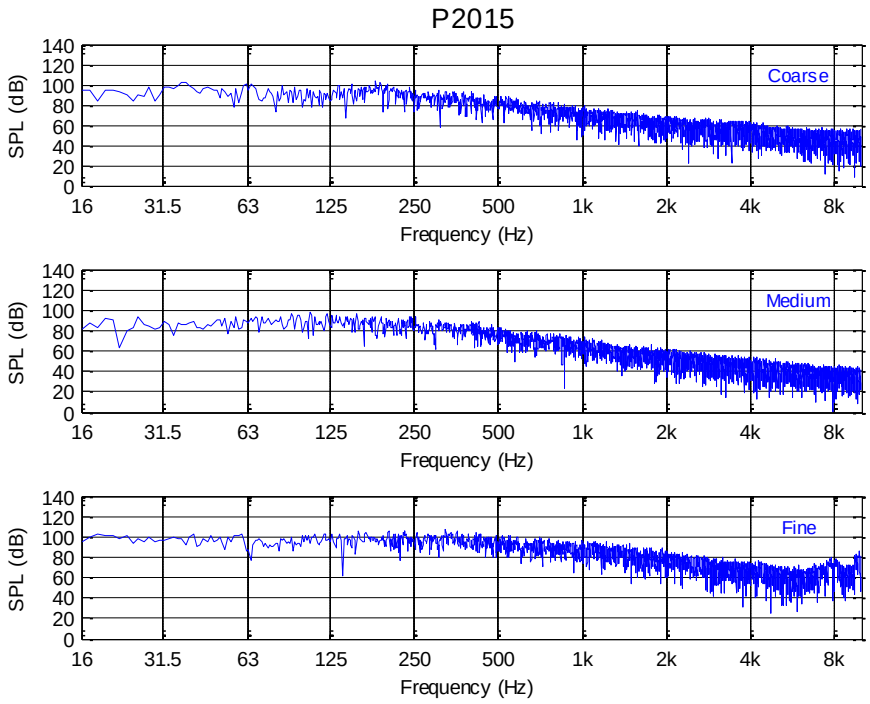

Figure 5.5 SPL (1/3rd Octave) (dB) V/s Frequency (Hz) at probe location 2015

Collectively, the results obtained within the frequency up to 250 Hz for three grid resolution used in this study showed variation of SPL by maximum 0 – 15 dB (except P2006) when compared to each other. However, the declining trend of SPL for higher frequencies from 250 Hz to 5 KHz showed varying data by maximum 25 dB. Nevertheless, on the basis of mesh cut-off the three grids revealed that fine mesh was able to resolve frequencies up to 1KHz where coarse and medium mesh were resolved up to 250 Hz and 600 Hz respectively. Subsequently, the fine mesh case is selected to compare with aero-acoustic wind tunnel results provided by JLR.

5.2.4 Comparison based on Sound Pressure Levels:

The sound pressure levels provided by JLR were extracted from Aero-acoustic Wind Tunnel (AWT) testing in Koln. The surface microphones typically, GRAS

type 40PS with 10 mm diameter were mounted over front side glass window. The data was recorded for 15 sec [11].

It is worth noting that the discrepancies in comparing the current work with AWT results are obvious because of the two reasons:

- The current work includes surface pressure data recorded for only 1 sec (10tcar) where in AWT recorded for 15 seconds and is computationally very expensive. Hence, less averaging was obtained as compare to AWT
- Another distinguishing point of concern is the probe diameter that is just a point (flush mounted) in present work and in the AWT a 10 mm probe diameter was used.

From plots shown in Figure 5.3 Figure 5.4 and Figure 5.5, the difference between three grid resolutions is very clear. The numerical simulations for the coarse grid were able to resolve frequencies up to 250 Hz only whereas medium and fine grid resolved frequencies up to 1 KHz. The finest grid was able to provide better results as compared to the coarse and medium grid. All grids provided comparable results especially at low frequencies and the average difference of coarse and medium grid

The plots in Figure 5.6 to Figure 5.15 shows the comparison between the CFD and AWT is shown.

Note: Only fine grid is used for comparison with AWT results.

5.2.4.1 A-Post region:

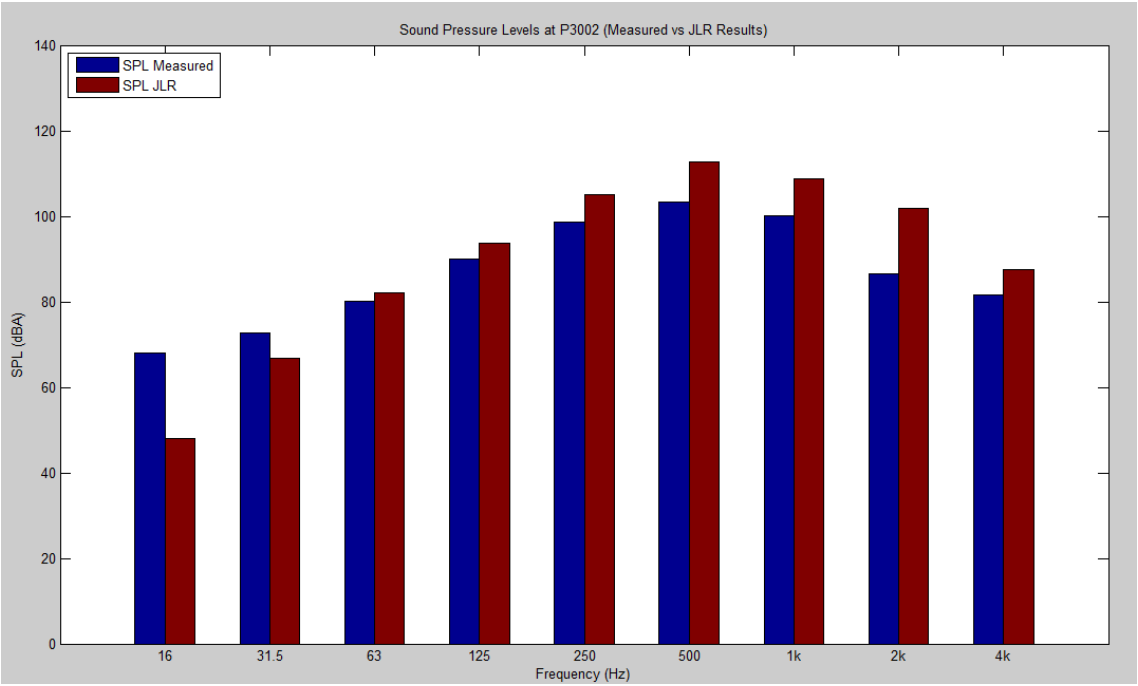

Figure 5.6 SPL comparison of CFD v/s AWT at probe location P3002

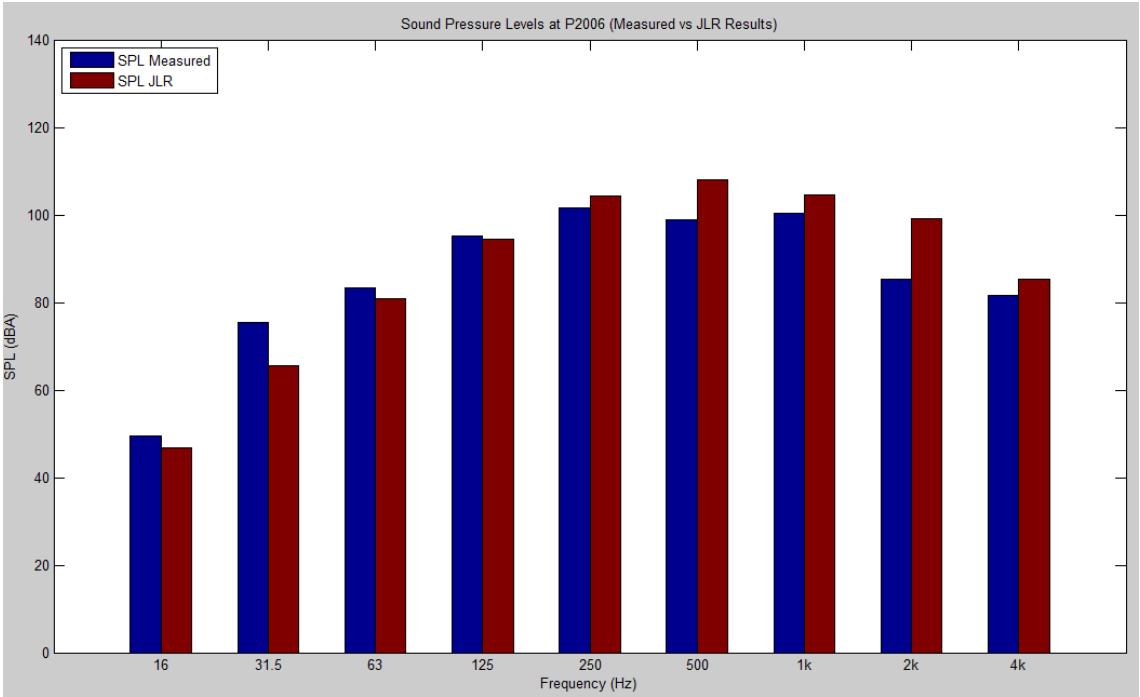

Figure 5.7 SPL comparison of CFD v/s AWT at probe location P2006

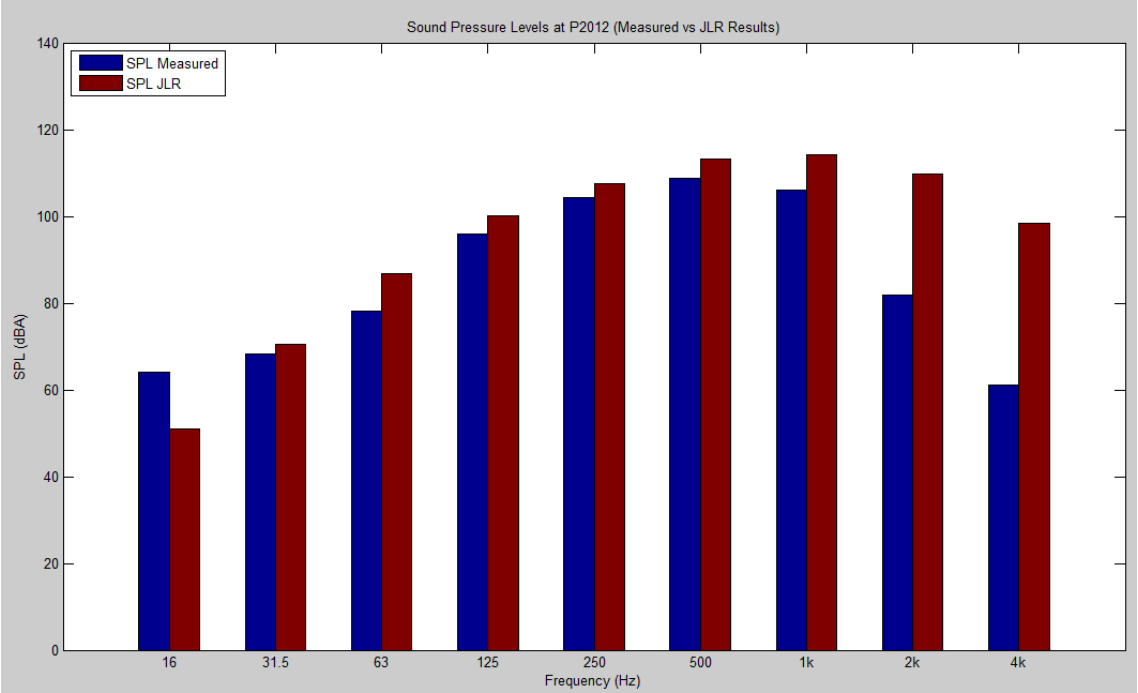

Figure 5.8 SPL comparison of CFD v/s AWT at probe location P2012

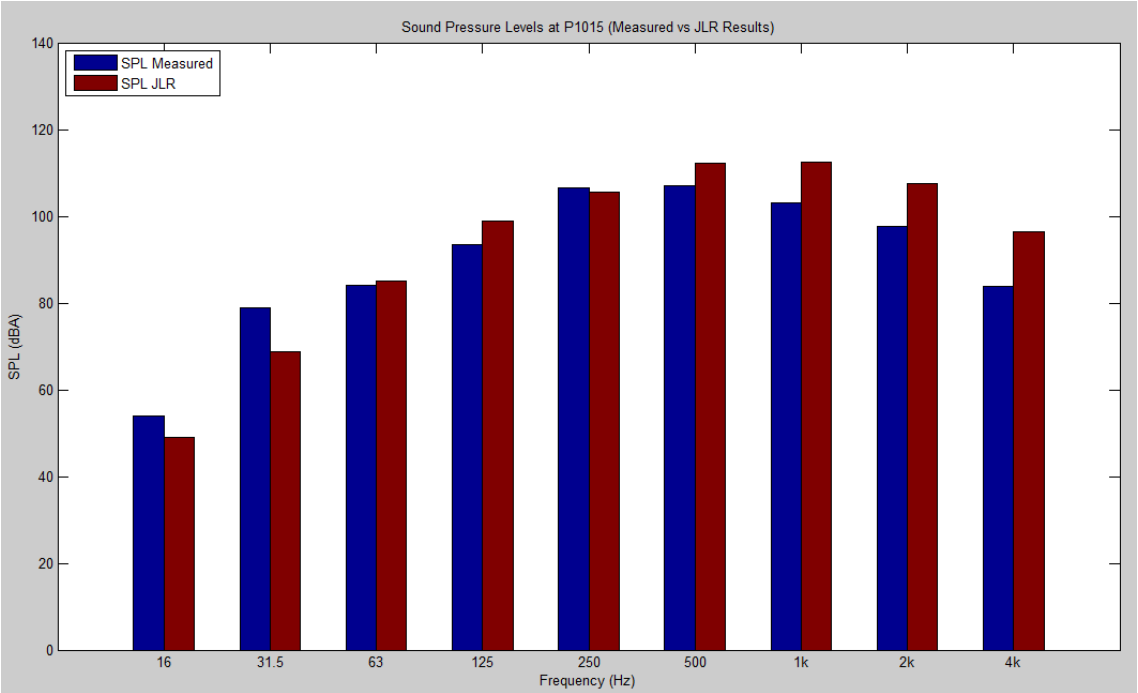

Figure 5.9 SPL comparison of CFD v/s AWT at probe location P1015

Figure 5.6 to Figure 5.9 shows the SPL extracted in A-Post wake region. The first figures represents closest to the origin (close to side mirror structural

joint).and last figure farthest. From these figures we can see that the correlation between the AWT and CFD is generally comparable for low frequencies up to 250 Hz however at higher frequencies ranging from 250 Hz to 4 KHz the correlation is less good as seen in the case of probe location P2012 which is located at A-Pillar vortex entrainment. The reason to this can be over-prediction of the size of separating A-pillar vortex at this location. Other probe locations (shown in Appendix) under-predicted the SPL and the trend of deviation at particular frequency for all grids showed similarity. For an instance consider frequency 1 KHz. The comparison for four probes at 1 KHz show approximately the same level of difference of maximum 20 dBA illustrating that the grid was not able to resolve higher frequencies especially above 1 KHz. This is consistent with the observation that the large scales are too energetic and the small scales are not captured with current numerical methods. Given the log scale, this is significantly over-predicting the lower frequency's SPL and over-predicting the higher frequency's SPL.

5.2.4.2 Side Mirror Wake Region:

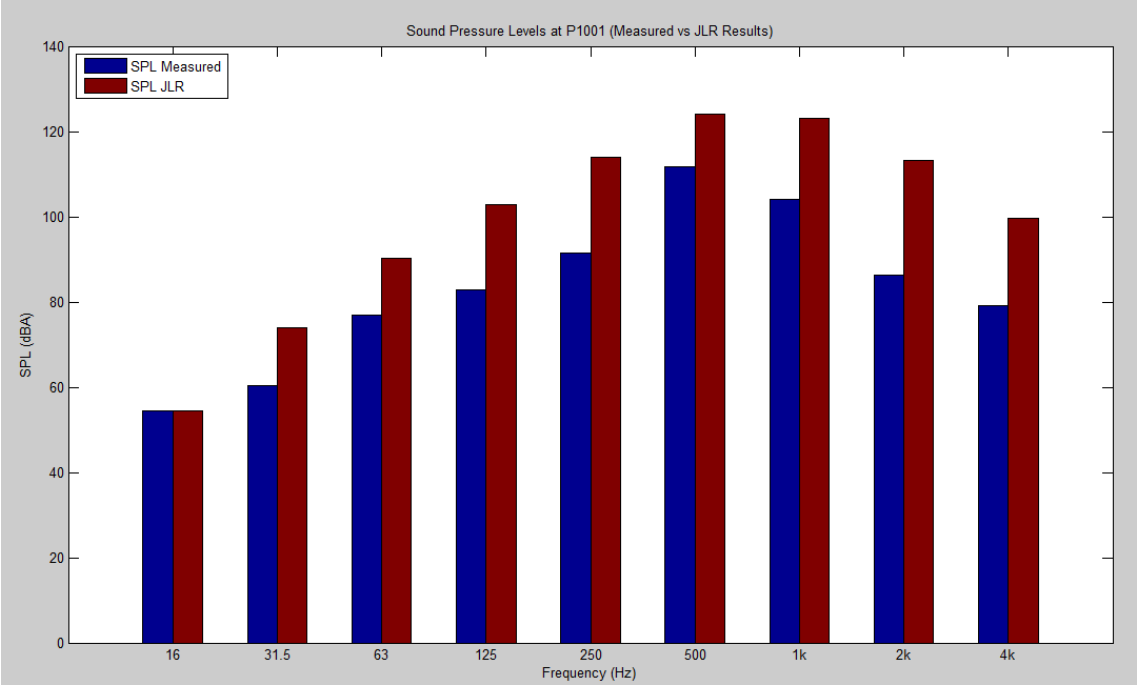

Figure 5.10 SPL comparison of CFD v/s AWT at probe location P1001

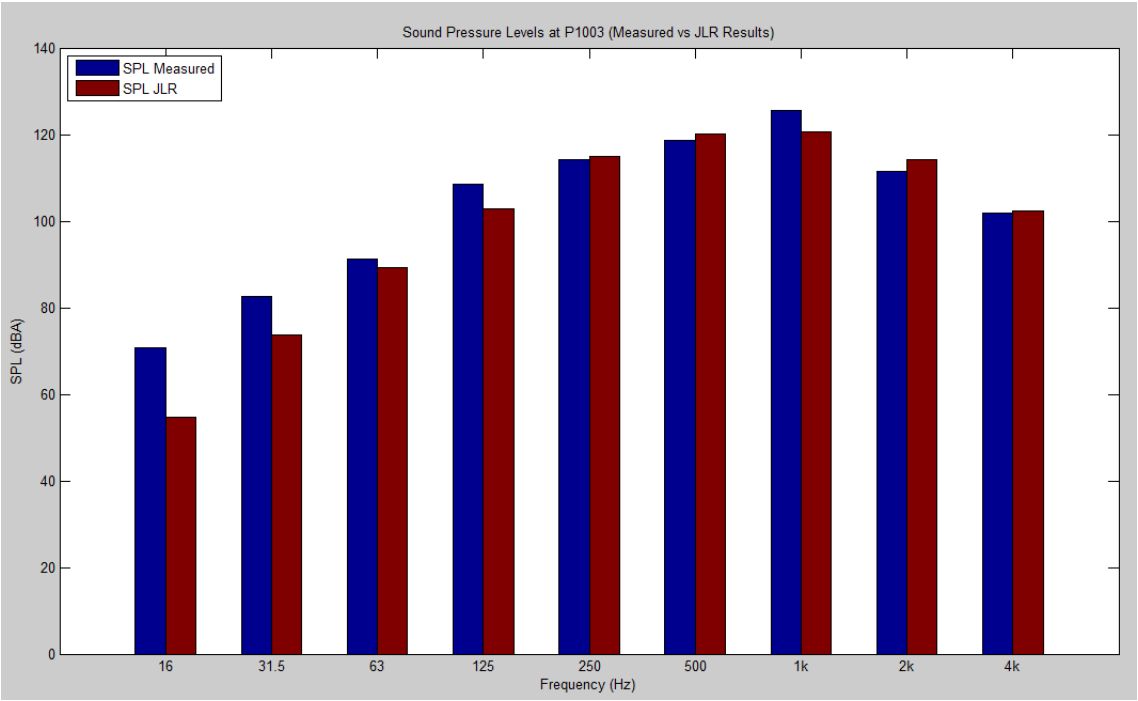

Figure 5.11 SPL comparison of CFD v/s AWT at probe location P1003

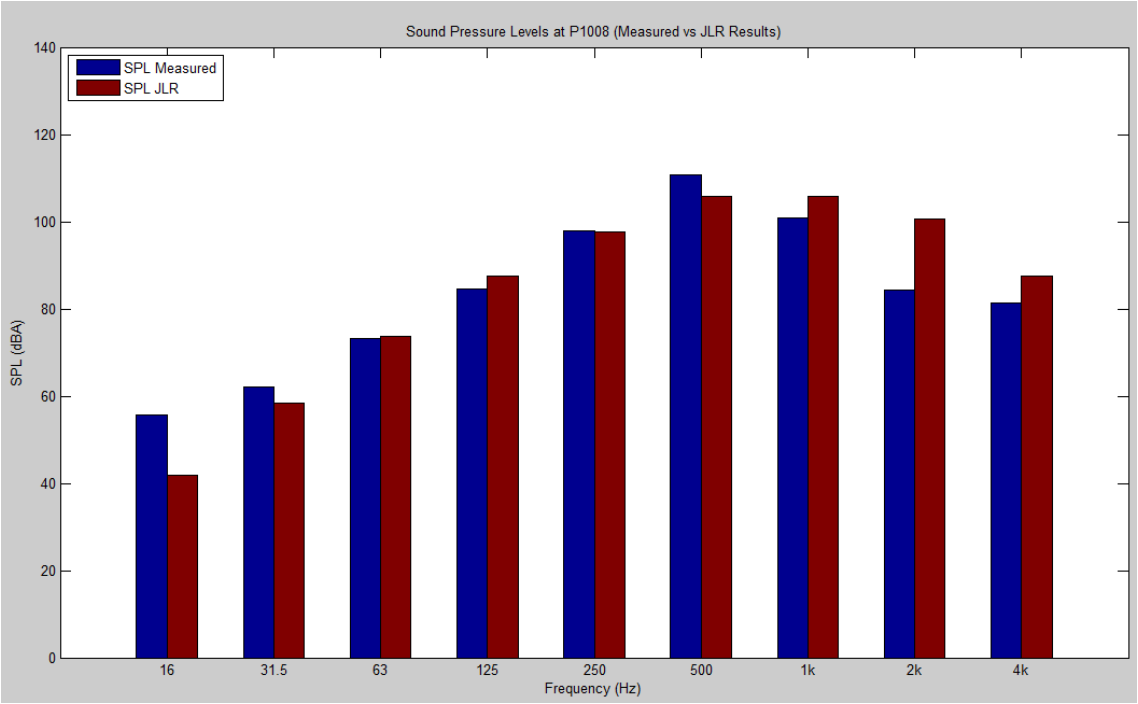

Figure 5.12 SPL comparison of CFD v/s AWT at probe location P1008

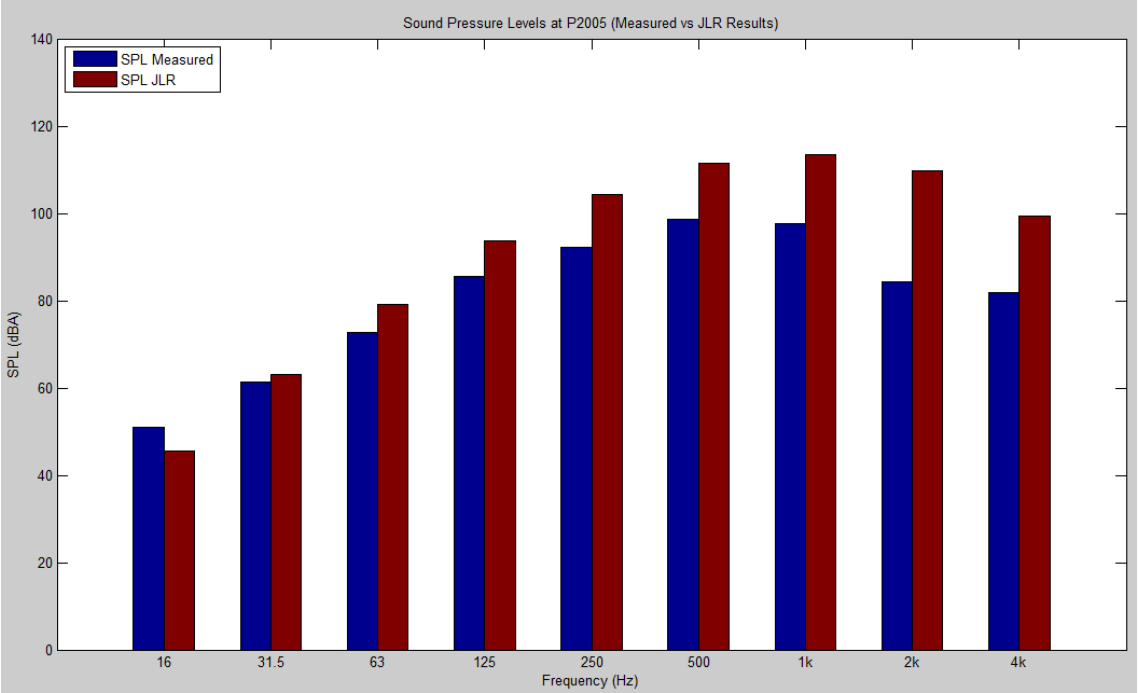

Figure 5.13 SPL comparison of CFD v/s AWT at probe location P2005

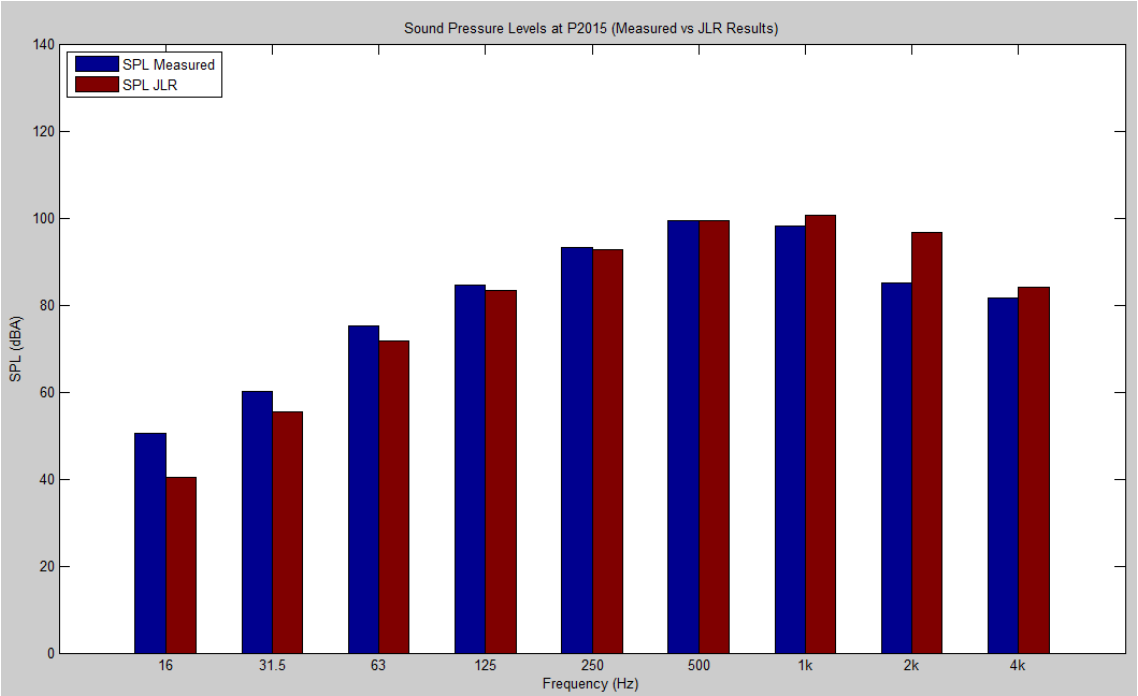

Figure 5.14 SPL comparison of CFD v/s AWT at probe location P2015

In the side mirror wake zone, the general trend of SPL at lower frequencies (≤ 250 Hz) showed good results except P1001 probe location that under-predicted the SPL even below the range of 250 Hz with a difference of

approximately – 20 dBA. The location of this probe is behind the top edge of the side mirror structural joint. Moreover, the correlation of this probe with AWT shows the greater deviations occurring at higher frequencies of maximum 25 dBA. P1001 probe location lies behind cheater reattachment line where the oncoming flow from the root of A-Pillar and side mirror wake merges and small separation occurs because of side mirror structural joint. Moreover, at this location the conical vortex emerges. The probe P1008 and P2015 showed good correlation as compare to other probes reflecting that this location well predicted the wake of side mirror. However, the geometrical amendments made at side mirror surface can also be the reason for the overall variation in the results of this zone.

5.2.4.3 Reattachment Zone:

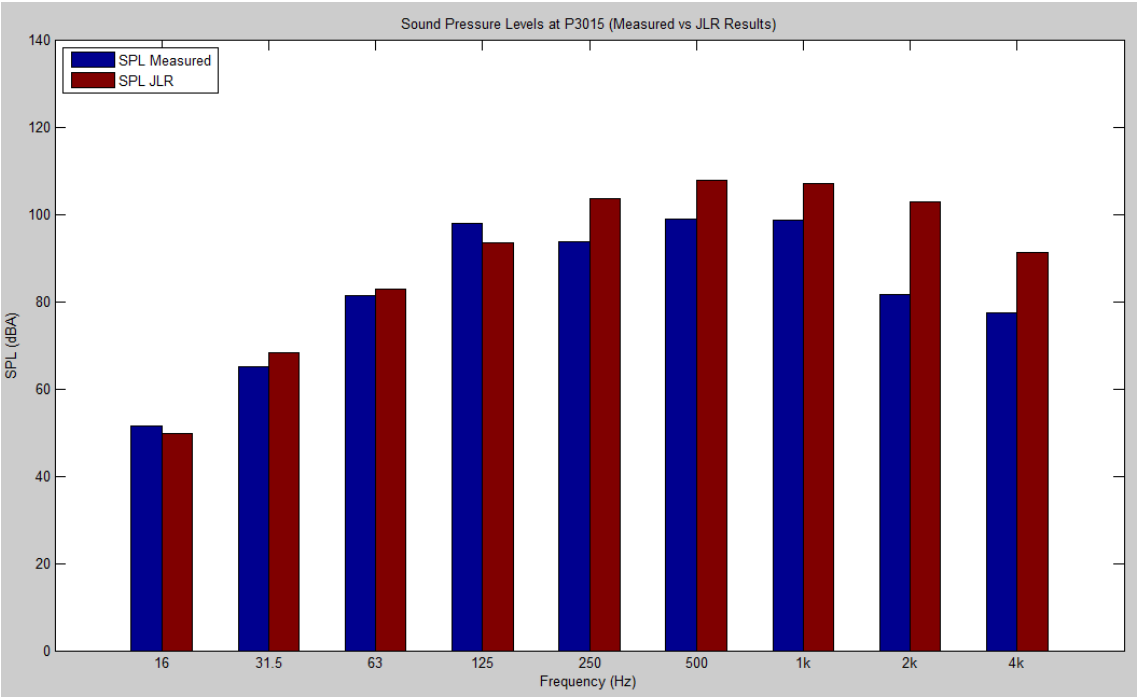

Figure 5.15 SPL comparison of CFD v/s AWT at probe location P3015

Only one probe was located in the reattachment zone. The comparison with AWT showed an average difference of 5 dBA for lower frequency range and about 25 dBA for higher frequencies.

General comments on comparison:

- The trends at higher frequencies is approximately the same except the probe locations P1001 and 2015 where the separation was experienced due to side mirror structural joint and over-predicting the size of A-Pillar vortex separation
- From the aforementioned point, it can be concluded that either the grid was too coarse to resolve the higher frequencies or due to the grid being too coarse to render the benefits of LES.

6 Conclusions and Final Remarks:

- The prime focus of this study was to analyse the vortex formation behind the A-Pillar; resulting in unsteadiness; of simplified model derived from Jaguar XF using LES.
- Three hybrid grids (unstructured with prism layers near the boundary); namely coarse, medium and fine grid were generated using Ansys ICEM CFD
- Statistical steady state was achieved; for all simulations; after 15 t_{car}. that was justified by monitoring the drag coefficient. Thereafter, the probes (flush mounted) were located at 51 locations over the front side window
- Vortex formation behind the A-Pillar was visualised using 3D & surface streamlines, slices on yz plane and iso-surface of Q visualization methods. The visualization showed bubble formation at the leading edge of hood, significance of curvature on hood, cowl vortex at hood/windshield intersection, flow-field over the angled front windshield diverting flow towards A-Pillar and unsteadiness behind the A-Pillar.
- Using the iso surface of Q, hairpin type of vortex was visualised over front windshield and the reattachment zone of front side glass window. However the coarse grid did not captured the hairpin type of vortex formation.
- A-Pillar vortex visualised by C_p contour for all grid resolutions showed that coarse mesh over-predicted the size of A-Pillar vortex whereas medium and fine grid correlated well with JLR results. Side mirror vortex was also captured and visualised with medium and fine grid

- Comparing the quantitative results of C_p; obtained by computations; with results provided by JLR showed generally a good agreement with an over-prediction of $\pm 0.1\ C_p$ except P1001 where the deviation incurred was $-0.3\ C_p$ for coarse grid and at same location medium and fine grid shows deviation of $-0.22\ C_p$ and $-0.17\ C_p$ respectively. However, error in locating probes over front side glass window was not more than ±0.01 m.
- Post-processing the Sound Pressure Levels showed variation of approximately

– 10 dBA ≤ SPL ≤ + 10 dBA at lower frequencies (≤ 250 Hz). However the difference increases at higher frequencies especially at and after 1 KHz. Reason to these discrepancies can be due to

  - The grid was not fully resolved or refined as it was only not able to resolve higher frequencies especially higher than 1 KHz. Or due to the grid being too coarse to render the benefits of LES
  - The error associated in locating probes over front side glass window
  - The results provided by JLR run for 15 sec whereas in current case only one second of t_{car} was achieved.
  - Errors involved in observing SPL are noteworthy as the scale used is logarithmic which implies an increase of 3 dB resulting in doubling of power.

For future work, using different sub grid scales of LES can be useful to look into. The LES standard model (standard Smagorinsky-Lilly model) was run upto 1 sec of flow-time with 1E-04 sec time step size due to the time constraints however this can be considered to run for enough time with lower time step size. More fine grid resolution at front side glass window, A-Pillar, side mirror and hood can be generated that can capture the small scales. Further

investigation can be done using DES or VLES turbulence models with higher order schemes.

Bibliography

[1] A. P. Gaylard (2004), "Simulation of A-Pillar/Side Glass Flows for Bluff SUV Geometries"*5th MIRA International Vehicle Aerodynamics Conference,* 13-14 October, Heritage Motor Centre, Warwick, UK.

[2] A. P. Gaylard (2006), "CFD Simulation of Side Glass Surface Noise Spectra for a Bluff SUV" *SAE Technical Paper*, DOI: 10.4271/2006-01-0137

[3] Alam, F. (2000), *The Effects of Car A-Pillar and Windshield Geometry and Yaw Angles on Local Flow and Noise* (Ph.D Thesis thesis), Department of Mechanical and Manufacturing Engineering, RMIT University, Melbourne, Australia.

[4] Alam, F., Watkins, S., Song, B., Steiner, T. and Humphris, C. (1998), "The flow charateristics around a car A-Pillar", *13th Australasian Fluid Mechanics Conference,* 13-18 December, Monash University, Melbourne, Australia

[5] Alam, F., Watkins, S. and Zimmer, G. (2003), "Mean and time-varying flow measurements on the surface of a family of idealised road vehicles", *Experimental Thermal and Fluid Science,* vol. 27, pp. 639–654.

[6] Alam, F., Watkins, S. and Zimmer, G. (2003), "A Study of the A-Pillar vortex of a passenger car", *Proceedings of the International Conference on Mechanical Engineering,* 26- 28 December 2003, Dhaka, Bangladesh

[7] *FLUENT 12.1 theory guide, (2012)* ANSYS Inc

[8] Batchelor, G. K. (1982), *The theory of homogeneous turbulence,* Cambridge University Press, UK.

[9] Bergamini, P., Casella, M., and Vitali, D. (1997), "Computational Prediction of Vehicle Aerodynamic Noise by Integration of a CFD Technique with Lighthill's Acoustic Analogy"

[10] Deardorff, J. W. (1970), "A numerical study of three-dimensional turbulent channel flow at large Reynolds numbers", *J.Fluid Mech,* vol. 41, no. 2, pp. 453-480.

[11] Freeman, C. and Gaylard, A. (2008), "Integrating CFD and Experiment: the Jaguar Land Rover Aeroacoustics Process", *7th MIRA International Conference on Vehicle Aerodynamics,* 22-23 October 2008, Ricoh Arena, Coventry, UK.

[12] Fricke, F. R. and Stevenson, D. C. (1968), "Pressure fluctuations in a separated flow region", *The Journal of the Acoustical Society of America,* vol. 44, no. 5, pp. 1189-1200.

[13] Gaylard, A. and Rover, A. P. G. J. L. (2006), "CFD simulation of side glass surface noise spectra for a bluff SUV", *SAE paper,* , pp. 01-0137.

[14] Giulia Ghezzi (2011), *RANS modelling of the A-pillar vortex structure of the Jaguar XF,* Cranfield University, UK.

[15] H K Versteeg and W Malalasekera (2007), *An introduction to Computational Fluid Dynamics: The Finite Volume Method,* 2nd ed, Pearson Education Limited.

[16] Hagemeier, T., Hartmann, M. and Thévenin, D. (2011), "Practice of vehicle soiling investigations: A review", *International Journal of Multiphase Flow,* vol. 37, no. 8, pp. 860-875.

[17] Hamel, T. A. and Ahuja, K. K. (1996), "Wind Noise Measurements on an Automobile Side Glass with A-Pillars of Different Height", *AIAA Journal*

[18] Hanaoka, Y., Zhu, M. and Miyata, H. (1993), "Numerical Prediction of Wind Noise Around the Front Pillar of a Car-Like Body", DOI: 10.4271/ *931895*

[19] Haruna, S., Kamimoto, I. and Okamoto, S. (1992), "Estimation Method for Automobile Aerodynamic Noise", *SAE Technical Paper 920205,* , DOI: 10.4271/920205.

[20] Haruna, S., Nouzawa, T., Kamimoto, I. and Sato, H. (1990), "An Experimental Analysis and Estimation of Aerodynamic Noise Using a Production Vehicle", *SAE Technical Paper 900316,* DOI: 10.4271/900316.

[21] Hinze, J. (1959), *Turbulence,* McGraw Hill Book Comp, New York.

[22] Hoarau, C., Borée, J., Laumonier, J. and Gervais, Y. (2008), "Unsteady wall pressure field of a model A-pillar conical vortex", *International Journal of Heat and Fluid Flow,* vol. 29, pp. 812–819.

[23] Jeong, J. and Hussain, F. (1995), "On the identification of a vortex", *Journal of Fluid Mechanics,* vol. 285, no. 69, pp. 69-94.

[24] Kolmogorov, A. N. (1941), "Dissipation of energy in locally isotropic turbulence", *Dokl. Akad. Nauk SSSR,* Vol. 32, pp. 15.

[25] Kolmogorov, A. N. (1941), "The local structure of turbulence in incompressible viscous fluid for very large Reynolds' numbers", *Akademiia Nauk SSSR Doklady,* Vol. 30, pp. 301.

[26] Kraichnan, R. H. (1959), "The structure of isotropic turbulence at very high Reynolds numbers", *Journal of Fluid Mechanics,* vol. 5, no. 04, pp. 497-543.

[27] Launder, B. E. and Spalding, D. B. (1972), *Mathematical models of turbulence,* Academic Press, London, UK.

[28] Leonard, B. (1991), "The ULTIMATE conservative difference scheme applied to unsteady one-dimensional advection", *Computer Methods in Applied Mechanics and Engineering,* vol. 88, no. 1, pp. 17-74.

[29] Li, Y., Kamioka, T., Nouzawa, T., Nakamura, T. et al. (2003), "Evaluation of Aerodynamic Noise Generated in Production Vehicle Using Experiment and Numerical Simulation", *2003-01-1314*

[30] Mahavir Rajesh Shah (2011), *A study of A-pillar vortices on the Jaguar XF using transition turbulence models,* Cranfield University, UK.

[31] McDonough, J. (2004), "Introductory lectures on turbulence physics, mathematics and modeling"

[32] Mohsen, A. M. (1967), *Experimental Investigation of the Wall Pressure fluctuations in subsonic, separated flows.* AD0669214, Boeing Commercial Plane Co., Washington, USA.

[33] Murad Nurul Muiz (2009), *Computational fluid dynamics (CFD) of vehicle Aerodynamics and associated acoustics* (PhD thesis), Swinburne University of Technology, Melbourne, Australia.

[34] Murad, N. M., Naser, J., Alam, F. and Watkins, S. (2004), "Simulation of Vehicle A-Pillar Aerodynamics of Various Yaw Angles", *15th Australasian Fluid Mechanics Conference,* 13-17 December, University of Sydney, Sydney, Australia

[35] Nienaltowska, E. (1993), "Separated Flow on the Car Body: Spectral and Spatial Characteristics Analysed from the Aeroacoustic Viewpoint", *International Journal of Vehicle Design,* vol. 14, no. 5/6.

[36] 'Nurul M. Murad', 'Jamal Naser' (2004), "Simulation of Vehicle A-Pillar Aerodynamics using various Turbulence Models", *SAE 2004 World Congress & Exhibition,* pp. 2004-01-0231.

[37] Orszag, S. and Patterson, G. (1972), "Numerical simulation of turbulence", *Statistical models and Turbulence,* pp. 127-147.

[38] Parliamentary Office of Science and Technology (2009), *postnote: Environmental Noise (Contains Parliamentary information licensed under the Open Parliament Licence v1.0),* 338, www.parliament.uk, London.

[39] Patankar, S. V. and Spalding, D. B. (1972), "A calculation procedure for heat, mass and momentum transfer in three-dimensional parabolic flows",

International Journal of Heat and Mass Transfer, vol. 15, no. 10, pp. 1787-1806.

[40] Popat, B. C. (1991), *Study of Flow and Noise Generation From Car A-Pillars* (Ph.D. Thesis thesis), Imperial College London, University of London, UK.

[41] Reynolds, O. (1895), "On the dynamical theory of incompressible viscous fluids and the determination of the criterion", *Philosophical Transactions of the Royal Society of London.A,* vol. 186, pp. 123-164.

[42] Sadakata, O., Kanamaru, K. and Kakamu, T. (1988), "A Consideration Of Wind Noise Reduction By Air Flow Control", *SAE Technical Paper 885115,* DOI: 10.4271/885115.

[43] Stapleford, W. R. and Carr, G. W. (1970), *Aerodynamic Noise on Road Vehicle, Part 1, The Relationship Between Aerodynamic Noise and the Nature of Airflow,* 1979/2, The Motor Industry Research Association.

[44] Taylor, G. I. (1935), "Statistical theory of turbulence", *Proceedings of the Royal Society of London.Series A, Mathematical and Physical Sciences,* vol. 151, no. 873, pp. 421-444.

[45] Townsend, A. (1980), *The structure of turbulent shear flow,* Cambridge University Press.

[46] Watanabe, M., Harita, M. and Hayashi, E. (1978), "The Effect of Body Shapes on Wind Noise", *SAE Technical Paper 780266,* DOI:10.4271/780266.

[47] Whyte, S. A. (1993), *A Flow Visualization Study of Acoustically Enhanced Hairpin Vortices* (Master's Thesis thesis), University of Washington, USA.

[48] Zhu, M., Hanaoka, Y., Aoki, K., Miyata, H. and Terada, I. (1993), "A Numerical Study of Wind Noise Around Front Pillar", *DOI: 10.4271/930296,* .

Appendix

A. Sound pressure levels at three probes located in A-Post wake region.

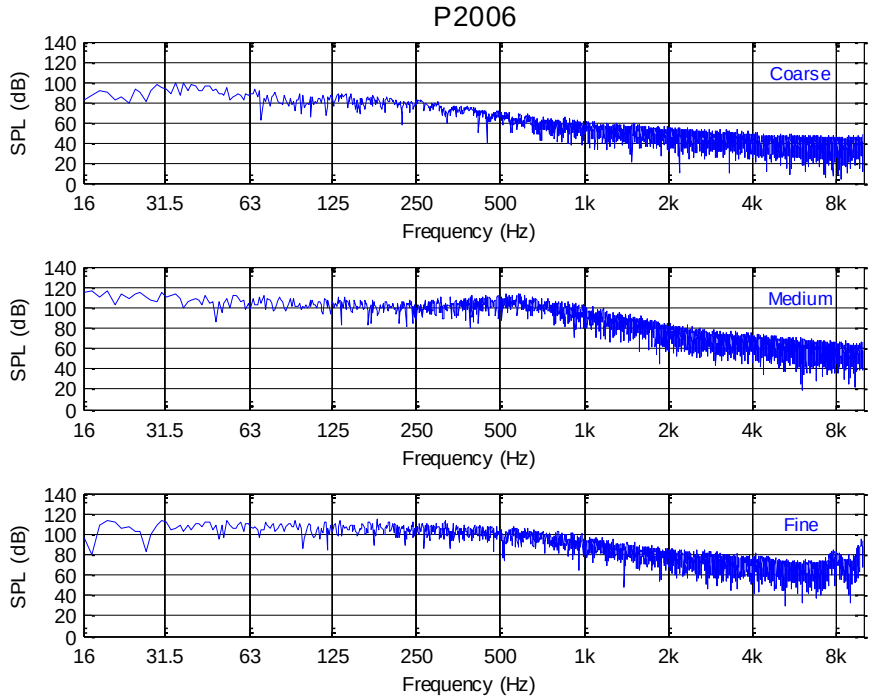

SPL (1/3rd Octave) (dB) V/s Frequency (Hz) at probe location 2006

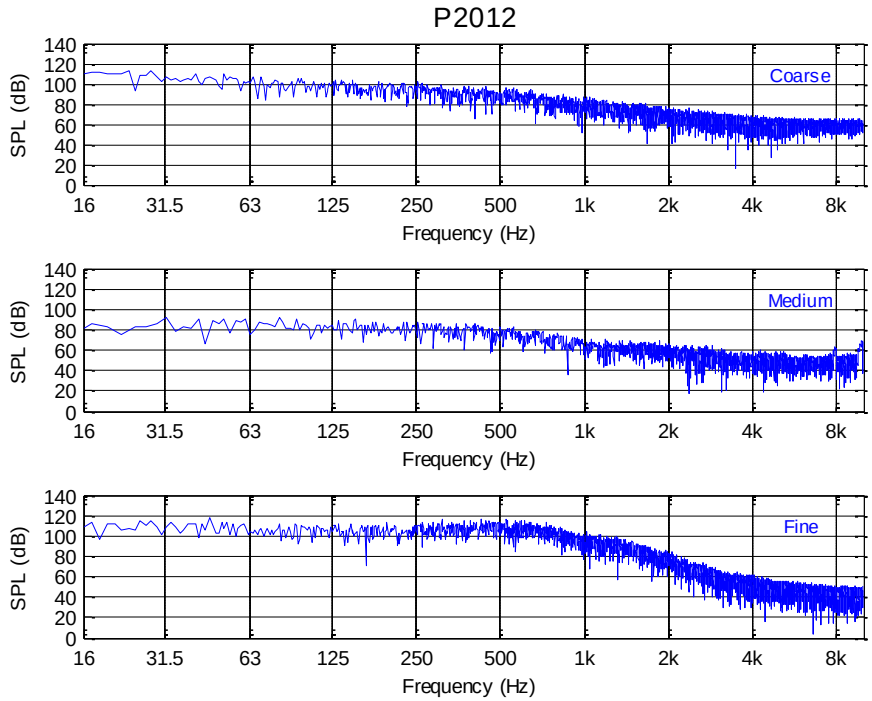

SPL (1/3rd Octave) (dB) V/s Frequency (Hz) at probe location 2012

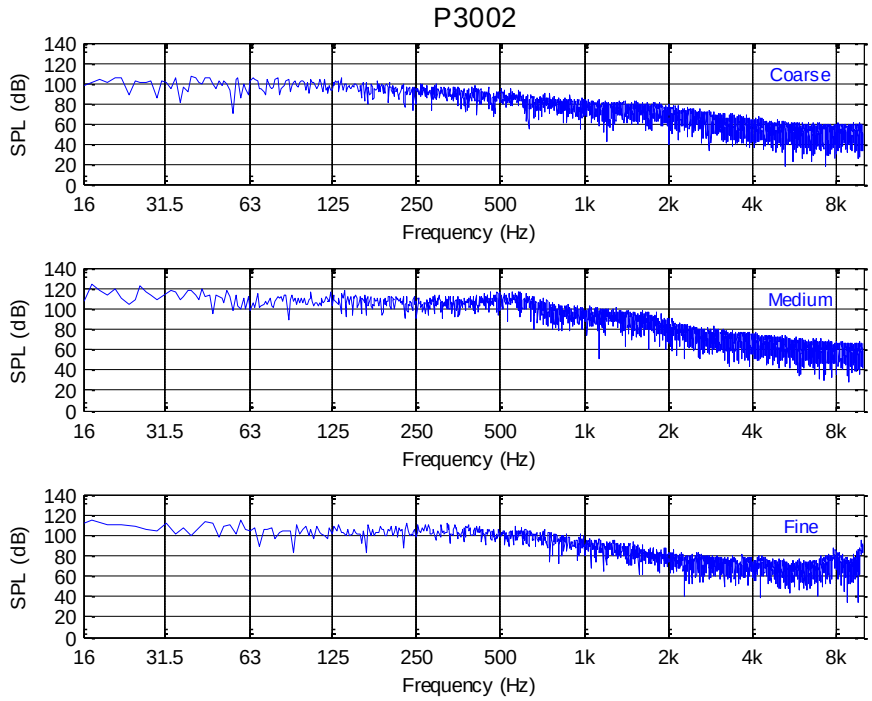

SPL (1/3rd Octave) (dB) V/s Frequency (Hz) at probe location 3002

B. Sound pressure levels at three probes located in side mirror wake region.

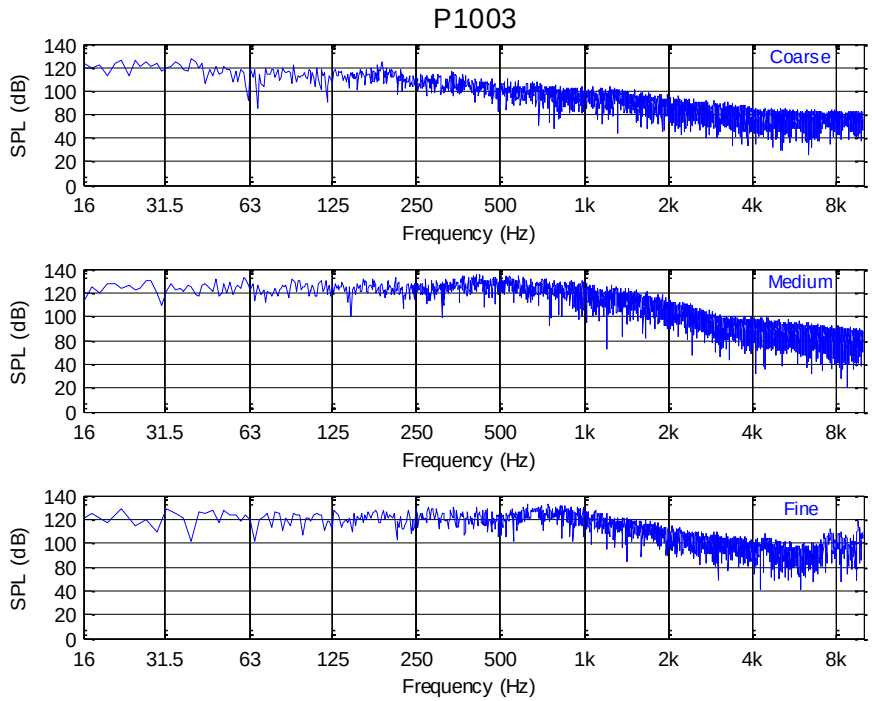

SPL (1/3rd Octave) (dB) V/s Frequency (Hz) at probe location 1003

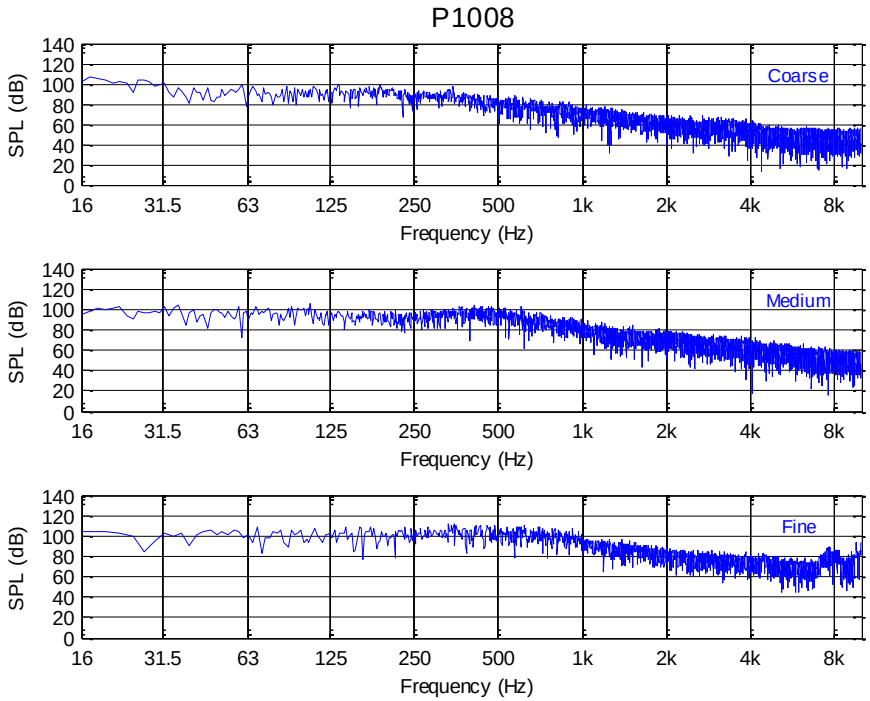

SPL (1/3rd Octave) (dB) V/s Frequency (Hz) at probe location 1008

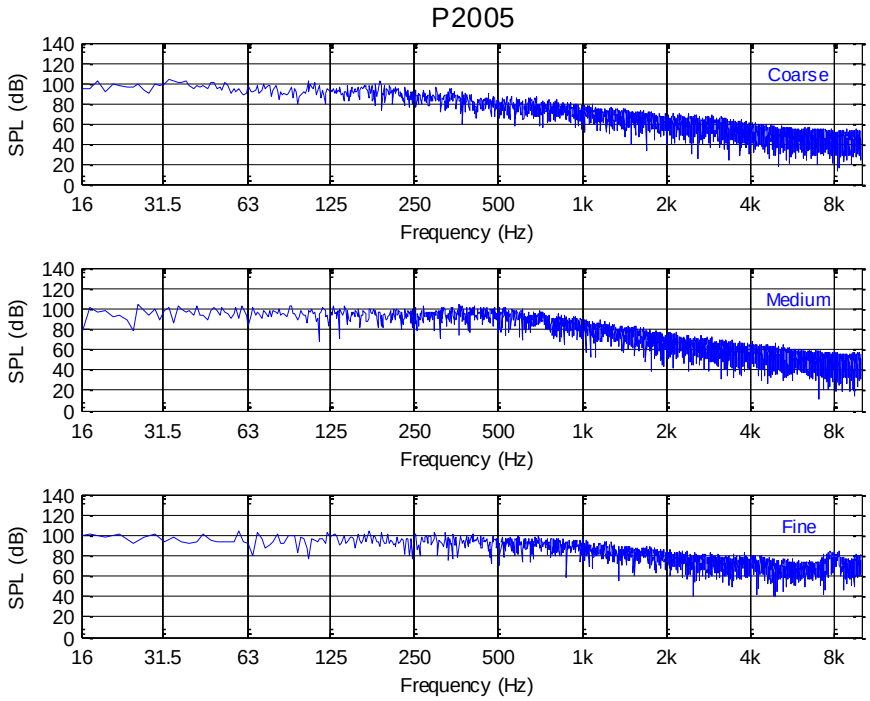

SPL (1/3rd Octave) (dB) V/s Frequency (Hz) at probe location 2005

C. Sound pressure levels at three probes located in side mirror wake region.

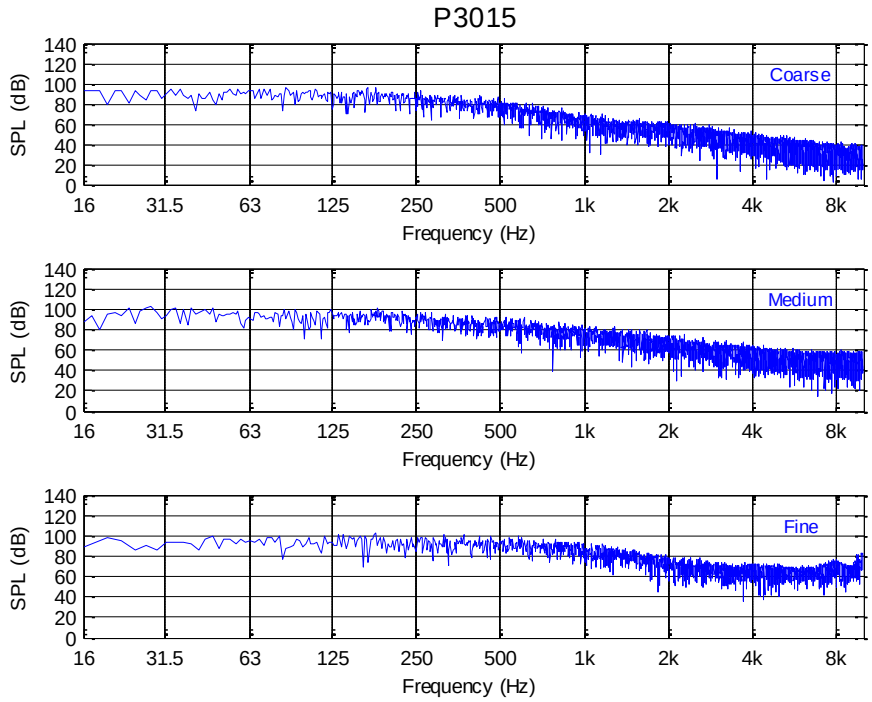

SPL (1/3rd Octave) (dB) V/s Frequency (Hz) at probe location 3015